UNIVERSIDADE FEDERAL DE SÃO CARLOS
CENTRO DE CIÊNCIAS EXATAS E DE TECNOLOGIA
DEPARTAMENTO DE QUÍMICA
PROGRAMA DE PÓS-GRADUAÇÃO EM QUÍMICA

SYNTHESIS OF g-C_3N_4/Nb_2O_5 HETEROSTRUCTURES: STUDY OF PHOTOCATALYTIC PROPERTIES

Gelson Tiago dos Santos Tavares da Silva*

Thesis presented as part of the requirements to obtain the title of DOCTOR IN SCIENCES, concentration area: PHYSICAL-CHEMISTRY.

Advisor: Caue Ribeiro de Oliveira
Co-advisor: Elaine Cristina Paris

*** bolsista CAPES/EMBRAPA**

São Carlos - SP
2019

UNIVERSIDADE FEDERAL DE SÃO CARLOS

Centro de Ciências Exatas e de Tecnologia
Programa de Pós-Graduação em Química

Folha de Aprovação

Assinaturas dos membros da comissão examinadora que avaliou e aprovou a Defesa de Tese de Doutorado do candidato Gelson Tiago dos Santos Tavares da Silva, realizada em 22/04/2019:

Profa. Dra. Elaine Cristina Paris
EMBRAPA

Prof. Dr. Jean Marcel Ribeiro Gallo
UFSCar

Prof. Dr. Jose Maria Correa Bueno
UFSCar

Profa. Dra. Elisabete Inacio Santiago
IPEN

Profa. Dra. Daniela Zanchet
UNICAMP

DEDICATÓRIA

Dedico este trabalho a toda minha família e amigos em especial a minha esposa e minha mãe, pessoas maravilhosas que não mediram esforços para tornar esse sonho possível.

AGRADECIMENTOS

A Deus por ter me ajudado a superar as dificuldades ao longo dessa caminhada.

Ao Dr. Caue Ribeiro, pela amizade, orientação e conselhos durante todo o período do doutorado.

À Dra. Elaine Paris, pela coorientação e suas contribuições no Exame de Qualificação e durante todo o período do doutorado.

Aos doutores André, Kele, Juliana, Luís, Vagner e Henrique pelo suporte sempre que necessário, parceria frutífera e acima de tudo pela amizade.

Aos doutores Elton Sitta, Guilherme Nogueira, Júlio Sczancoski, José Maria C. Bueno, Elisabete Santiago, Jean Gallo e Daniela Zanchet pelas contribuições durante as avaliações (Exame de Qualificação, Seminário e defesa) do meu doutorado.

À Embrapa Instrumentação pela excelente estrutura fornecida para realização deste trabalho. Um agradecimento especial ao pessoal de suporte à pesquisa, Viviane, Adriana, Silviane, Mattêo, Paulinho, Joana e Suzane.

Ao Programa de Pós-Graduação em Química da Universidade Federal de São Carlos (PPGQ-UFSCar), pela oportunidade que me foi dada para realizar o doutorado.

À CAPES que em parceria com a Embrapa, concedeu a bolsa de estudos, além de todo o suporte financeiro, para a realização deste trabalho.

Ao Laboratório de Caracterização Estrutural LCE/DEMa pelas análises de HRTEM. Ao Laboratório Interdisciplinar de Eletroquímica e Cerâmica LIEC/UFSCar em especial aos meus amigos Francisco, Pablo e Mitchel, pela amizade e auxílio em diversas análises. Ao Laboratório Nacional de Nanotecnologia (LNNano/LNLS) pela realização das medidas de XPS.

À CBMM (Companhia Brasileira de Metalurgia e Mineração) por disponibilizar todo o nióbio utilizado neste trabalho.

Ao Dr. Marcelo Carmo pela supervisão e cooperação durante o estágio no Forschungszentrum, em Jülich.

A todos do grupo de pesquisa do qual faço parte e companheiros de sala, em especial ao Fernando, Amanda, Jessica, Margareth, Paulo, Thiane, Eduardo e Stella por tornar o ambiente de trabalho sempre agradável e produtível, acima de tudo pelo companheirismo e amizade.

Aos meus pais, Ireni e José Carlos, os pilares da minha família, que compartilharam comigo esse sonho e não mediram esforços para que eu pudesse alcançar o final de mais essa jornada.

À minha esposa, Tamires, por sua paciência e amor incondicional durante todos esses anos, sempre me incentivando e tornado essa caminhada mais amena.

Ao Osmando e Marcela, pela amizade, companheirismo e conselhos que me fizeram crescer no âmbito pessoal e profissional.

Aos meus amigos Carlos, Tiago, Edilson, Igor e todos do Laboratório LERCI, em especial ao Gabriel, pessoas fantásticas que o doutorado me proporcionou, tornando através de confraternizações e rodas de tereré, momentos de completa descontração.

A todos os meus familiares e amigos que contribuíram direta e indiretamente para a conclusão de mais essa etapa da minha vida, meu muito obrigado.

TABLE LIST

FIGURE LIST

SCHEME LIST

RESUMO

SÍNTESE DE HETEROESTRUTURAS g-C_3N_4/Nb_2O_5: ESTUDO DAS PROPRIEDADES FOTOCATALÍTICAS. Semicondutores são catalisadores promissores para processos de fotossíntese artificial, porém até o momento não há um material de consenso como fotocatalisador ideal para a redução de CO_2. Entre os utilizados com essa finalidade, o Nb_2O_5 é uma alternativa promissora, uma vez que possui características promissoras à catálise, como grupos de superfície capazes de auxiliar em processos catalíticos e alta estabilidade química. No entanto, sua capacidade de absorver somente radiação UV torna seu uso em larga escala, utilizando a radiação solar, um processo pouco eficiente. Portanto nesta tese foi investigada uma alternativa para melhorar as características do Nb_2O_5 como fotocatalisador, através da formação de heterojunções com o C_3N_4, um semicondutor que absorve abaixo de 460 nm do espectro visível. Inicialmente, observou-se a capacidade do Nb_2O_5 em fotocatalisar a reação de conversão de CO_2 em produtos C1 e C2, dado que óxidos de nióbio de um modo geral possuem elevada acidez superficial, fator que poderia diminuir a interação entre o CO_2 e a superfície do catalisador. No entanto observou-se que a acidez superficial do Nb_2O_5 o tornou em catalisador preferencial para formação de CO, devido à baixa interação dessa molécula com a superfície do catalisador. Com isso, observou-se que o Nb_2O_5 é um possível agente catalisador de reações de fotoredução de CO_2. Após verificar as principais características do Nb_2O_5, buscou-se alternativas para formar heterojunções entre o Nb_2O_5 e o g-C_3N_4, tanto para aumentar sua absorção do espectro eletromagnético, quanto para aumentar sua performance fotocatalítica. Para tal optou-se pela heteroagregação sonoquímica induzida pela diferença de carga superficial. Esse método se mostrou eficiente e capaz de formar heteroestruturas g-C_3N_4/Nb_2O_5, onde as partículas de Nb_2O_5 foram homogeneamente dispersas sob a superfície do g-C_3N_4, conferindo assim um intimo contato entre as partículas, elevado compartilhamento das cargas fotogeradas e consequentemente uma alta atividade fotocatalítica tanto para degradação de poluentes orgânicos, quanto para conversão de CO_2 em CH_4.

ABSTRACT

SYNTHESIS OF g-C_3N_4/Nb_2O_5 HETEROSTRUCTURES: STUDY OF PHOTOCATALYTIC PROPERTIES. Semiconductors are promising catalysts for artificial photosynthesis, but to date, there is no consensus on the ideal photocatalyst for CO_2 reduction. Among semiconductors used for CO_2 reduction, Nb_2O_5 is a promising alternative, since it has characteristics useful for catalysis, such as surface groups capable of assisting catalytic processes and high chemical stability. However, Nb_2O_5 absorbs only UV radiation, thus large scale application of the same under solar radiation is inefficient. Given this problem, the formation of heterojunctions between Nb_2O_5 and C_3N_4, a semiconductor that absorbs below 460 nm of the visible spectrum, was investigated in this thesis as an alternative method to improve the photocatalytic properties of Nb_2O_5. Initially, the ability of Nb_2O_5 to convert CO_2 in C1 and C2 products under irradiation was studied since Nb_2O_5 is known for its high surface acidity, a factor that could decrease the interaction of CO_2 with the surface of the catalyst. However, it was observed that the surface acidity of Nb_2O_5 favored the formation of CO due to the low interaction of this molecule with the surface of the catalyst. This finding showed that Nb_2O_5 is a possible catalyst for CO_2 photoreduction reactions. Accordingly, the main characteristics of Nb_2O_5 was verified and alternative synthesis methods for the formation of heterojunctions between Nb_2O_5 and g-C_3N_4 were investigated in order to shift the absorption of Nb_2O_5 into the visible region and increase its photocatalytic performance. To that end, heteroaggregation induced by difference in superficial charge was chosen. The method proved efficient for the formation of g-C_3N_4/Nb_2O_5 heterostructures, where the Nb_2O_5 particles were homogeneously dispersed on the surface of g-C_3N_4, thus conferring an intimate contact between the particles, high sharing of photogenerated charges, and consequently high photocatalytic activity for the degradation of organic pollutants and conversion of CO_2 into CH_4.

SUMMARY

1 INTRODUCTION

1.1 Background

In the mid-18th century, the industrial revolution boosted the economy and consequently improved the quality of human life beings in an unprecedented way. However, this rapid development brought with it factors such as disordered population growth, as well as high human dependence on fossil fuels, both domestic and industrial. Thus, there is also an intensification of the water pollutant resources around the world, due to the inadequate disposal of organic and inorganic compounds from industrial and agro-industrial waste.[1–3]

The irrational use of fossil fuels has brought an irreparable price to the environment, through increasingly severe climate changes, since the burning of these fossil fuels generate toxic gases, such as carbon dioxide (CO_2), that intensify the so-called greenhouse effect.[4–6] In this scenario, the development of technologies able to mitigate these anthropic effects has been gaining increasingly notoriety.

Currently, the ways to promote the suppression of these effects are processes that demand high investments and in some cases are not very efficient, thus making them infeasible. An alternative to overcome these barriers is the use of low-cost catalysts capable of accelerating the redox processes of converting these compounds into products with less environmental damage.[7–9]

Promising candidates are semiconductors, which when excited under visible or ultraviolet electromagnetic radiation produce carriers of reducing and oxidizing charges capable of promoting directly or indirectly the processes of degradation of organic compounds as well as the conversion of CO_2 into products such as methane, ethanol among other organic compounds of industrial interest, efficiently.[10,11]

Among the photocatalysts currently used, niobium pentoxide (Nb_2O_5) has been drawing attention because it is directly associated with strategic factors for the Brazilian economy, since the country has the largest niobium

reserves in the world. Its electronic structure is similar to of TiO_2, the semiconductor most used in photocatalytic processes having interesting fundamental characteristics in catalytic processes, such as high surface acidity as well as high chemical and physical stability.[12,13]

However, like TiO_2, Nb_2O_5 has limitations for large-scale use, since its activation is only by ultraviolet radiation, which corresponds to approximately 3% of the solar spectrum [14] (Among the different ways to surpass this barrier, the formation of a semiconductor junction that absorbs larger parts of solar spectrum has been proved to be an interesting alternative .[15–17]

A promising candidate is graphitic carbon nitride (g-C_3N_4), a semiconductor that can be activated with energy of 2.7 eV, absorbing approximately 44% of the solar spectrum, Therefore its use in favored for large scale catalytic processes, associated to the low cost of its typical precursors (urea, melamine, and cyanamid) and simple synthesis.[18–20] Therefore, the formation of heterostructures between Nb_2O_5 and g-C_3N_4 proves to be an interesting alternative both to increase the absorption spectrum of the formed material and to improve its catalytic activity. The charge migration in heterostructure reduces electron-hole recombination, one of the main factors associated with the increase of the photocatalytic activity.[21]

Although there are some studies that report the use of g-C_3N_4/Nb_2O_5 heterostructures in photocatalytic processes, there are still several knowledge gaps to be filled with respect to the efficient formation of heterojunctions, in order to improve the particle distribution, thus reducing the agglomeration and increasing the contact surface between the semiconductors, favoring the migration of photogenerated charges.

1.2 Semiconductors in photocatalytic process

The pioneers in the development of catalytic processes using semiconductors were Fujishima and Honda, when in 1972, they reported the water

oxidation and the evolution of H_2 and O_2 gases when a TiO_2 suspension was irradiated in an electrochemical cell.[11,22] The relevance of the Fujishima and Honda work is evident because it reached more than 21,000 citations just over 45 years, which corresponds to an average of approximately 470 citations per year (more than one per day). This research was the main responsible for what can be called “modern heterogeneous photocatalysis”. Moreover, among several possibilities, the anatase TiO_2 polymorph has become the “battle horse” of this research field.[23]

The same scientific principle applied in electrochemical cell presented by Fujishima and Honda can be idealized for process in solution, as organic contaminant oxidation in aqueous medium. Thenceforth, several semiconductors have been tested as photocatalysts.[24–26] To the best of our knowledge, the oldest research on photocatalytic properties of semiconductors, namely ZnO, Sb_2O_3 and TiO_2, carried out by Markham, dates back to 1955.[27] In this work, various types of chemical reactions that these oxides could promote were described, among them the oxidation of organic compounds under UV radiation. Some years later, ZnO application to carbon monoxide oxidation was described in two articles of Hauffe and Doerfler published in *The Journal of Catalysis*.[28,29] Subsequently and especially after the aforementioned work performed by Fujishima and Honda, several researches were devoted to understanding photocatalytic processes involving oxidation and reduction process, such as degradation of organic compounds, water splitting and CO_2 conversion, promoted by an ample variety of semiconductors.

This broad interest in semiconductors for energy generation or environmental remediation is mainly due to its electronic structure, composed of two energy bands, called valence (VB) and conduction band (CB). In addition, it has a region that does not have electronic levels, which is between the valence bands and the conduction band, this region is called band gap (bg) (as can be seen in FIGURE 1.1). When the semiconductor absorbs energy equal to or greater than

its bandgap, it promotes electrons from VB to CB, thus creating the aforementioned positive and negative charges in bands VB and CB, respectively (1). After photogenerated, the electron/hole pair can catalyze chemical reactions, promoting the heterogeneous photocatalysis (3-5). On other hand, the electron can simply return to VB by photons or phonons (2). In this case, the material is considered non-reactive in photochemical processes.[30]

The semiconductor can act as a catalyst in different ways, directly or indirectly. The direct way is when the electron/hole pairs oxidize or reduce the molecules of interest, for example, the CO_2 reduction, where there is transference of the electrons from the CB to the CO_2, forming $^{\bullet-}CO_2$, making it a molecule reactive and capable of after multiple steps form C1 or C2 molecules (4).[31] An example of organic molecules degradation via direct oxidation occurs after the molecule adsorbs under the catalyst surface has a lower oxidation potential than the VB band of the semiconductor, which makes the process thermodynamically favorable (5).[32]

The indirect degradation process occurs in cases where the photogenerated electron/hole loads interact with molecules capable of mediating the degradation process of more stable molecules, such as the formation of hydroxyl radicals, through the water oxidation process, or the formation of superoxide radicals by reducing the oxygen dispersed in the medium (3). These species have high oxidizing and reducing potentials, becoming the main mechanism of degradation of organic molecules.[32]

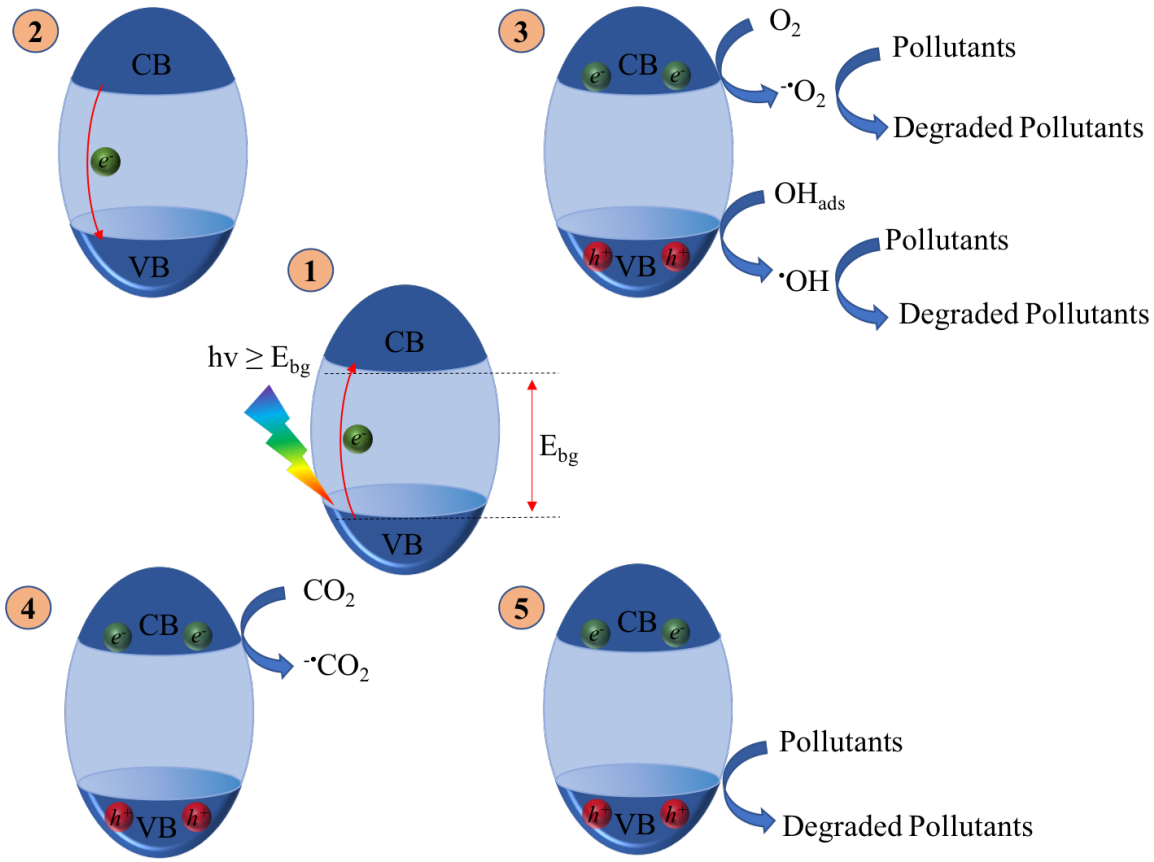

FIGURE 1.1 – Simplified mechanisms of photocatalysis on a semiconductor surface: (1) charge photogeneration by absorption of photons with energy higher than semiconductor band gap (E_{bg}), electrons (negative charge – e^-) and holes (positive charges – h^+); (2) recombination of photogenerated charges with release of absorbed energy as photons or phonons; (3) formation of hydroxyl radical (•OH) by electrons transfer from groups adsorbed on the solid surface, such as H_2O or OH^-, to pervade positive holes in valence band; (4) reduction process by transfer of electron of conduction band to electron acceptors adsorbed on the solid surface; (5) direct oxidation and posterior degradation of contaminants by potential generated in the valence band.

Valence band holes are powerful oxidants with a potential reduction between +1.0 and +3.5V *vs* NHE (Normal Hydrogen Electrode), while conduction band electrons are excellent reducing agents (+ 0.5 to -2.0 V *vs* NHE). These values are dependent on the semiconductor and certain medium conditions, such as pH.[33] Both hydroxyl groups and water adsorbed on semiconductor surface

can be oxidized to $^{\bullet}OH$ radicals, which contain sufficient potential to oxidize various organic compounds, however, they may have different potential (surface bonded $OH/^{\bullet}OH \geq 1.6$ V *vs* NHE and $H_2O/^{\bullet}OH = +2.72$ V *vs* NHE).[34] On the other hand, the oxygen molecules dissolved in the reaction or on the surface of the catalyst usually act as oxidants, capturing the formed electron, producing the superoxide radical anion. Although this radical contributes little to the photocatalytic process, since these species are less reactive than the other species generally formed in higher quantity in a photocatalytic reaction ($E^{\circ}(O_2/^{-\bullet}O_2) = -0.33$ V *vs* NHE), their role should not be disregarded in the photocatalytic process oxidative as a whole.[35]

However, although the oxidation concept of organic pollutants is well known by the scientific community, several other factors must be taken into account for direct conversion of CO_2 through photocatalytic reduction. This is because CO_2 is a chemically inert molecule and has high chemical and physical stability due to its linear geometry and stable covalent bonds. So, any attempt to reduce it to form any C1 or C2 products requires a substantial amount of energy to promote the formation of the first intermediate of the CO_2 reduction reaction, CO_2 radical, from which it is possible to form such pure or oxygenated hydrocarbons. The addition of an electron to CO_2 to form $^{-\bullet}CO_2$ has a very negative reduction potential ($E^{\circ} = -1.9$ V *vs* NHE), which is the limiting step of the reaction rate.[10,36]

To illustrate the different products that can be formed by the CO_2 reduction reaction, the reduction potentials for the CO_2 reduction half-reactions in different products are shown in TABLE 1.1, noting that these data are thermodynamic, not giving any indication to reaction kinetics, i.e. the reaction speed and its reaction mechanism.[37]

TABLE 1.1 - CO_2 reduction potential in water for different products (E^o, V *vs* NHE at pH 7)[37]

$CO_2 + 2e^-$	→	$CO_2^{\bullet -}$	E^o = - 1.90 V
$CO_2 + 2e^- + 2H^+$	→	$CO + H_2O$	E^o = - 0.53 V
$CO_2 + 2e^- + 2H^+$	→	$HCOOH$	E^o = - 0.61 V
$CO_2 + 4e^- + 4H^+$	→	$HCOH + H_2O$	E^o = - 0.48 V
$CO_2 + 6e^- + 6H^+$	→	$CH_3OH + H_2O$	E^o = - 0.38 V
$CO_2 + 8e^- + 8H^+$	→	$CH_4 + 2H_2O$	E^o = - 0.24 V
$2H_2O + 4h^+$	→	$O_2 + 4H^+$	E^o = + 0.81 V
$2H^+ + 2e^-$	→	H_2	E^o = - 0.42 V

Based on these data FIGURE 1.2 shows possible photocatalyst candidates in processes conducted in aqueous medium, for CO_2 reduction, water splitting or pollutant degradation.

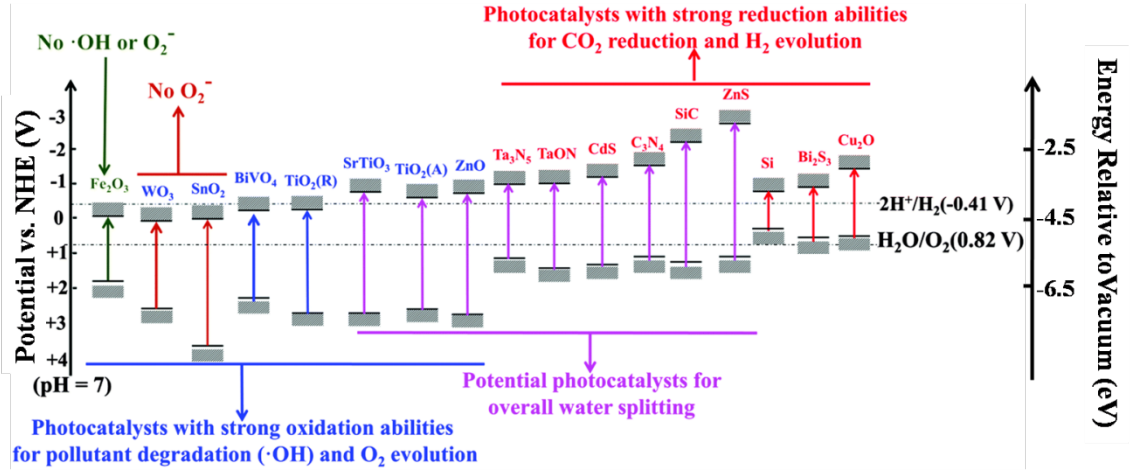

FIGURE 1.2 – Calculated energy positions of conduction band edges and the valence band of selected semiconductors. (Adapted from Li et al. 2016)[38]

As can be seen in FIGURE 1.2, the anatase phase of TiO_2 can be used for water splitting as well as for pollutant degradation due to commercial availability, stability, low cost, non-toxicity, adequate values of electron reduction potential and photogenerated holes in the conduction and valence bands.[39,40] Nb_2O_5 has similar band structures, as shown in FIGURE 1.3, and due this has

been attracting attention also due to its high chemical and physical stability.[41,42]

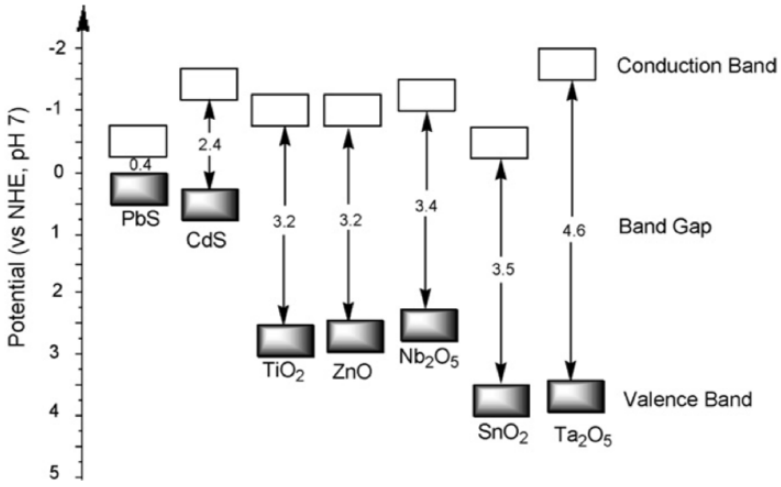

FIGURE 1.3 – Electronic structure of different semiconductors and their energy potential values at pH 7.[43]

Nb_2O_5 has been shown to have a good catalytic performance both for chemical reactions as pyruvaldehyde degradation to form lactic acid, as well as alkylation of benzyl alcohol.[44,45] Both reactions catalyzed by their high surface acidity (equivalent to> 70% concentrated H_2SO_4).[46] Already in the process of photocatalytic their abilities in decreasing the recombination time of the electron pairs/hole, associated to the position of their valence and conduction bands (E_{bg} ~ 3.4 eV) that favor mainly the degradation of dyes by the formation of radicals hydroxyl and superoxide.[13,47] In addition, some of the reactions photocatalyzed by Nb_2O_5 have also been associated with its high surface acidity, both by the interaction between the pollutant and the catalyst surface, as well as by the alteration of the pH of the medium, favoring the working range in the which Nb_2O_5 is most efficient.[43,48]

The high acidity of niobium pentoxide is one of the main attractions of this oxide in catalytic processes in general, being its properties dependent on its crystalline structure and surface groups. Niobium oxide with low crystallinity

or phase mixture that induces distortions in its crystal lattice is often obtained, causing defects such as vacancy or excess of atoms, thus conferring surface groupings or electron density capable of influencing catalytic processes. Hydrated amorphous niobium pentoxide (Nb_2O_5•nH_2O, niobic acid) contains the Brønsted and Lewis acid sites and is capable of promoting a large number of chemical reactions, even in the presence of water molecules.[49]

However, this semiconductor, as well as the main photocatalysts, i.e., TiO_2 and ZnO, has an energy limitation being activated only under UV radiation, making it poorly efficient to apply it on a large scale using solar radiation .[50,51] Solar energy is composed of 44% visible radiation and 53% infrared, with only 3% of UV radiation.[14]

In this scenario, processes such as the sensitization with organic molecules, doping with elements such as carbon, sulfur, and nitrogen, or decorating with metallic nanoparticles, or even the use of semiconductors that absorb a larger fraction of the solar spectrum, appear as an option to circumvent this energy barrier.[52] The formation of heterojunctions between two or more semiconductors or crystalline phases is a procedure that has been gaining prominence in recent years. This alternative has shown to be able not only to improve the absorption of the energy spectrum of the materials but also a way to improve its photocatalytic activity by charge transfer between the semiconductors.[53,54]

1.2.1 Heterostructures in photocatalytic processes

The formation of heterojunctions between different semiconductors or crystalline phases as a way to increase the properties of the formed materials, dates from the 70s, but also using TiO_2, the use of this methodology was intensified with the discovery of the so-called P25, a composite heterostructure of the anatase and rutile phases of TiO_2, in the following ratios 80 and 20%, respectively. Commercial TiO_2 (Degussa P25) is widely accepted as a

“benchmark” for its excellent photocatalytic activity. However, its practical application is limited due to its non-porous nature, low surface area, complicated preparation, and low visible light activity.[55,56]

Therefore, in 1984, Serpone et. al. have demonstrated that the coupling between TiO_2 and CdS, with respectively 3.2 and 2.4 eV bandgaps, leads to an increase in the spectral absorption range of the formed composite, making the active material under visible radiation, besides being the noticeable separation of charges, which prevents recombination. In this case, electrons photogenerated in CB of CdS after absorption of visible energy ($\lambda > 400$ nm) were transferred to the CB of TiO_2, while the positive holes remained in the electronic structure of CdS. [57]

Therefore, it is understood that this architecture composed by different compositions sharing the same interface promotes significant improvements in the fundamental properties of the semiconductors, such as bandgap, refractive index, thermal stability, charge carriers mobility among others. This charge carriers mobility may increase photocatalytic efficiency compared to isolated semiconductors, a band-structure scheme was designed demonstrating the difference between an isolated semiconductor in a heterostructure (FIGURE 1.4). The isolated semiconductors have characteristic band structures (a), as previously mentioned, but after coupling, there is the pairing of their Fermi levels and the sharing of their interfaces (b). Thus, after being activated, the photogenerated electrons/holes are shared among the semiconductors, increasing the useful lifetime of charge carriers (c), which consequently increases the time that the current semiconductor as catalyst role in the reaction.[58,59]

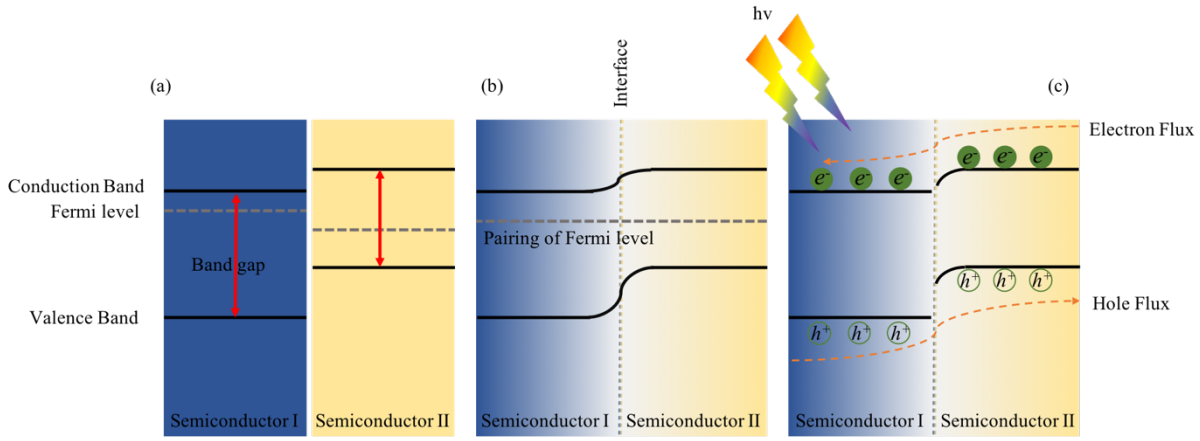

FIGURE 1.4 – Schematic illustration of the electronic structure of isolated semiconductors and their heterostructures.

Thereafter, during the last decades, the researchers tried to obtain, through various combinations of semiconductors, highly efficient and selective photocatalysts, besides explaining the high activity of these heterostructures in relation to the isolated materials. Among these combinations the formation of heterostructures between Nb_2O_5/CdS, Nb_2O_5/Bi_2WO_6, Nb_2O_5/CuO, and Nb_2O_5/g-C_3N_4 have shown to be interesting both for the increase in the energy absorption spectrum needed to start the photocatalytic processes from 365 nm to 775 nm, as well as improving its adsorption and photocatalytic capacity for both oxidative processes and the degradation of emerging organic pollutants, as well as reducing processes such as the conversion of chromium IV to chromium III, or for water splitting producing hydrogen.[60–63]

Among these main heterostructures composed of Nb_2O_5, a promising alternative for photocatalytic applications is involving g-C_3N_4 in its composition. This material, besides having a band gap of ~ 2.7 eV, is a material with lamellar structure, favorable for formation of heterostructures and with high stability, and of low cost. The synthesis of this material is relatively simple and consists in the polymerization ends of compounds rich in carbon and nitrogen, such as melamine and urea, among others.[64,65]

These precursors, when subjected to high temperatures often under an oxidizing atmosphere start the polymerization process, where the smaller molecules release NH_3 and in some cases CO_2, when subjected to a temperature of approximately 240 °C for the formation of melamine. Soon after multiple steps of temperature rise and loss of NH_3 occurs at approximately 500 and 600 °C, depending on the precursor, the formation of the two-dimensional tri-s-triazine connects via tertiary amines, g-C_3N_4.[66] It is to be noted that the chosen precursors directly interfere in the yield of the final product, since the formation synthesis of C_3N_4 via melamine polymerization, compared to urea, goes through fewer steps. However, the synthesis of g-C_3N_4 starting from smaller precursors, tend to a larger surface area, an important factor for catalytic processes in general.[15]

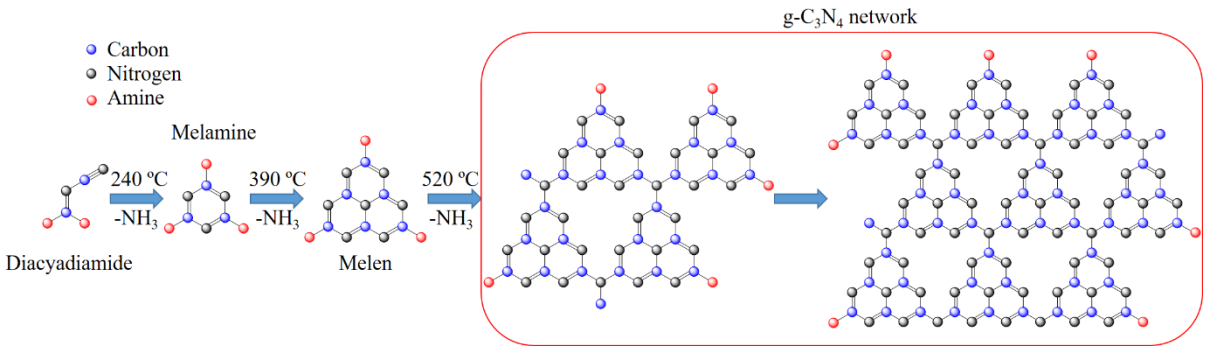

SCHEME 1.1 – Schematic illustration of the thermal polymerization process of g-C_3N_4. (Adapted from Zhang et al., 2012)[66]

Although these differences exist, with respect to their textural and crystalline structure of the materials and the precursor, the electronic structure, except in some cases, remains practically the same, attributing to this material good photocatalytic characteristics, basing itself on its band gap and potentials values of the valence and conduction bands, 1.4 and -1.23 eV, respectively.[67]

The process of complex architectures construction, such as the heterostructures, involving carbon nitride are the most varied, since ordered growth of particles under its surface, with also thermal aggregation at high

temperatures, however, several of these techniques aggregated the decrease of the activity linked to the material, such as reduction of the surface area through the pore sintering process. With this, new methodologies to obtain more efficient materials are still being investigated. [15]

1.2.2 Synthesis and Processing of Heterostructures

The foremost challenge in developing efficient heterostructures for distinct applications is the definition of which semiconductors can be combined in order to exhibit a maximized electron/hole pair lifespan and simultaneously present appropriate positions of valence and conduction bands to conduct photo-oxidative reactions. Nonetheless, the need to create interfaces/junctions between two semiconductors that often present none crystallographic similarities (i.e. comparable values of interplanar distances) generates an additional challenge, which is the synthesis and/or processing to obtain the final heterostructure.[38]

Numerous synthesis methods have been applied to obtain heterostructures from different semiconductors, such as sol-gel, polymer precursors and hydrothermal method. However, the major variations in obtaining heterostructures lie in the utilized strategy rather than in the method itself, i.e. simultaneous growth of two phases in equal reaction medium, phase growth over a preformed second phase, or heterostructures formation applying preformed particles as building blocks.[68]

For the formation of heterostructures involving g-C_3N_4, there must necessarily be a calcination process, because up to the present moment, there is little evidence of another alternative route to obtain it. Therefore, the simultaneous synthesis process, in many cases, uses as precursor melamine, which mixed with Cu, Zn, and Ti precursors under high temperatures and oxidizing atmosphere, form the respective oxides and g-C_3N_4.[69–71] However, the coalescence process between the metal particles, leads to form oxides with low porosity and surface area, in addition, the presence of metals in the reaction medium, facilitates the

thermal degradation of melamine, acting as a catalyst, in this way occurs in some cases the loss of the final yield of the synthesis.

The process of growth of one of the phases on the g-C_3N_4 formed, has proved to be an interesting alternative, since it is possible by methods such as crystallization by hydrothermal method, materials with high surface area, or even functionalized surfaces capable to increase the activity of the formed heterostructures, as it is the case of the heterostructures g-C_3N_4/Nb_2O_5, C_3N_4/$BiOIO_3$, C_3N_4/$BiVO_4$, among the others.[72–74] In both cases, there is a significant improvement in materials activities, both in oxidative and reductive processes. However, some important synthesis parameters are not yet taken into account, such as pH, a variable that considerably alters the properties of the final product.

Within this scenario, the synthesis of heterostructures using preformed materials appears as an interesting alternative. They demonstrate, through heterostructures such as SnO_2/TiO_2, g-C_3N_4/Pt, g-C_3N_4/Zn_2GeO_4, that the junctions are effective and with considerable catalytic efficiency, probably due to the good dispersion between the particles to be agglomerated and the maintenance of the surface and morphological characteristics of each catalyst. Important catalytic factors that are maintained due to the control of temperature, pressure, pH among other synthesis parameters that can be controlled through this methodology.[75,76]

In this thesis, the main photocatalytic influences of Nb_2O_5 and g-C_3N_4, as well as different synthesis strategies to obtain g-C_3N_4/Nb_2O_5 heterostructures were investigated, aiming at the best way to induce the intimate contact between the preformed particles, thus promoting an increase in its photocatalytic activities, for environmental remediation in oxidative processes, such as the degradation of organic pollutants, as well as reductive, such as the conversion of CO_2 into CH_4.

2 GOALS AND OVERVIEW

The main goal of this thesis was to study the effect of type-II heterostructure formation between g-C_3N_4 and Nb_2O_5 on their photocatalytic reduction and oxidation properties.

Specific goals:

- To understand the influence of Niobium acid surface on the photocatalytic process;
- To study the effects provided by the formation of heterojunctions between g-C_3N_4 and Nb_2O_5 in photocatalytic systems.
- To investigate the efficiency of the g-C_3N_4/Nb_2O_5 heterostructures in the CO_2 conversion into CH_4.

2.1 Summary of each chapter

This thesis goals to understand the dynamics of the physicochemical properties of Nb_2O_5 and g-C_3N_4 catalysts, as well as their heterostructures (Nb_2O_5/g-C_3N_4) during oxidizing and reducing catalytic processes, both for the generation of products with high added-value carbon and degradation of organic compounds.

For this proposal, initially as-synthesized Nb_2O_5 hydrated by a sol-gel method adapted to crystallization/dehydration by calcination. From this method, it was possible to evaluate the influence of acidic surfaces in the process of CO_2 photoreduction under UV radiation. The main results of this part are shown in Chapter I.

After understanding the role of the Nb_2O_5 acidity surface for the photocatalytic process it was proposed to increase its absorption spectrum and catalytic efficiency. For this, it was promoted the formation of heterojunction between Nb_2O_5 and C_3N_4 by a sonochemical method based on surface charge-induced heteroaggregation. This method produces a homogeneous distribution of the nanoparticles of Nb_2O_5 under the g-C_3N_4 surface and materials with good

catalytic performance under visible radiation for the degradation of organic compounds. The main results of this part are shown in Chapter II.

In order to improve the coupling between g-C_3N_4 and Nb_2O_5 by the sonochemical method, it was proposed in the last chapter (Chapter III), the alteration of the surface charge of g-C_3N_4 and the verification of this influence in the formation of g-C_3N_4/Nb_2O_5 heterostructures and in the photocatalytic properties for CO_2 reduction of the prepared materials.

3 CHAPTER I: Niobium pentoxide activity for CO_2 photoreduction

The content of this chapter is an adaptation of the article entitled "**Acidic surface niobium pentoxide is catalytic active for CO_2 photoreduction**" by Gelson T.S.T. da Silva, André E. Nogueira, Jéssica A. Oliveira, Juliana A. Torres, Osmando F. Lopes, and Caue Ribeiro, published for Applied Catalysis B: Environmental.

Reference: Applied Catalysis B: Environmental 242 (2019) 349–357.

Applied Catalysis B: Environmental 242 (2019) 349–357

Contents lists available at ScienceDirect

Applied Catalysis B: Environmental

journal homepage: www.elsevier.com/locate/apcatb

Acidic surface niobium pentoxide is catalytic active for CO_2 photoreduction

Gelson T.S.T. da Silva[a,b], André E. Nogueira[c], Jéssica A. Oliveira[b,d], Juliana A. Torres[b], Osmando F. Lopes[e], Caue Ribeiro[b,*]

[a] Department of Chemistry, Federal University of São Carlos (UFSCar), 13565-905, São Carlos, SP, Brazil
[b] National Nanotechnology Laboratory for Agribusiness (LNNA), Embrapa instrumentation, 13561-206, São Carlos, SP, Brazil
[c] Brazillian Nanotechnology National Laboratory (LNNano), CNPEM, 13083-970, Campinas, SP, Brazil
[d] Department of Chemical Engineering, Federal University of São Carlos (UFSCar), 13565-905, São Carlos, SP, Brazil
[e] Federal University of Uberlândia, Institute of Chemistry, Santa Mônica, 38400-902, Uberlândia, MG, Brazil

3.1 Abstract

In this paper, we report for the first time the significant photocatalytic activity of Nb-based materials for CO_2 reduction. Nb_2O_5 catalysts were prepared through a modified peroxide sol−gel method using different annealing temperatures, showing activity for CO_2 photoreduction in all conditions. The activity and selectivity of the Nb_2O_5 samples were directly related to their surface acidity: high surface acidity prompted conversion of CO_2 to CO, HCOOH, and CH_3COOH; low surface acidity prompted conversion of CO_2 to CH_4. The results also indicated that CO is the main intermediate species of the CO_2 photoreduction in all conditions. We have uncovered the role played by the surface acidity of Nb_2O_5 and the mechanism behind its performance for CO_2 photoreduction.

3.2 Introduction

Since atmospheric carbon dioxide (CO_2) concentration has been increasing, leading to greenhouse effects[77–79], the development of photocatalysts to prompt CO_2 reduction is promising for both environmental (reducing total CO_2 emission) and economic management. CO_2 reduction yields fuels or sustainable chemicals (CH_4, CO, CH_3OH, etc.) that are suitable for power generation or industrial processes.[80,81] However, there is a challenge that lies in an adequate photocatalyst development: improvements in the CO_2 photoconversion rates and the study on the mechanisms involved in this process are required.[10,82] The photoconversion efficiency and selectivity of catalysts towards desired products depend on their light absorption and charge separation efficiencies and spatial position of valence and conduction bands, however the catalyst surface properties also play a critical role in the charge transference process.[9,83]

The literature reports several CO_2 photoreduction approaches that use water simultaneously as a dissolution medium and electron source.[84–86] Typical setups involve the bubbling of CO_2 into alkaline medium to prompt high

reactant concentrations,[10,87] as well as the investigation of the basic-surface catalyst effects on CO_2 adsorption.[88,89] Some authors indicate that due to the CO_2 acidic character, basic catalysts are more likely for adsorption and further to react with CO_2 by electron transference. However, we propose here that acidic catalysts, due to their role as an electron acceptor, can be active for CO_2 reduction as well as for specific molecular bonding, which depends on their adequate charge separation when excited by light.[90–92] To the best of our knowledge, Nb_2O_5 is a semiconductor that fulfills both features: it shows good performance as a catalyst due to its very acidic surface [48,93–95] and exhibits photoactivity for pollutant degradation. [13,67,72,96] Nevertheless, studies on the photocatalytic activity of Nb_2O_5 for CO_2 reduction have not been published yet.

We describe here that Nb_2O_5 can be a very active catalyst for CO_2 photoreduction with formation of preferential byproducts driven by the Nb_2O_5 surface acidity. A series of Nb_2O_5 catalysts were synthesized through a modified peroxide sol−gel method. Our results support a deep discussion about the role of the surface acidity of photocatalytic semiconductors, providing important insights into the design of selective CO_2 reduction systems.

3.3 Experimental

3.3.1 Synthesis

The precursor ammonium niobium oxalate (CBMM, Brazil) was dissolved in distilled water (140 mL) under vigorous stirring and then 60 mL of hydrogen peroxide was added to the solution, leading instantaneously to a transparent yellow solution, which denotes formation of niobium peroxo complex. Afterward, the niobium peroxo-complex solution was heated at 80 ºC for 1 h and a yellow gel was formed. The product was allowed to cool down to room temperature, recovered by centrifugation, and dried in air at 60 ºC for 12 h. The final product is reactive niobium pentoxide with surface modified with peroxo groups (namely Nb-OPM).[13,97] This Nb-OPM was annealed at 150,

200, 300, 400 and 600 ºC for 2 h using heating rate of 10 ºC min^{-1} in alumina crucible boats. Samples were referred to as Nb-*x*, where *x* represents the annealing temperature.

3.3.2 Characterizations

The crystalline phases were characterized by X-ray diffraction (XRD) over the 2θ range from 10 to 80º using a Shimadzu XRD-6000 diffractometer operating with CuKα radiation. Thermal analyses were carried out using a TGA Q500 thermogravimetric analyzer (TA Instruments) in air atmosphere from room temperature up to 700 ºC using heating rate of 10 ºC min^{-1}. A Fourier Transform Infrared spectrometer (FTIR) (Bruker VERTEX 70) was used to investigate surface changes using sample-containing KBr disks with 64 scans and 4 cm^{-1} resolution in the 4000 - 400 cm^{-1}. Raman spectroscopy was performed with a FT-Raman spectrometer (Bruker RAM II with a Ge detector), equipped with a Nd:YAG laser with wavelength centered at 1064 nm generating a power of 150 mW at a resolution of 4 cm^{-1}. Sample morphology and particles size were analyzed by field emission gun scanning electron microscopy (FEGSEM) JEOL JSM 6701F. The materials were also characterized by transmission electron microscopy (TEM), using an FEI Tecnai G2 F20 microscope. N_2 adsorption–desorption isotherms were measured with a Micromeritics ASAP 2020 analyzer at 77 K. Samples were previously degassed at 80 ºC under vacuum until a degassing pressure <10 μmHg. The Brunauer–Emmett–Teller (BET) method was used to calculate the specific surface area (S_{BET}). The total pore volume (Vp) was estimated from the adsorbed N_2 amount at a relative pressure P/P_0 of 0.98. UV-visible diffuse reflectance spectroscopy (DRS) was measured at room temperature from 200 to 800 nm in a Varian Cary 5G spectrophotometer in diffuse reflectance mode (R). CHN analyses were conducted on a Perkin Elmer 2400 elemental analyzer.

The total amount of acid sites in the Nb_2O_5 samples was measured by the ionic-exchange procedure followed by titration of the acid species released from the solid acid in alkaline solution using a calibrated pH meter (QX 1500 Plus Qualxtron).[44,98] First, 0.1 g of samples were placed in a vial containing 10 mL of 0.1 mol L^{-1} NH_4OH solution. The vial was sealed and kept under constant stirring for 12 h and the resulting suspension was titrated with 0.1 mol L^{-1} HCl solution. The total acidity was calculated using the following equation:[44,98]

$$Cas = \frac{[(C_{NH4OH})(V_{NH4OH})]-[(C_{HCl})(V_{HCl})]}{m_{cat}} \quad \text{Eq. 1}$$

where Cas is the acid sites concentration, C_{NH4OH} is the NH_4OH concentration (mol L^{-1}), C_{HCl} is the HCl concentration (mol L^{-1}), V_{NH4OH} represents the NH_4OH solution volume, V_{HCl} is the HCl solution volume and m_{cat} is the sample amount (g).

3.3.3 CO_2 photoreduction

The CO_2 photoreduction was performed in a cylindrical steel reactor covered with borosilicate glass with 225 mL total volume. In brief, 0.1 g of catalyst were suspended in 100 mL of distilled water. High purity CO_2 was bubbled into the reactor for 20 min to expel the remaining gases and saturate the water inside the reactor. The reactor was then uniformly illuminated from the inside using a UVC lamp (PHILIPS 5W) protected by a quartz tube with a maximum wavelength of 254 nm (0.167mW/cm^2) (FIGURE 3.1).

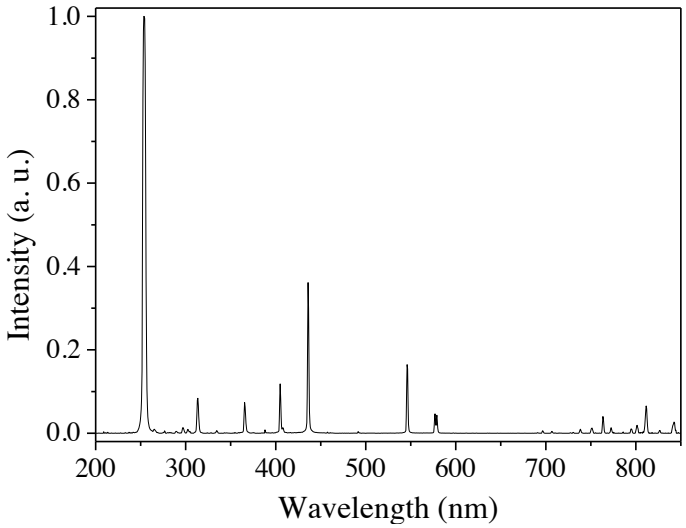

FIGURE 3.1 - Ultraviolet light spectrum used in all experiments was measured with a StellarNet EPP2000C spectroradiometer.

The photocatalytic performance of the Nb_2O_5 samples was monitored every 60 min for 6 h by collecting 0.3 mL of the gaseous sample with a watertight syringe, which was injected into a gas chromatograph (GC) to analyze the amount of CO and CH_4 formed inside the reactor. The experiments were also conducted in the absence of catalyst and light and no appreciable amounts of products could be detected, indicating that both are required for the photocatalytic CO_2 reduction. To determine the amount of CO_2 converted into hydrocarbons or carbon monoxide, the equation described below was used, taking into account the concentration of the products formed and the concentration of CO_2 in water, assuming that the solution is saturated with CO_2.

$$Aumont\ of\ CO2\ Converted[\%] = \frac{Product\ concentration}{CO2\ concentration} x\ 100 \qquad \text{Eq. 2}$$

Gaseous products were determined by gas chromatography (GC, Varian, CP-3800) equipped with a thermal conductivity detector (TCD) and a flame ionization detector (FID), using a packed column (HayeSep N (0,5 m x 1,8")) with flow rate of 30 mL min^{-1} for H_2, 300 mL min^{-1} for air and 30 mL min^{-}

[1] for N_2. The injector temperature was set at 150 ºC, while the TCD and FID detector temperatures were 200 ºC and 150 °C, respectively. The gas products were analyzed by the external standard method.

High-performance liquid chromatography (HPLC-LC-20AD, Shimadzu) was used to analyze the products formed in the liquid phase. Samples (20 μL) were collected after 6 h of CO_2 photoreduction and injected into an Aminex HPX-87H column (300 x 7.8 mm), which is suitable for carboxylic acid and alcohol determination, using dilute H_2SO_4 solution (3.3 mmol L^{-1}) as a mobile phase flowing at 0.6 mL.min^{-1}. Column and detectors were kept at constant temperature of 40 ºC. This chromatograph was equipped with a differential refractive index detector (RID-10A) suitable for alcohols quantification and a UV-Vis detector (SPD-20A, 210 nm) with deuterium lamp suitable for carboxylic acid determination.

3.4 Results and Discussion

3.4.1 Characterization of Nb_2O_5 samples

XRD patterns of Nb ammonium oxalate and Nb_2O_5 samples are shown in FIGURE 3.2 and 3.3. It is observed that the Nb ammonium oxalate precursor is crystalline, but it becomes amorphous (up to 480 ºC) when treated with hydrogen peroxide to form Nb-OPM. This indicates the proper reaction, forming a hydrated niobium pentoxide ($Nb_2O_5 \cdot nH_2O$), also known as niobic acid.[41,93,94,99] The calcination at different temperatures indicates that the hydrated niobium pentoxide is stable even at high temperatures, i.e. hydration corresponds to strongly bonded water instead of water weakly adsorbed at the niobium pentoxide structure.[44] In fact, as seen in FIGURE 3.4, TGA/DTG curves show that Nb-OPM loses around 5% weight up to 100 ºC, associated with physically/weakly adsorbed water molecules. The most significant weight loss (~20%) lies in the temperature range between 100 and 300 ºC, which is associated with residual organic molecules (CO and OCO) of the precursor and strongly

adsorbed surface water or with the crystalline oxide network.[100] Above 500 °C, there are weight losses associated with the complete oxide dehydration, which results in a crystalline material. This agrees with the XRD pattern of Nb-600 °C, which shows the formation of the pseudohexagonal phase of Nb_2O_5 with high crystallinity (JCPDS No. 07-061).[100,101] Therefore, these results indicate that samples are structurally similar from room temperature until 480 °C due to the presence of adsorbed and structural water molecules.

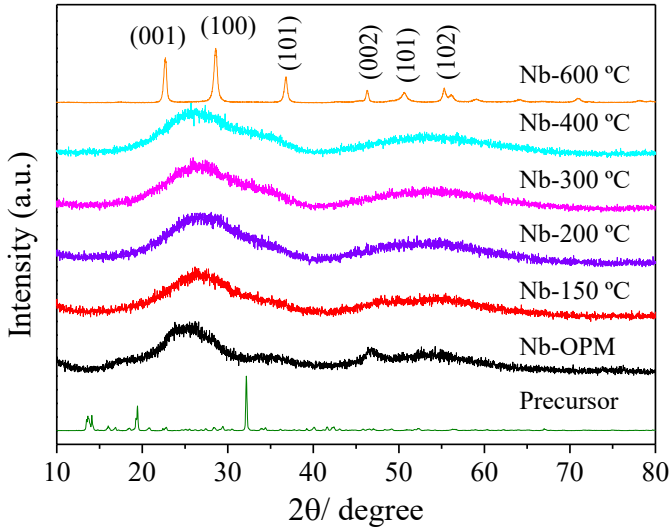

FIGURE 3.2 - XRD patterns for Nb precursor and Nb_2O_5 samples obtained by oxidant peroxide method (OPM) and after calcination from 150 to 600 ºC.

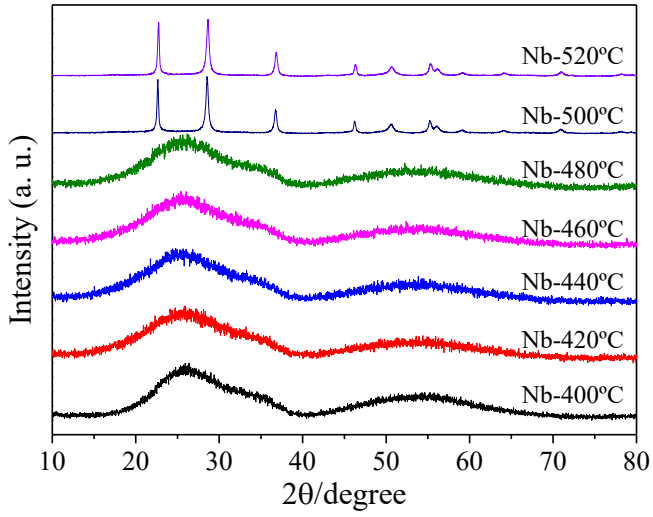

FIGURE 3.3 - XRD patterns for Nb precursor and Nb_2O_5 samples obtained by oxidant peroxide method (OPM) and after calcination from 400 to 520ºC.

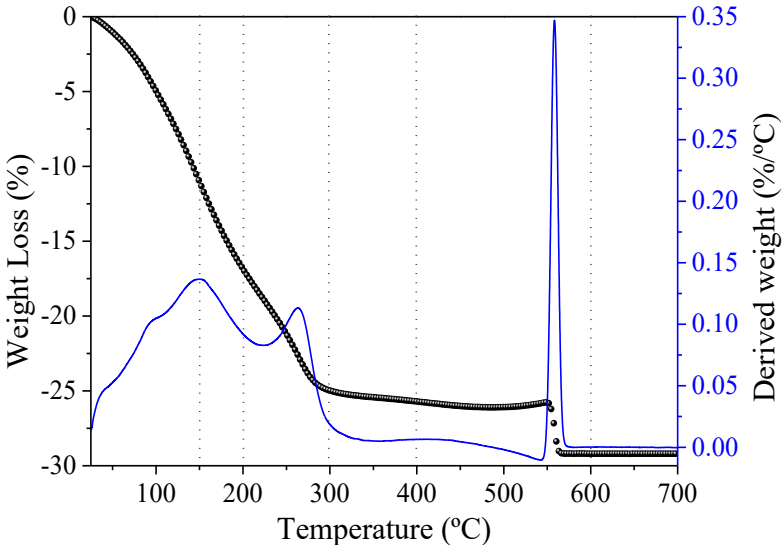

FIGURE 3.4 - Thermogravimetric Analysis of Nb-OPM. Dotted lines indicate the temperatures related to the calcined samples.

The surface water molecules are also perceived by FTIR, as seen in FIGURE 3.5. The broad vibration band in the range 3471 cm^{-1} - 3126 cm^{-1} relates to the OH-stretching vibration of H_2O molecules and structural OH-groups – this band is observed in the FTIR spectra of all samples except Nb-600 °C.[102] However, its intensity decreases with the increasing of calcination temperature, thus agreeing with the TGA results. The FTIR spectrum of Nb-400°C exhibits minimal band intensity, indicating that weakly absorbed water content is also low – although this sample corresponds to a hydrated Nb_2O_5 material, as indicated by XRD. The FTIR spectrum of Nb-600 °C presents a small shift in this band regarded to Nb-OH stretching, which agrees with the role of structural water in the thermal phase transition of Nb_2O_5.[13,44] Comparing the XRD patterns, it is seen that these amounts are not effective to keep the hydrated Nb_2O_5 phase unchanged, which may influence its final properties. Vibration bands at the range 1840–1305 cm^{-1} correspond to organic byproducts from reactants, which are almost totally eliminated at 400 °C.[103] Characteristic peaks attributed to Nb-O groups of niobium oxide are observed below 1144 cm^{-1} in all FTIR spectra.[102,103]

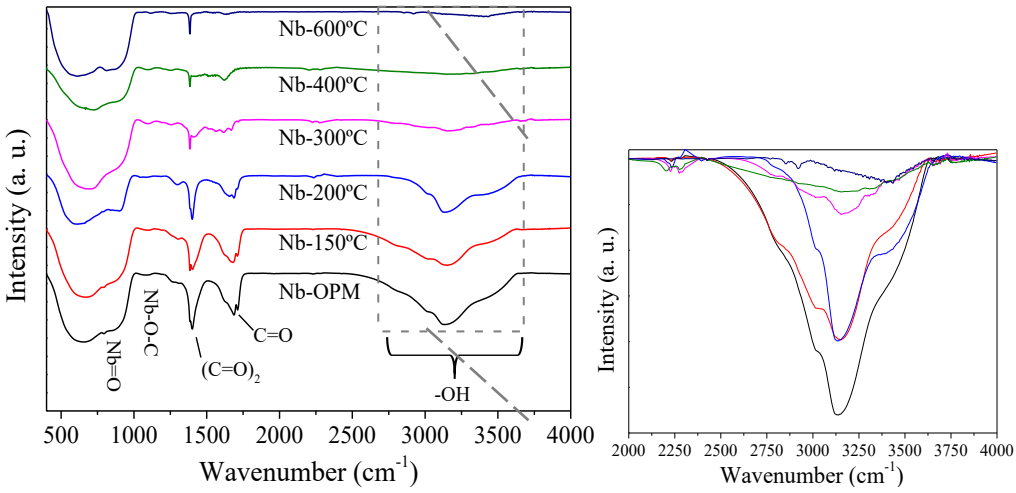

FIGURE 3.5 – Full and enlarged FTIR spectra of Nb-samples obtained without heating (Nb-OPM) and at 150, 200, 300, 400 and 600 ºC.

The strong scattering properties of the Raman spectra can be further used to analyze the phase structure features in the catalysts. FIGURE 3.6 exhibits the Raman spectra of the precursor and Nb-*x* samples. The Raman spectrum of the Nb precursor exhibits narrow and very intense peaks, which is characteristic of materials with good crystallinity, which agrees with the XRD results. The Raman spectrum of Nb-OPM shows three representative signals, one centered at 870 cm^{-1} and two centered at 656 and 586 cm^{-1}. The peak centered at 870 cm^{-1} and the peak centered at 586 cm^{-1} can be attributed to the symmetrical and asymmetric stretching of NbO_2 groups and associated with formation of di-η^2-peroxo systems with *cis*-lateral geometry. The signal centered at 656 cm^{-1} can be attributed to the asymmetric stretching of Nb-O groups in the distorted polyhedra of NbO_6, NbO_7 and NbO_8, thus characterizing the amorphous state of the materials. It is important to note that intensity of the peaks at 870 and 586 cm^{-1} signals decrease since the first thermal treatment (200 ºC), indicating the gradual loss of peroxide groups (O-O and O-H). For 600 ºC (Nb-600 ºC), the peak centered at 656 cm^{-1} shifts to 692 cm^{-1} and becomes more defined, indicating the formation of pseudohexagonal phase[103–105].

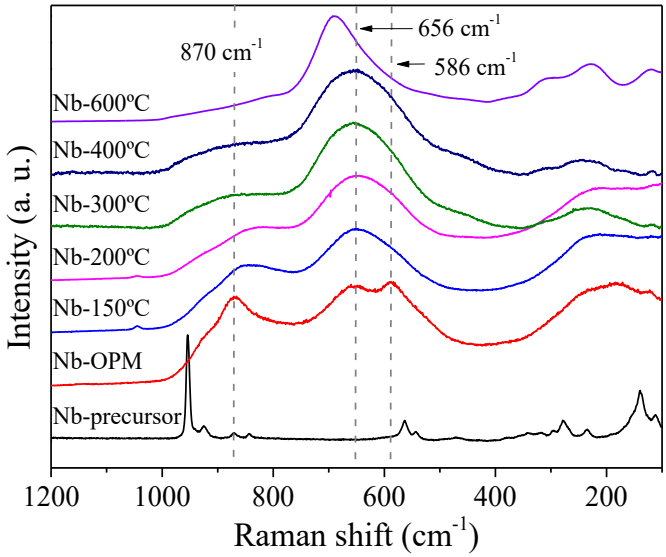

FIGURE 3.6 - Raman spectra for Nb-samples set: Nb-OPM, Nb-150ºC, Nb-200ºC, Nb-300ºC, Nb-400ºC, and Nb-600ºC.

Full-scale XPS spectra (FIGURE 3.7a) indicate the presence of Nb, C, and O at the surface of the Nb-*x* samples. The Nb 3d high-resolution XPS spectra show Nb 3d peaks at 207.6 eV and 210.3 eV, corresponding to Nb $3d_{3/2}$ and Nb $3d_{5/2}$ levels, respectively, indicating Nb^{5+} oxidation state and niobium pentoxide formation (Nb_2O_5) in all conditions (FIGURE 3.7b and FIGURE 3.8e).[61,100] In the C 1s and O 1s high-resolution XPS spectra (FIGURES 3.7c,d), the contribution of carboxyl and hydroxyl groups is noticeable, mainly for the Nb-OPM sample. The C 1s XPS spectra are shown in FIGURE 3.7c, giving three different C signals (the strongest peak at 284.8 eV is assigned to the adventitious hydrocarbon from the XPS instrument). The other two weak peaks at 286.1 eV and 288.9 eV are identified as carbon oxygen bond species (CO, OCO), probably residual contaminants of the oxalate precursor.[101,106] The O 1s region after the deconvolution curves can be seen in FIGURE 3.7d, showing two peaks characteristics of Nb-O bond (530.5 eV) as well as oxygen in hydroxyl groups (531.9 eV), assigned to water molecules adsorbed at the Nb-*x* sample surfaces.[106,107] In both cases (C 1s and O 1s), the increase in the annealing temperature decreases the intensity of the peak attributed to carboxyl and

hydroxyl groups, as observed in FIGURES 3.8a-d). This corroborates with the TGA results, that is, the increase in temperature leads to loss of weakly adsorbed water molecules, followed by loss of strongly adsorbed water molecules with carboxyl groups and finally the total crystallization of the Nb-*x* samples, as confirmed by XRD.

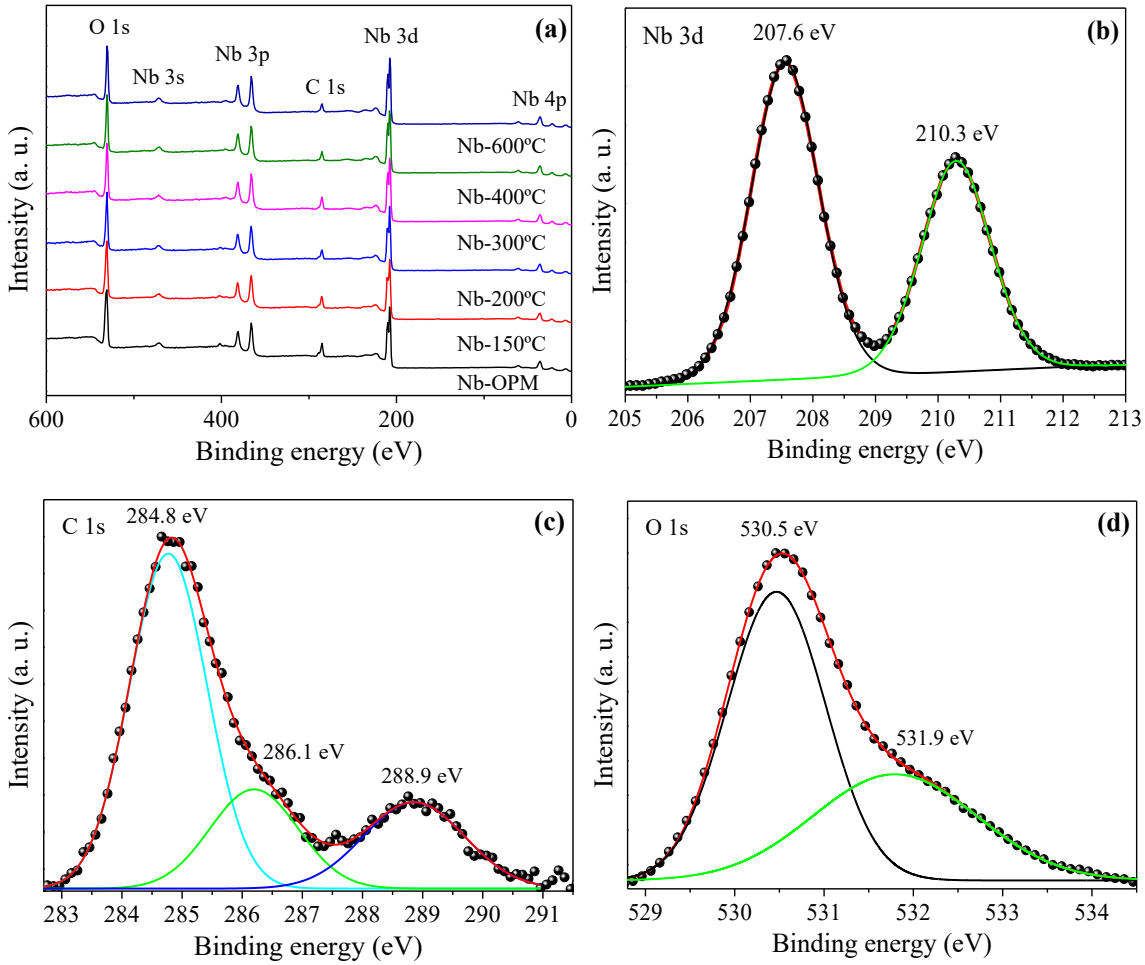

FIGURE 3.7 – (a) XPS survey spectra of synthesized samples and high-resolution XPS spectra with deconvolution curves for (b) Nb 3d, (c) C 1s and (d) O 1s of the Nb-OPM sample.

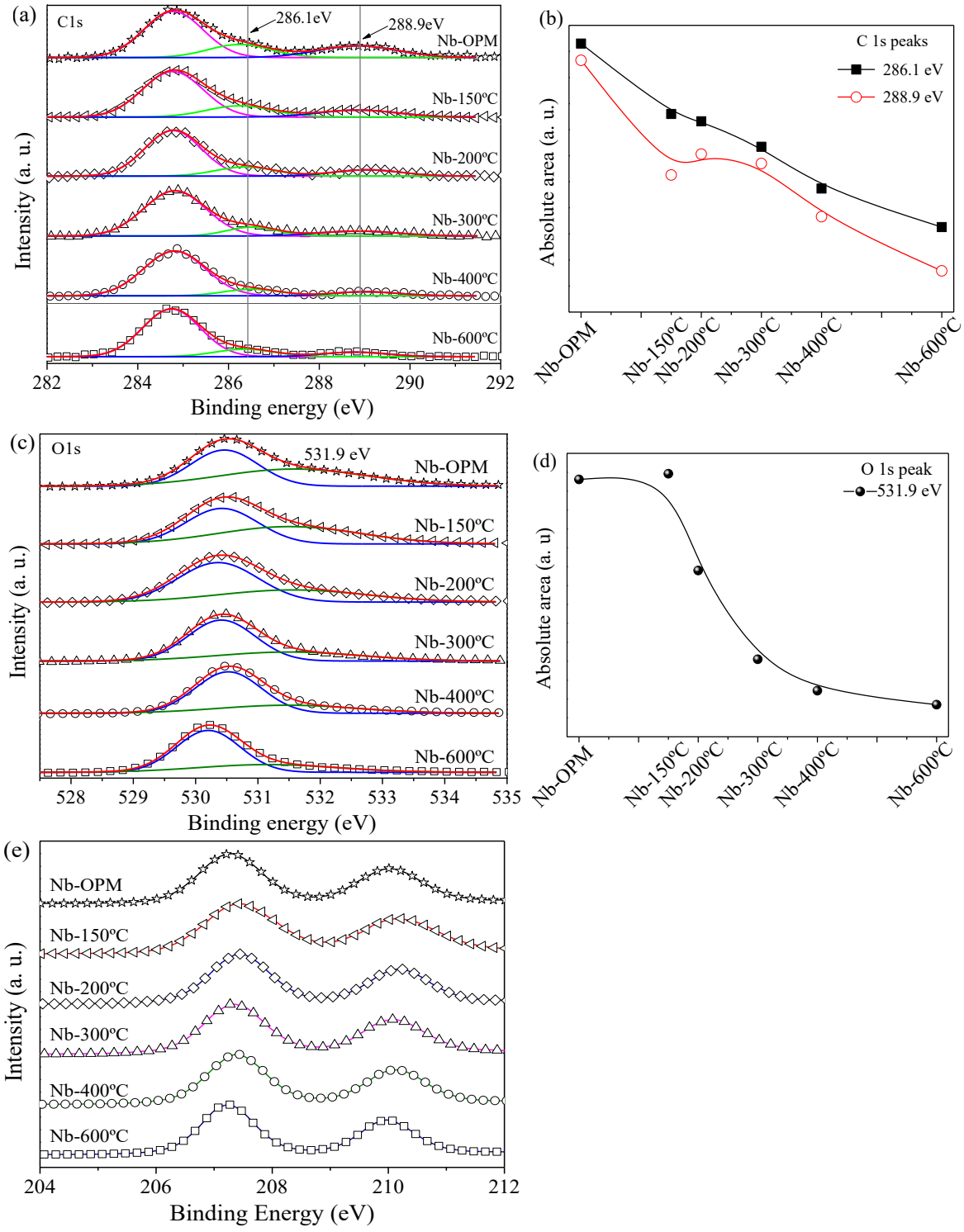

FIGURE 3.8 - The XPS high resolution spectra of the C1s (a), O1s (c), and Nb 3d (e) regions from the synthesized samples, and analysis of peaks area C1s (286,1 and 288.9 eV) (b), and peak area O1s (531,9 eV) (d).

Bandgap values obtained by interpolation of diffuse reflectance spectroscopy curves (FIGURE 3.9) show that the energies required to excite each photocatalyst are quite similar (TABLE 3.1), except for Nb-OPM, which is influenced by remnant peroxocomplex structure. Therefore, from 150 ºC to 600 ºC, the differences are minimal, denoting the similar electronic property among the Nb-*x* samples.

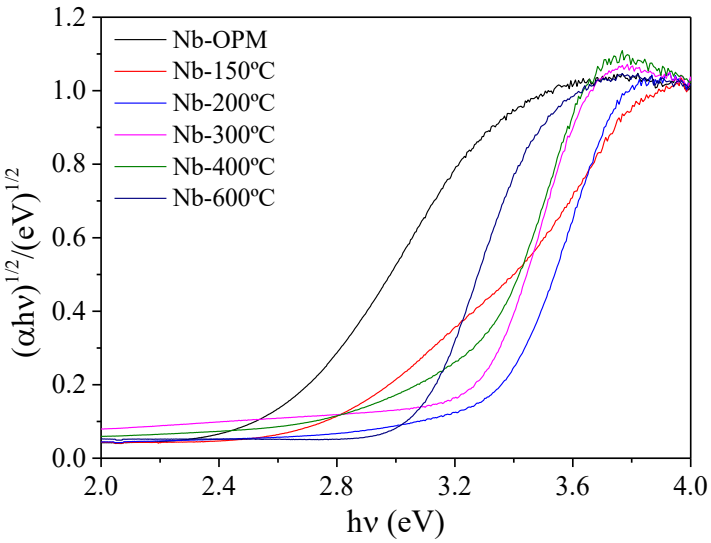

FIGURE 3.9 - DRS curves applying the Tauc model to estimate band gap values of synthesized Nb_2O_5 at different temperatures.

TABLE 3.1 - The surface areas, pore volumes and electronic properties of Nb_2O_5-OPM calcined at different temperature.

Sample	**S_{BET} (m^2/g)[a]**	**Vp(cm^3/g)[b]**	**Bandgap (eV)**
Nb-OPM	18	0.012	2.6
Nb-150 ºC	13	0.013	3.0
Nb-200 ºC	11	0.012	3.0
Nb-300 ºC	11	0.013	3.2
Nb-400 ºC	10	0.013	3.2
Nb-600 ºC	20	0.037	3.1

[a] Surface area obtained by BET method;
[b] Total pore volume;

The morphology and size of the Nb_2O_5 particles were examined by scanning electron microscopy (SEM) and transmission electron microscopy (TEM). As shown in FIGURE 3.10 AND 3.11, all samples are micrometric agglomerates of nanoparticles. The Nb-600 ºC sample is composed of denser nanometric agglomerates than Nb-OPM and Nb-400 ºC samples, thus indicating growth of Nb_2O_5 nanoparticles at high temperatures (recrystallization and coalescence process). TABLE 3.1 shows that the specific surface area values decrease with the increasing calcination temperature (up to 400 ºC), which may be related to the decrease of sample surface roughness caused by the growth of the particles. However, the Nb-600 ºC sample exhibits an increase in the specific surface area, indicating that the nucleation-recrystallization processes induced the formation of a phase with lower density. The total pore volume values of the samples calcined up to 400 ºC are similar (TABLE 3.1), however, they are lower than that of the Nb-600 ºC sample, indicating that water molecules or precursor residues are totally eliminated at 600 ºC (TABLE 3.2), leaving the pores free, and consequently, increasing the pore volume and surface area.

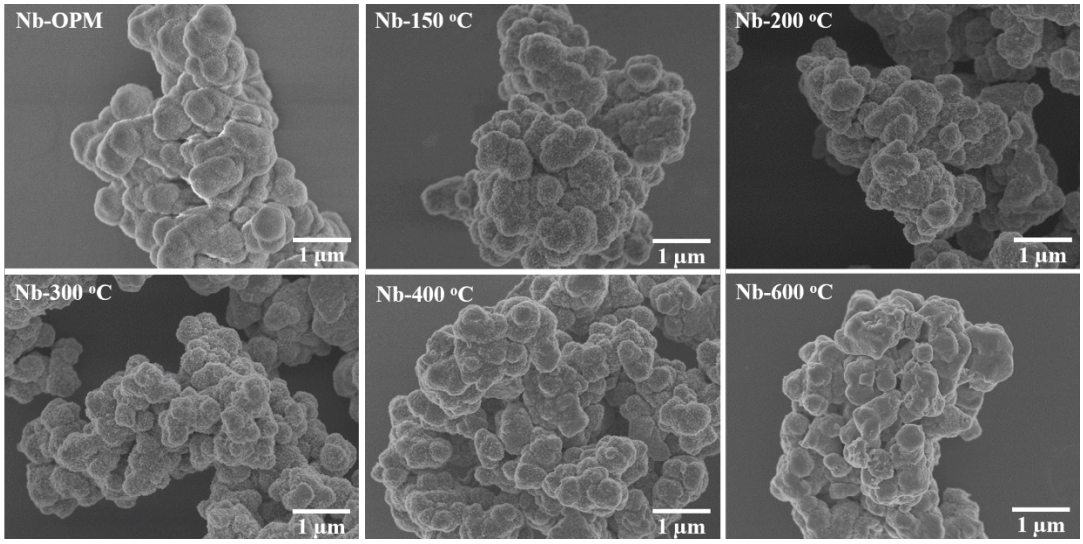

FIGURE 3.10 - Representative SEM images of Nb_2O_5 prepared at different temperatures.

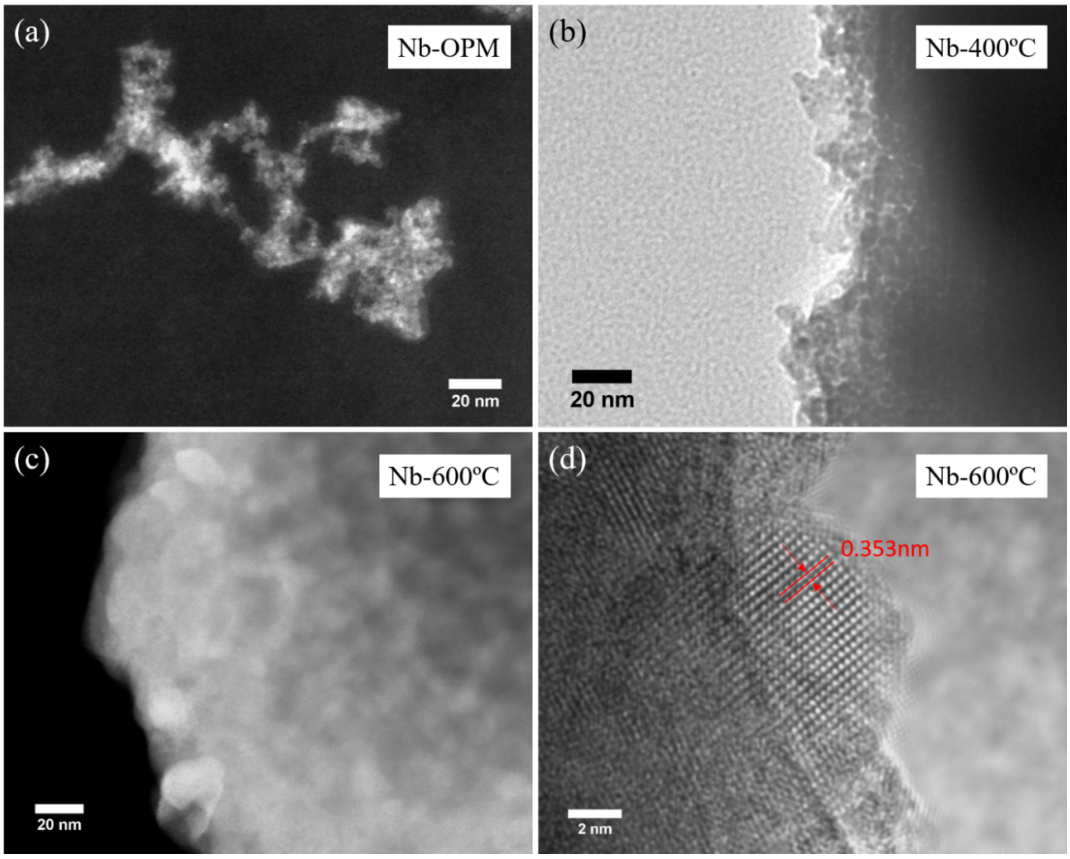

FIGURE 3.11 - Transmission electron microscopy (TEM) images of (a) Nb-samples obtained without heating (Nb-OPM) and annealed at (b) 400 and (c) 600 ºC. (d) High-magnification transmission electron microscopy (HRTEM) image of Nb-600 ºC sample.

TABLE 3.2 - Quantification of the carbon (C), hydrogen (H) and nitrogen (N) elements of the surface of the photocatalysts synthesized via CHN elemental analysis.

Samples	Amount (%)			Amount (µmol g^{-1})		
	C	N	H	C	N	H
Nb-OPM	1.05	2.39	2,81	87.4	170.6	$2.8x10^{-3}$
Nb-150ºC	1.32	2.76	1.46	109.9	197	$1.4x10^{-3}$
Nb-200ºC	1.31	2.30	1,10	109.1	164.2	$1.09x10^{-3}$
Nb-300ºC	0.82	1,58	0.34	68.3	112.8	$0.33x10^{-3}$
Nb-400ºC	0,83	1,69	0,17	69.1	120.7	$0.17x10^{-3}$
Nb-600ºC	*	*	*	*	*	*

*Nb-600ºC sample does not have the elements analyzed.

3.4.2 Photocatalytic performance of Nb_2O_5 samples

FIGURE 3.12 shows the photocatalytic performance of the Nb-*x* samples for CO_2 reduction to CO and CH_4 in aqueous medium. It is observed a preference for CO formation after 6 h of reaction under UV irradiation. However, the CO production efficiency decreases with the increasing of the annealing temperature.

The Nb-OPM sample shows the highest performance towards CO production (over 10.7 mmol L^{-1} g^{-1}), compared to the other samples, as can be seen in FIGURE 3.12a. This behavior may be associated with the photoreduction of organic groups (oxalate) present at the catalyst surface and not with the direct reduction of CO_2 molecules, since the vibrations attributed to the oxalate groups decrease after the reaction (FIGURE 3.13).[13,103] To confirm this hypothesis, the stability of Nb-OPM was evaluated over five 6-h photocatalysis cycles, (FIGURE 3.14a). It is observed that the CO production decreases abruptly up to the third cycle, leveling off in the fourth and fifth cycles. This demonstrates that part of the CO produced over the photocatalysis relates to the organic groups at the catalyst surface. However, even after the fifth photocatalysis cycle the Nb-OPM sample still prompts CO production rate (257 µmol L^{-1} g^{-1}).[108–110]

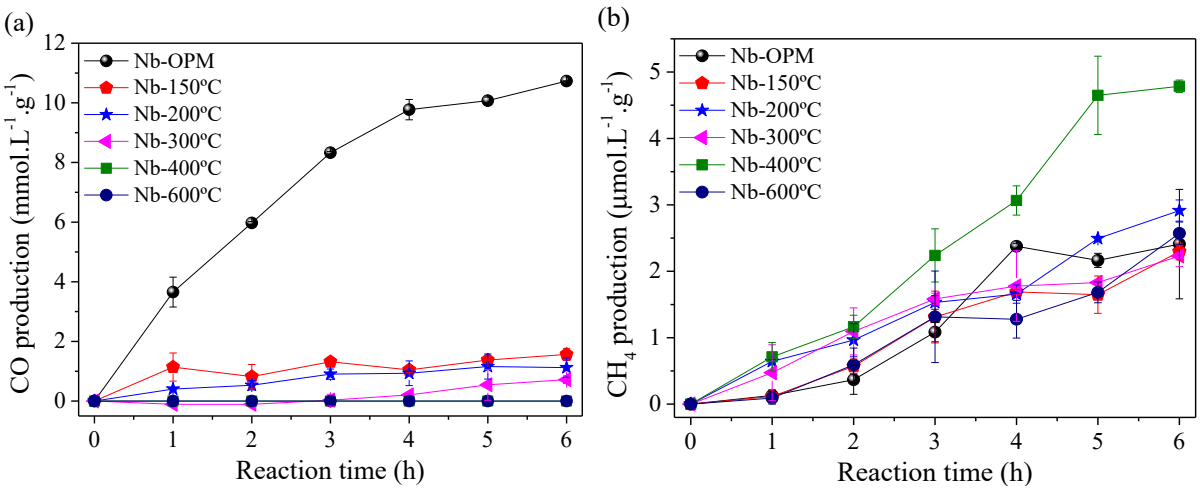

FIGURE 3.12 - Gaseous byproducts of CO_2 photoreduction according to the catalyst: (a) CO and (b) CH_4.

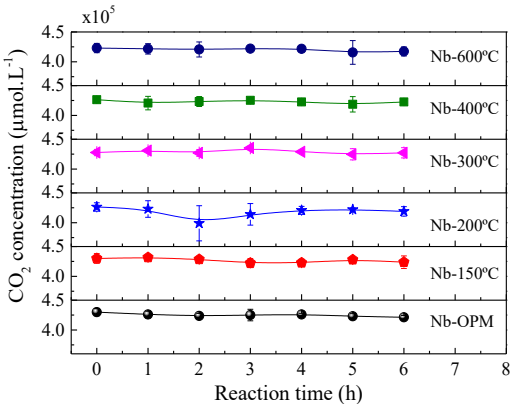

FIGURE 3.13 - The amount of CO_2 inside the reactor during the photocatalysis process.

An important aspect is the CO production yield stabilization after 4-h of photocatalysis (FIGURE 3.12a) for Nb-OPM. This should be interpreted by the availability of CO_2 for reduction *versus* CO solubility in water. As the CO_2 solubility (1.45g L^{-1}) in aqueous medium is higher than the CO solubility (0.027g L^{-1}), higher CO_2 amount is available to react with the catalysts.[111,112] Therefore, CO is formed and easily saturates the medium, most of the CO molecules diffuse to the photoreactor headspace, demonstrating the tendency for a plateau after 4 h. Amount of CO_2 converted data are depicted in TABLE 3.3, considering that each 1 mol of CO or CH_4 is produced at the expense of 1 mol of CO_2.[113,114].

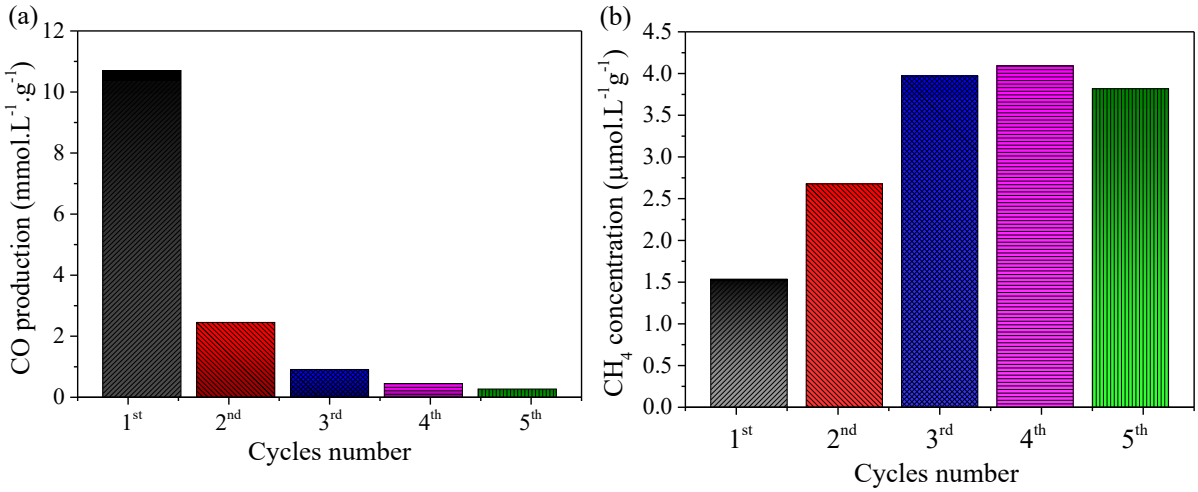

FIGURE 3.14 - Nb-OPM stability during 5 reusing cycles. (a) CO formation and (b) CH_4 production.

Regarding the CH_4 production, Nb-OPM initially presents photocatalytic activity similar to the other samples, except for Nb-400 ºC which prompts a CH_4 production of 4.78 μmol.L^{-1}.g^{-1}. This may be associated with the residual organic molecules, decreasing CO_2 interaction in aqueous medium and blocking the catalytic sites. This is confirmed by the presence of oxalate peaks (1840 – 1305 cm^{-1}), which are reduced after the CO_2 photoreaction with Nb-OPM, indicating the presence of related organic groups. However, as observed in FIGURE 3.14, from the second cycle onwards there is an increase in the CH_4 production, confirming that these organic molecules block the interaction of CO with the catalyst surface. On other hand, after the removal of organic residues the CO can be adsorbed on the Nb_2O_5 surface, and the CO can be converted to CH_4. This pathway is thermodynamically and kinetically more favorable than the reduction of CO_2 towards CH_4.[31,85,115,116] Inversely to the plateau for CO production (FIGURE 3.12a), the CH_4 production tends to increase gradually, especially for Nb-400 ºC (FIGURE 3.12b). This suggests that the CH_4 production relates to the CO excess in solution, leading to a basic mechanism for CH_4 production in which CO is the intermediary species in the catalytic system.[10,117] Since Nb-400 ºC has a few surface hydroxyl groups, this suggests that the CO to CH_4 conversion mechanism probably depends on the affinity of CO to the catalyst surface.[31,80,108,118–120] This is confirmed by the higher photocatalytic activity of Nb-400 ºC for CH_4 production since this sample still exhibits the same crystalline structure at 400 ºC (niobic acid, Nb_2O_5·$n$$H_2O$) but with minor surface hydroxyls and organic adsorbates. Comparing to the Nb-600 ºC sample, which is also free of these organic groups but shows poor catalytic activity, the results confirm that niobic acid is the catalytic active phase, and that the surface acidity plays an important role in the CO_2 photoreduction selectivity.[41,121]

Similar to the gas phase, two products are observed in the liquid phase (FIGURE 3.15), namely, formic acid (HCOOH) and acetic acid (CH_3COOH), with a very similar tendency. The highest liquid-phase product yields are obtained with the most hydroxylated catalysts (Nb-OPM and Nb-150 ºC), denoting the advantage of the coordinately unsaturated-surface samples. Surprisingly, the Nb-400 ºC sample (which prompted CH_4 production at a highest extent) shows decreased activity for liquid-phase products formation, which highlights the role of the surface hydroxyl group amount in the catalyst selectivity. This role is probably related to the surface acidity (TABLE 3.3), suggesting that Nb-OPM is the most effective acid catalyst, followed by Nb-150 ºC and Nb-200 ºC. This decrease was effective to suppress the CO production at a very low level compared to Nb-OPM, but it is still remarkable that Nb-150 ºC is active for HCOOH and CH_3COOH production. The surface acidity tends to decrease as the annealing temperature increase, and the activity towards HCOOH and CH_3COOH formation as well.

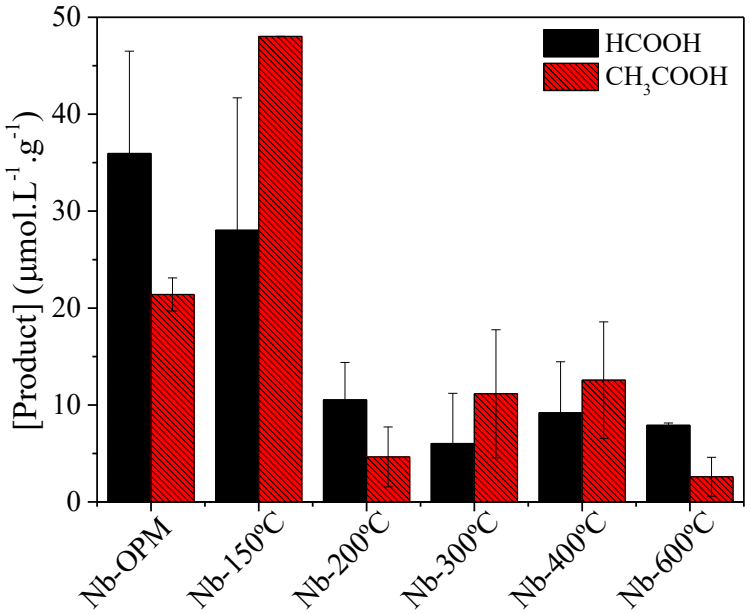

FIGURE 3.15 - Peak amounts of the main compounds obtained by photocatalytic reduction of CO_2 with H_2O on synthesized Nb-samples, after 6 hours.

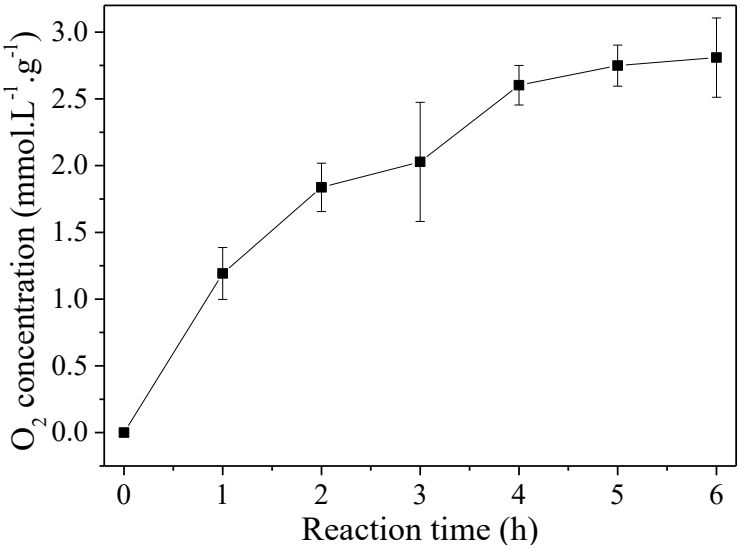

FIGURE 3.16 - Evolution of O_2 concentration promoted by the Nb-OPM sample during the CO_2 photoreduction in water.

TABLE 3.3 - Total acid site concentration (C_{as}) of synthesized samples and amount of CO_2 converted after 6 hours of reaction.

Samples	**C_{as} (mmol/g)**	**Amount of CO_2 Converted (%)**			
		CO	**CH_4**	**CH_3COOH**	**HCOOH**
Nb-OPM	2.5	9.75	2.2	21.6	18.4
Nb-150ºC	1.4	1.42	2.1	34.3	43.7
Nb-200ºC	1.2	1.02	2.7	7.1	2.2
Nb-300ºC	0.8	0.65	2.0	2.2	5.9
Nb-400ºC	0.4	*	4.4	11.7	4.9
Nb-600ºC	0.0	*	2.3	7.3	1.1

It is noteworthy that the yields of formic and acetic acid were larger in all conditions than the CH_4 yields. With basis on this comparison, one could notice that the CH_4 production, in any condition, is very below the production of other compounds, reinforcing the hypothesis that the mechanism involves the successive reactions of CO with H^+, leading to formic and acetic acid. It is impressive that the production of these intermediate species is remarkably high, thereby showing the versatility of Nb_2O_5 as a catalyst for CO_2 photoreduction.

It is demonstrated that semiconductors, such as Nb_2O_5, having acidic surface can be used as photocatalysts for conversion of CO_2 to CO or

hydrocarbons. Thus, we propose a reaction mechanism (SCHEME 3.1) based on several steps: in the 1st step, there is physisorption of the CO_2 molecules on the photocatalyst surface, which is comprised of a high number of hydroxyl groups. Afterwards (2nd step), the catalyst is activated by UV radiation, generating charge carriers, which induce reductive and oxidative processes. In the valence band, oxygen from water is oxidized to molecular oxygen (FIGURE 3.16) while the excited electron are transfers to the CO_2 molecules, generating $CO_2^{\bullet-}$ species.[122,123] The $CO_2^{\bullet-}$ species are reduced through a series of complex and elementary steps involving the transfer of an electron, a proton or a hydrogen radical, as well as the breakage of C-O bonds and the creation of new C-H bonds [10,31,36]. Several of the intermediates are radical species whose recombination at different stages partially explains the number of possible pathways and end products.

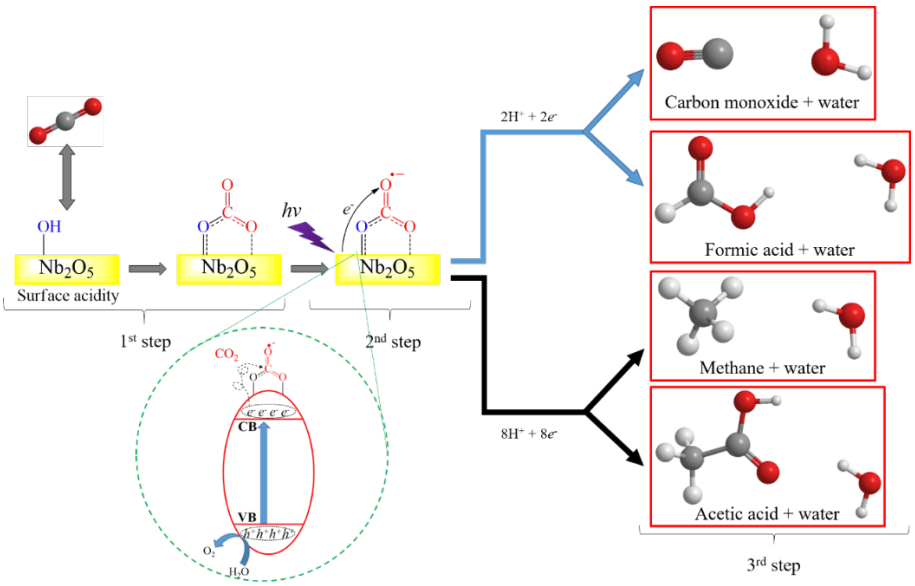

SCHEME 3.1 - Proposed pathways for CO_2 photoreduction adsorbed on the acid surface of Nb_2O_5.

Therefore, based on the results presented here, we propose that carbon monoxide (CO) and formic acid (HCOOH) are the first species formed from the CO_2 photoreduction in gas and liquid phase, respectively. This is

probably due to the fact that these reactions require only two electrons and two protons (3rd step).[36,124]

The other products such as methane (CH_4) and acetic acid (CH_3COOH) are more difficult to be formed in this system, once this requires eight electrons and eight protons as well as the adsorption of CO on the catalyst surface or the CO dissolution in the aqueous medium (3rd step).[36,125–127] The high CH_3COOH yields obtained from catalysts with the highest surface acidity may be associated with the fact that the reactor headspace saturation increases the CO partial pressure and its solubility in the aqueous medium.[113,114] Catalysts with poorly hydroxylated surfaces seem to be more active for CO adsorption, which could explain the increased CH_4 production observed for Nb-400ºC.

3.5 Conclusion

We have shown for the first time that Nb_2O_5 is an active catalyst for CO_2 photoreduction in which the Nb_2O_5 surface acidity plays a significant role in its selectivity towards byproducts. This effect is probably related to the formation of intermediates due to the CO_2 adsorbed onto the Nb_2O_5 surface by coordination of oxygen atoms and further reaction with H^+. The CO_2 photoreduction efficiency was surface acidity-dependent: high surface acidity prompted conversion of CO_2 preferentially to CO, HCOOH, and CH_3COOH, while low surface acidity prompted CO_2 conversion preferentially towards CH_4. It was demonstrated that CO is the main intermediate species of the CO_2 photoreduction in all conditions. The high activity of the acid Nb_2O_5 catalysts in comparison with other systems reported in the literature indicates that the photocatalytic properties of Nb_2O_5 deserve further investigation for CO_2 reduction.

4 CHAPTER II: Increasing photoactivity through g-C_3N_4:Nb_2O_5 heterojunctions

The content of this chapter is an adaptation of the article entitled **"g-C_3N_4/Nb_2O_5 heterostructures tailored by sonochemical synthesis: Enhanced photocatalytic performance in oxidation of emerging pollutants driven by visible radiation"** by Gelson T.S.T. da Silva, Kele T. G. Carvalho, Osmando F. Lopes, and Caue Ribeiro, published for Applied Catalysis B: Environmental.

Reference: Applied Catalysis B: Environmental 216 (2017) 70–79

Applied Catalysis B: Environmental 216 (2017) 70–79

Contents lists available at ScienceDirect

Applied Catalysis B: Environmental

journal homepage: www.elsevier.com/locate/apcatb

g-C_3N_4/Nb_2O_5 heterostructures tailored by sonochemical synthesis: Enhanced photocatalytic performance in oxidation of emerging pollutants driven by visible radiation

Gelson T.S.T. da Silva [a,b], Kele T.G. Carvalho [b], Osmando F. Lopes [b,c], Caue Ribeiro [b,*]

[a] Departamento de Química, Universidade Federal de São Carlos – UFSCar, Rodovia Washington Luiz, km 235, CEP 13.565-905, São Carlos, SP, Brazil
[b] Laboratório Nacional de Nanotecnologia para o Agronegócio (LNNA) – Embrapa Instrumentação, Rua XV de Novembro, nº 1452, CEP 13.561-206, São Carlos, SP, Brazil
[c] Instituto de Química de São Carlos, Universidade de São Paulo – USP, Av. Trabalhador São Carlense, nº 400, CEP 13560-970, São Carlos, SP, Brazil

4.1 Abstract

In this study, g-C_3N_4/Nb_2O_5 heterostructures were successfully prepared by a sonochemical method based on surface charge-induced heteroaggregation. Under visible irradiation, the heterostructured g-C_3N_4/Nb_2O_5 samples exhibited higher activity in the photooxidation of the drug amiloride (AML) and rhodamine B dye (RhB), compared to the pure g-C_3N_4 and Nb_2O_5 phases. The enhanced photocatalytic activity of the heterostructures could be attributed to the effective formation of heterojunctions between the g-C_3N_4 and Nb_2O_5 semiconductors, causing the migration of photogenerated electrons and holes, hence increasing their lifetimes. Formation of the type-II heterostructure was confirmed by time-resolved photoluminescence, in which the 3CN:1Nb heterostructure showed the longest electron/hole pair lifetime. The 3CN:1Nb and 1CN:3Nb heterostructures exhibited high stability even after four cycles of reuse in RhB dye and drug AML oxidation, respectively. In summary, the combination of g-C_3N_4 with Nb_2O_5 to produce a type-II heterostructure is a good strategy to overcome important challenges in photocatalysis.

4.2 Introduction

The presence of organic contaminants such as pesticides, pharmaceuticals, and dyes in rivers and lakes, even at low concentrations, can seriously affect human health and the environment. Amiloride, a drug extensively used for the treatment of hypertension, belongs to a class of pharmaceutical compounds that are often found in wastewater and can adversely affect water quality [128–130]. Rhodamine B, a dye used in the textile industry, is another organic pollutant found in wastewater that can be prejudicial to the environment and human health because of its resistance to biodegradation and its potential carcinogenicity [131,132]. There is therefore a need for the development of efficient treatment technologies for the removal of these compounds from wastewater. Advanced oxidation processes (AOPs) such as heterogeneous

photocatalysis have attracted great interest for this purpose, especially using semiconductors that can be actived under visible irradiation. Graphitic carbon nitride (g-C_3N_4) has been identified as a useful organic semiconductor that can be easily obtained by polymerization involving the thermal condensation of nitrogen-rich precursors such as cyanamide, urea, and melamine [64,133,134]. Much of the interest in the use of this material is due to its low band gap value (E_g ~2.7 eV) and suitable band structure to drive reactions involving reduction (such as artificial photosynthesis and water splitting) or oxidation (such as degradation of organic pollutants) [135,136].

However, bulk g-C_3N_4 exhibits a low surface area and fast recombination of photogenerated electron/hole pairs, which reduce its photocatalytic activity [137]. Strategies such as morphology control, exfoliation, non-metal doping, and deposition of metal nanoparticles have been proposed in order to improve its efficiency in photocatalytic processes [138–141]. An effective way to increase the photoactivity is to couple g-C_3N_4 with another semiconductor by means of type-II heterojunctions [142]. In this type of heterojunction, the potential of the conduction and valence bands of a semiconductor is lower than that of the other semiconductor [142,143], and promotes photogenerated charge transfer between the semiconductors, longer photogenerated electron/hole pair lifetimes, and a consequent enhancement of photocatalytic properties [82,144–146].

Among various semiconductors, niobium oxide (Nb_2O_5) is a promising material for coupling to g-C_3N_4. Nb_2O_5 is an n-type semiconductor with an optical band gap of ~3.2 eV, high specific surface area, high surface acidity, and good photoactivity towards the degradation of organic pollutants [13,95,147]. Nb_2O_5 powder has been incorporated in many composites, such as Nb_2O_5/ZnO [147], TiO_2/Nb_2O_5 [148], Nb_2O_5/CuO [60], Nb_2O_5/RGO [149], and Nb_2O_5/iron oxide [150], resulting in significant increases in photocatalytic performance. However, until now there have been only two studies devoted to evaluating the

photoactivity of heterostructures formed by g-C_3N_4 and Nb_2O_5 [61,72]. Major drawbacks of the systems described previously are long synthesis times and lack of control of heterostructure formation, which can lead to poor dispersion of Nb_2O_5 particles on the g-C_3N_4 surface, as well as a large particle size, hence decreasing the activity of the photocatalysts. Therefore, the synthesis route employed to produce suitable heterostructures based on g-C_3N_4 still remains a matter of study.

The sonochemical technique offers an interesting alternative means of obtaining heterostructures of g-C_3N_4 and Nb_2O_5. This method is simple, fast, and enables highly accurate control of synthesis parameters including time, energy input, and pH. Furthermore, the application of ultrasonic irradiation induces particle deagglomeration, which increases the surface area of the materials [151–153]. The sonochemical method enables use of a surface charge-induced heteroaggregation strategy, based on the dispersion of particles by physical methods and adjustment of the pH of the medium to a value between the points of zero charge (PZC) of the materials. This maximizes the electrostatic attraction between them, favoring the effective formation of heterojunctions and control of the morphology [75,141]. However, few studies have explored this strategy for photocatalysis and, to the best of our knowledge, there are no published papers concerning heterojunction formation in a semiconductor: g-C_3N_4 system.

Therefore, the purpose of this work was to synthesize a series of g-C_3N_4/Nb_2O_5 heterostructures by a sonochemical method based on surface charge-induced heteroaggregation, and to evaluate their photocatalytic activity in the degradation of rhodamine B (RhB) dye and the drug amiloride (AML), under visible irradiation. The charge carrier dynamics was studied by time-resolved photoluminescence. Evaluation was also made of the pollutant photooxidation mechanism and the stability of the g-C_3N_4/Nb_2O_5 heterostructures.

4.3 Experimental

4.3.1 Preparation of the g-C_3N_4/Nb_2O_5 heterostructures

The g-C_3N_4 material was prepared by the thermal polymerization of urea (CH_4N_2O, Synth) in a muffle furnace under an air atmosphere from adapted method [154,155]. In a typical procedure, 10 g of urea powder was placed in a partially covered alumina crucible and heated at 550 ºC for 2 h, using a heating rate of 3 ºC.min^{-1}, resulting in a yellow powder. Nb_2O_5 powder was synthesized using the peroxide oxidant method [13]. This consisted of dissolving 2 g of ammonium niobium oxalate ($NH_4[NbO(C_2O_4)_2(H_2O)_2]\cdot nH_2O$), supplied by CBMM (Brazil) and used as the Nb precursor, in 100 mL of deionized water and 4 mL of hydrogen peroxide (H_2O_2), followed by hydrothermal annealing at 120 ºC for 12 h, as described elsewhere [13].

The g-C_3N_4/Nb_2O_5 heterostructures were prepared using the surface charge-induced heteroaggregation method [75], in which opposite surface charges are the driving force (by electrostatic interaction) for the formation of heterojunctions between the g-C_3N_4 and Nb_2O_5 phases. As shown in FIGURE 4.1, there is a pH range near pH 3.6 where g-C_3N_4 has a positive surface charge, due to the incomplete condensation of amino groups [156], while Nb_2O_5 has a negative surface charge, due to the presence of surface hydroxyl groups. SCHEME 4.1 illustrates the preparation process used for the heterostructured samples.

Typically, different amounts of the as-synthesized powders (g-C_3N_4 and Nb_2O_5) were placed in a beaker containing 130 mL of deionized water. Nitric acid (0.5 mol L^{-1}) was then added to the suspension, under continuous stirring, in order to adjust the pH to 3.6, followed by ultrasonic agitation for 2 h in an ice bath. The material obtained was washed with distilled water until reaching neutral pH, centrifuged, and dried at 50 ºC overnight. The weight ratios between g-C_3N_4 and Nb_2O_5 used in the syntheses were 1:3, 1:1, and 3:1, which were labeled as 1CN:3Nb, 1CN:1Nb, and 3CN:1Nb, respectively. It was determined by

thermogravimetric analysis (FIGURE 4.2) that g-C_3N_4 contents in the CN:Nb heterostructures were approximately 37.6 , 55.2, and 62.0 wt% for 1CN:3Nb, 1CN:1Nb, and 3CN:1Nb, respectively.

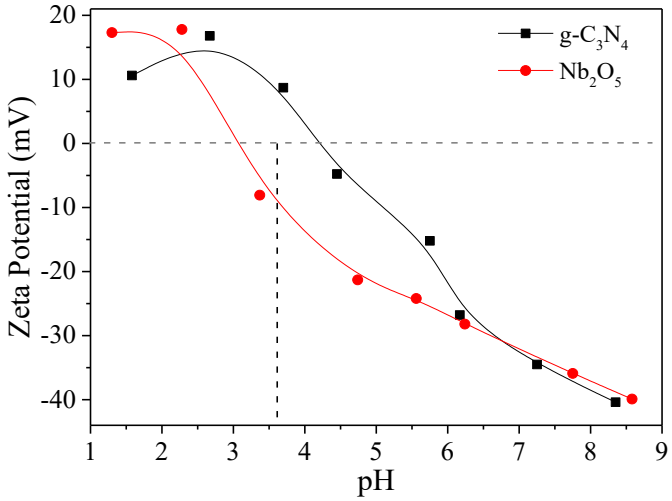

FIGURE 4.1 – Zeta potentials of g-C_3N_4 and Nb_2O_5, as a function of pH. The symbols correspond to the experimental data. The lines are provided to assist visual interpretation.

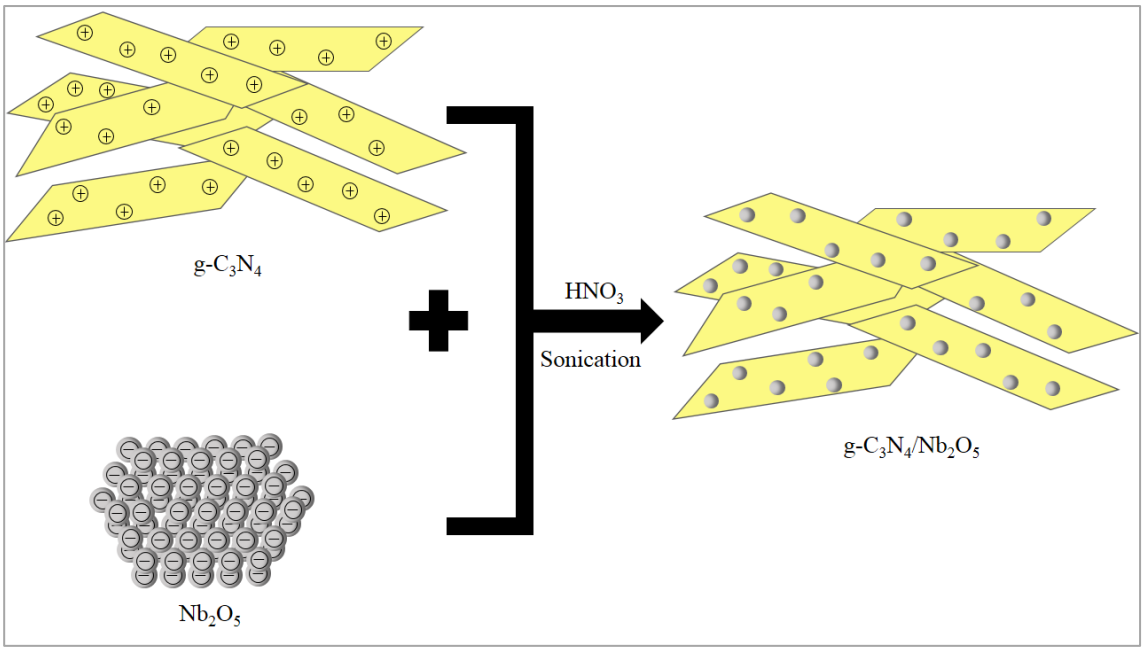

SCHEME 4.1 - Schematic illustration of the preparation process of the g-C_3N_4/Nb_2O_5 heterostructures.

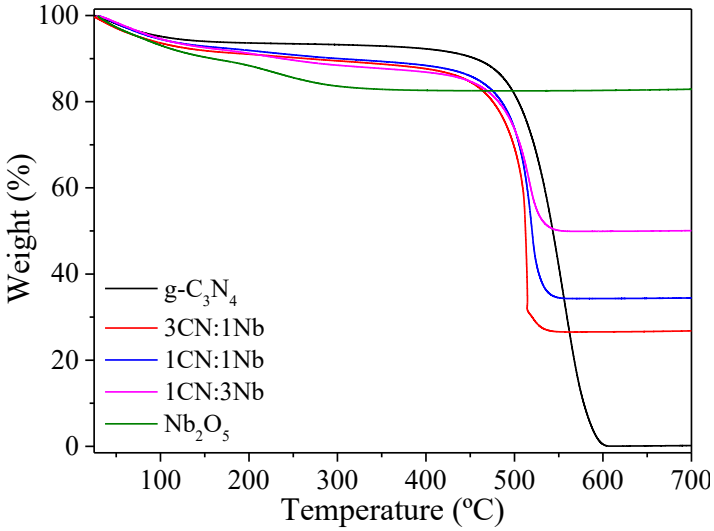

FIGURE 4.2 – Thermogravimetric curves (TG) of g-C_3N_4, Nb_2O_5, and the g-C_3N_4/Nb_2O_5 heterostructures.

The efficiency of the proposed method for obtaining heterojunctions was confirmed by preparing a physical mixture of the g-C_3N_4 and Nb_2O_5 phases by simple grinding in an agate mortar, as well as by using an ultrasonic method similar to that described above, but at neutral pH (without any pH adjustment). These materials were obtained using a CN:Nb weight ratio of 3:1 and were labeled as 3CN:1Nb-PM and 3CN:1Nb-H_2O, respectively. The photocatalytic performances of these two samples were compared to that of the 3CN:1Nb heterostructure (see in FIGURE 4.13).

4.3.2 Characterization of the materials

The materials were characterized by X-ray diffraction (XRD) using a Shimadzu XRD 600 diffractometer with nickel-filtered Cu Kα radiation, at 2θ from 5 to 70º, in continuous scan mode with a step width of 0.02° and a scan speed of 2º min^{-1}. Fourier transform infrared (FTIR) spectra were recorded from 4000 to 500 cm^{-1}, at a resolution of 4 cm^{-1}, using a Bruker Vertex 70 spectrophotometer.

The morphologies of the samples were observed with a JEOL JSM-6701F field emission gun scanning electron microscope (FEG-SEM). The materials were also characterized by transmission electron microscopy (TEM),

using an FEI Tecnai G2 F20 microscope operated at 200 kV. The TEM samples were prepared by wetting copper grids coated with formvar/carbon or ultrathin holey carbon film with drops of alcoholic suspensions, followed by drying in a desiccator. Diffuse reflectance spectrometry (DRS) spectra were recorded with a UV–Vis spectrophotometer (UV-2700, Shimadzu) in the range from 200 to 800 nm. Magnesium oxide (MgO) powder was used as a reflectance standard.

The zeta potential was measured at room temperature using a Zetasizer Nano-ZS analyzer (Malvern Instruments, UK), with the pH adjusted by dropwise addition of dilute HCl or NaOH solutions.

The specific surface area (SSA) values were calculated according to the Brunauer-Emmett-Teller (BET) method, using N_2 adsorption data obtained at -196 °C using a Micromeritics ASAP-2020 system. Surface chemical analyses were performed with a K-Alpha XPS instrument (Thermo Fisher Scientific, UK), using Al Kα X-rays, $>10^{-8}$ mbar of vacuum, and charge compensation during the measurements. A resolution of 1 eV, with 5 scans, was used for survey spectra, while high-resolution spectra were recorded at a resolution of 0.1 eV, with 50 scans. The binding energy was referenced to the C 1s peak at 284.7 eV. Data analysis was performed using CasaXPS software. The fluorescence lifetime was measured using a FluoTime 300 time-correlated single photon counting (TCSPC) instrument (PicoQuant, Germany) equipped with a picosecond-pulsed laser diode (LDH-P-C-405, 409 nm).

The lifetime was measured at an emission wavelength of 535 nm. Thermogravimetric analyses (TGA) were performed on a Shimadzu TGA-50 equipment using oxidative atmosphere conditions (air flow rate of 60 mL min^{-1}), temperature range from 30 to 700 °C and heating rate of 10 °C min^{-1}.

4.3.3 Evaluation of photocatalytic activity

The photocatalytic activities of the as-synthesized samples were evaluated using the oxidation of two different contaminants, namely rhodamine

B (RhB) and amiloride (AML), under visible irradiation. The chemical structures of the molecules are shown in FIGURE 4.3. In a typical procedure, 10 mg of photocatalyst was placed in contact with 20 mL of an aqueous solution of RhB or AML (both at 10 mg L^{-1}). All the experiments were performed at 18 °C in a photoreactor equipped with six fluorescent lamps (Osram, 15 W, maximum intensity at 440 nm), under magnetic stirring. The representative image of the photoreactor is showed in FIGURE 4.4. The photooxidation of RhB and AML was monitored at regular intervals at their maximum absorbances of 554 and 286 nm, respectively, using a Shimadzu UV-1601 PC spectrophotometer. Before starting the photocatalytic experiments, the suspensions were kept in the dark overnight in order to reach adsorption/desorption equilibrium between the contaminant and the photocatalyst surface. The adsorption capacity of both organic pollutants for all of the samples was negligible (< 5%) after 12 h. The mechanism of oxidation of RhB dye promoted by the heterostructured 3CN:1Nb sample was investigated by adding the reactive species scavengers sodium oxalate (SO), tert-butanol (t-BuOH), and potassium bromate ($KBrO_3$) to the dye solution. These scavengers were chosen due to their capacities for trapping holes (h^+), hydroxyl radicals ($^{\bullet}OH$), and superoxide radicals ($O_2^{\bullet-}$), respectively [157–159].

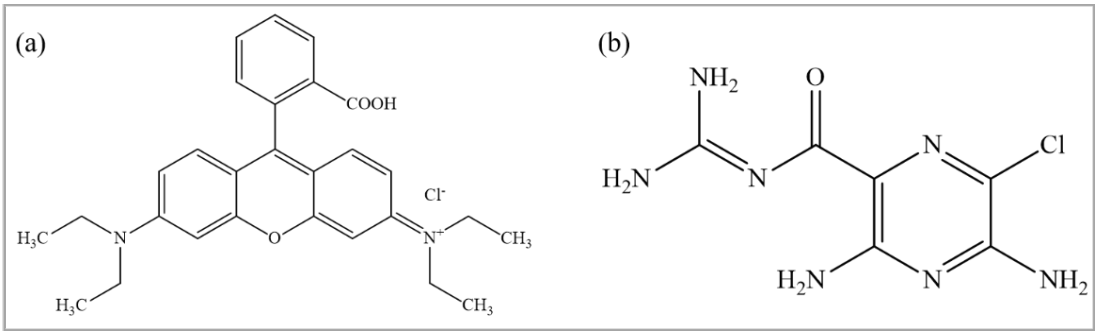

FIGURE 4.3 – Chemical structures of the (a) rhodamine B and (b) amiloride molecules.

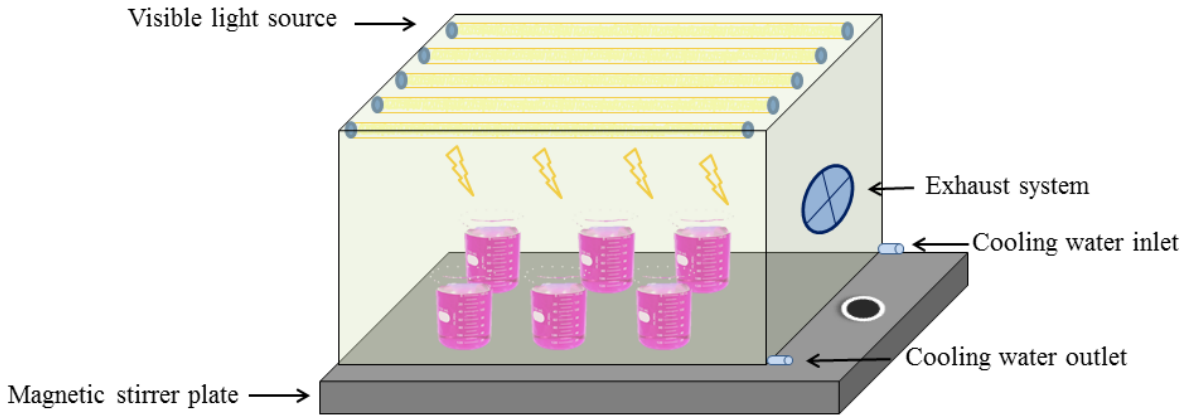

FIGURE 4.4 – Representative image of the photo-reactor used in photocatalytic experiments.

4.4 Results and Discussion

4.4.1 Characterization of the structural, electronic, and morphological properties of the materials

The XRD patterns of the as-synthesized g-C_3N_4, Nb_2O_5, and g-C_3N_4/Nb_2O_5 heterostructures are shown in FIGURE 4.5. The pure g-C_3N_4 XRD pattern exhibited two main diffraction peaks at 27.3° (002) and 13.4° (100) assigned, respectively, to interplanar stacking of aromatic systems and interlayer structural packing of the tetragonal g-C_3N_4 phase (JCPDS 87-1526) [133]. The XRD pattern of pure Nb_2O_5 showed several large diffraction peaks that could be indexed as the orthorhombic Nb_2O_5 phase (JCPDS 28-0317) [13]. The XRD patterns of the g-C_3N_4/Nb_2O_5 heterostructures presented diffraction peaks corresponding to both g-C_3N_4 and Nb_2O_5 phases, indicating that the synthesis method employed did not change the crystalline structure of the catalysts. In addition, it was observed that an increase in the CN:Nb weight ratio caused a gradual decrease in the intensity of the characteristic g-C_3N_4 peaks, indicative of the incorporation of this phase in the heterostructured samples.

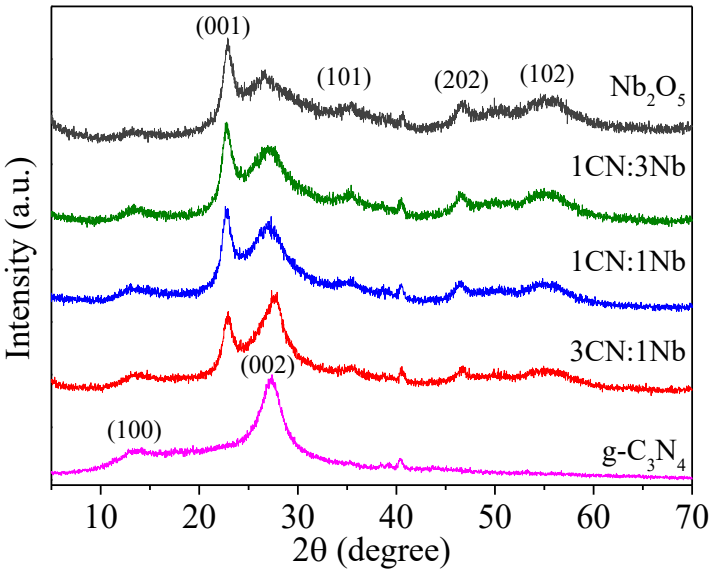

FIGURE 4.5 - XRD patterns of g-C_3N_4, Nb_2O_5, and the g-C_3N_4/Nb_2O_5 heterostructures.

In FIGURE 4.6 shows the FTIR spectra for all the as-synthesized samples. The spectrum of pure g-C_3N_4 presented all the bands described in the literature [134,160], with intense bands at 812 cm^{-1}, 889 cm^{-1}, and in the range 1139-1689 cm^{-1} are assigned to out-of-plane bending vibration of heptazine rings, deformation mode of N-H bonds, and stretching modes of C-N heterocycles, respectively. A broad band at 3220 cm^{-1} corresponded to stretching vibrations of amino groups present at the end of the g-C_3N_4 structure. The spectrum of pure Nb_2O_5 exhibited a broad vibration band centered at about 3384 cm^{-1} attributed to the –OH stretching vibration of adsorbed water molecules on the surface of the oxide, while a broad band at 3231 cm^{-1} was due to the vibrational modes of the hydroxyl groups of Nb-OH [48,102]. The band at 1716 cm^{-1} and 1402 cm^{-1} are attributed to C=O and $C(=O)_2$ derived from the Nb precursor [72]. A shoulder peak at 1101 cm^{-1} and an intense peak at 900 cm^{-1} were assigned to the stretching vibrations of Nb–O–C and Nb=O, respectively [43,102]. It can be seen that the FTIR spectra of the heterostructured samples exhibited characteristic peaks of both phases (g-C_3N_4 and Nb_2O_5), with few or negligible shifts. This could be explained by a relatively small quantity of interfaces available for interaction,

compared to the bulk materials. An increase in the amount of Nb_2O_5 was accompanied by increases of the characteristic bands of this material.

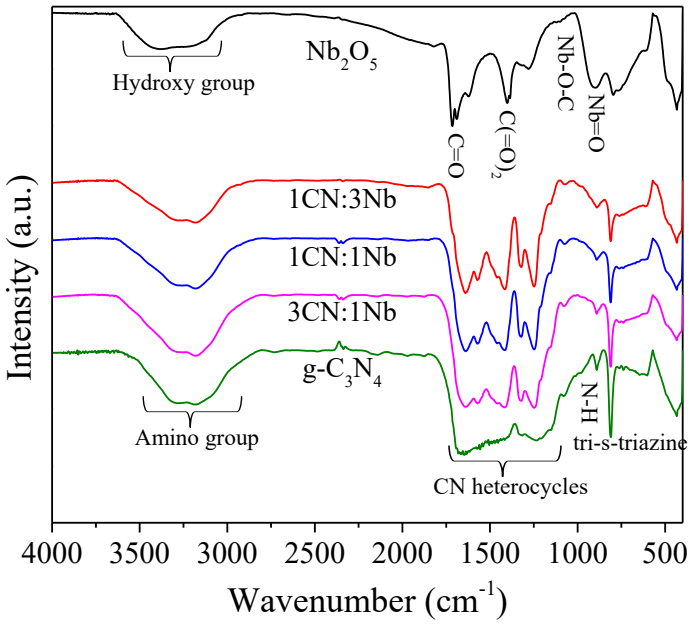

FIGURE 4.6 – FTIR spectra of g-C_3N_4, Nb_2O_5, and the g-C_3N_4/Nb_2O_5 heterostructures.

XPS measurements were performed to confirm the surface composition and the chemical environment of Nb_2O_5, g-C_3N_4, and the 3CN:1Nb heterostructure. The results (survey and high-resolution spectra) are shown in FIGURE 4.7. The survey XPS spectrum (FIGURE 4.7a) of the 3CN:1Nb heterostructure exhibited strong C 1s and N 1s peaks related to the g-C_3N_4 phase, together with Nb 3d and O 1s peaks related to the Nb_2O_5 phase, without any contamination. The C 1s high-resolution spectra of g-C_3N_4 and the 3CN:1Nb heterostructure (FIGURE 4.7b) showed two peaks centered at 284.7 and 288.1 eV. The peak at 284.7 eV corresponded to sp^2 C-C bonds of the carbon standard used to calibrate the binding energies. The peak located at 288.1 eV corresponded to N-C=N coordination present in the triazine rings of g-C_3N_4. As expected, the intensity of this peak was lower in the XPS spectrum for 3CN:1Nb, compared to the spectrum of pure g-C_3N_4. Deconvolution analysis of the N 1s spectra of g-

C_3N_4 and the 3CN:1Nb heterostructure (FIGURE 4.8) identified three peaks centered at 398.6, 399.7, and 400.8 eV, indicating the presence of N species with different chemical environments. These peaks could be assigned to N sp^2-bonded to C present in the triazine ring (C-N=C), tertiary nitrogen groups (N-$(C)_3$), and amino groups present at the end of the network (C-NH_3), respectively [154]. The Nb 3d high-resolution spectrum of pure Nb_2O_5 (FIGURE 4.7c) exhibited two peaks at around 206.8 (Nb $3d_{5/2}$) and 209.6 eV (Nb $3d_{3/2}$). For the 3CN:1Nb heterostructure, the Nb $3d_{5/2}$ and Nb $3d_{3/2}$ peaks shifted to higher energies (FIGURE 4.7c), compared to those of pure Nb_2O_5, evidencing the coordination between the atoms present on the Nb_2O_5 and g-C_3N_4 surfaces that resulted in the formation of effective heterojunctions between them. Deconvolution of the O 1s high-resolution spectrum of the 3CN:1Nb heterostructure (FIGURE 4.8) resulted in two peaks centered at 530 and 531.5 eV, which were attributed to the Nb-O bond and oxygen in hydroxyl or oxalate groups derived from the precursor of niobium, respectively, in agreement with the FTIR observations [106]. In addition, the small peak of O 1s in g-C_3N_4 is assigned to adsorbed oxygen species.

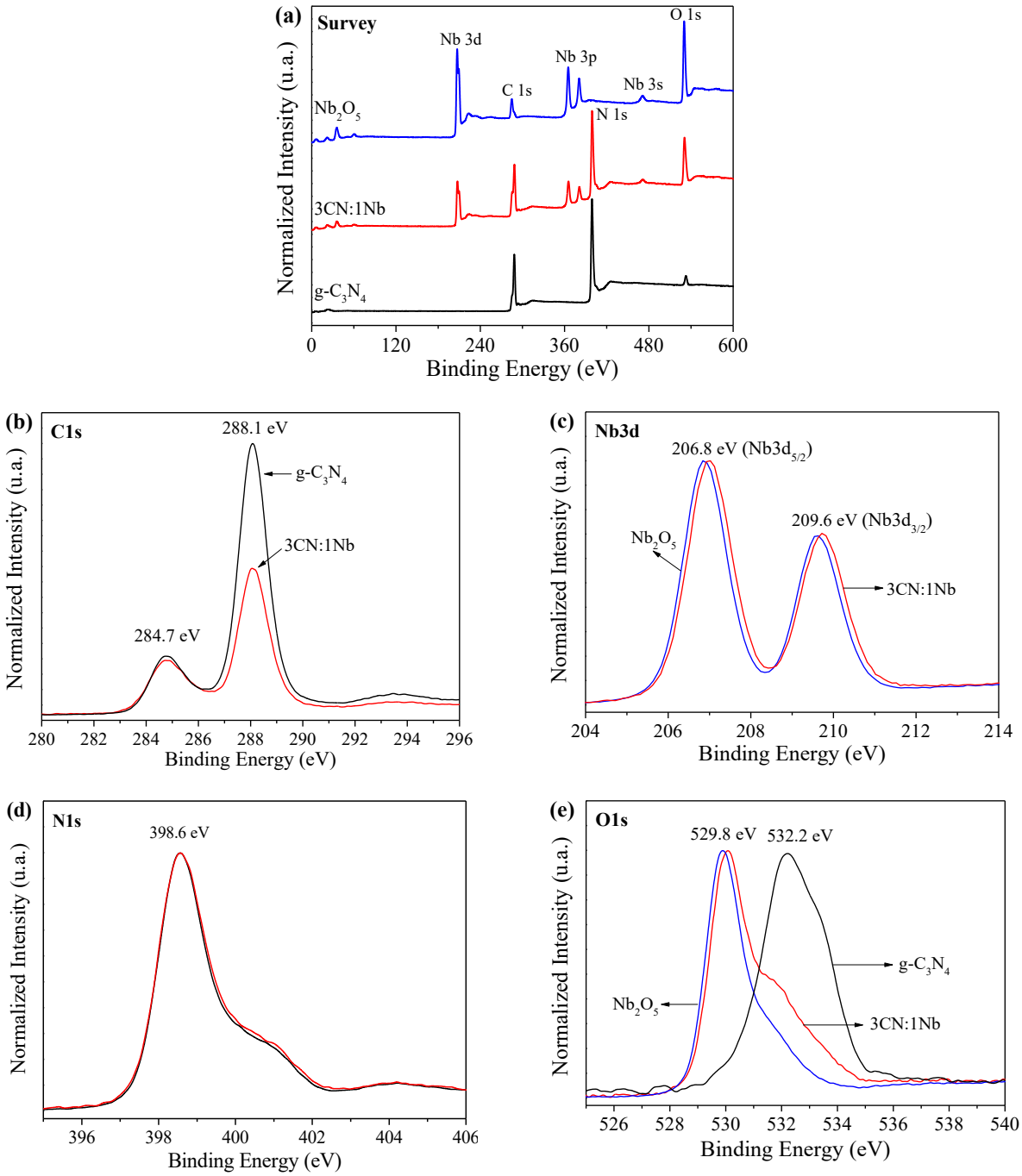

FIGURE 4.7 - XPS spectra of the as-synthesized g-C_3N_4, Nb_2O_5, and 3CN:1Nb heterostructure: (a) survey spectra, (b) high-resolution C 1s spectra, (c) high-resolution Nb 3d spectra, (d) high-resolution N 1s spectra, and (e) high-resolution O 1s spectra.

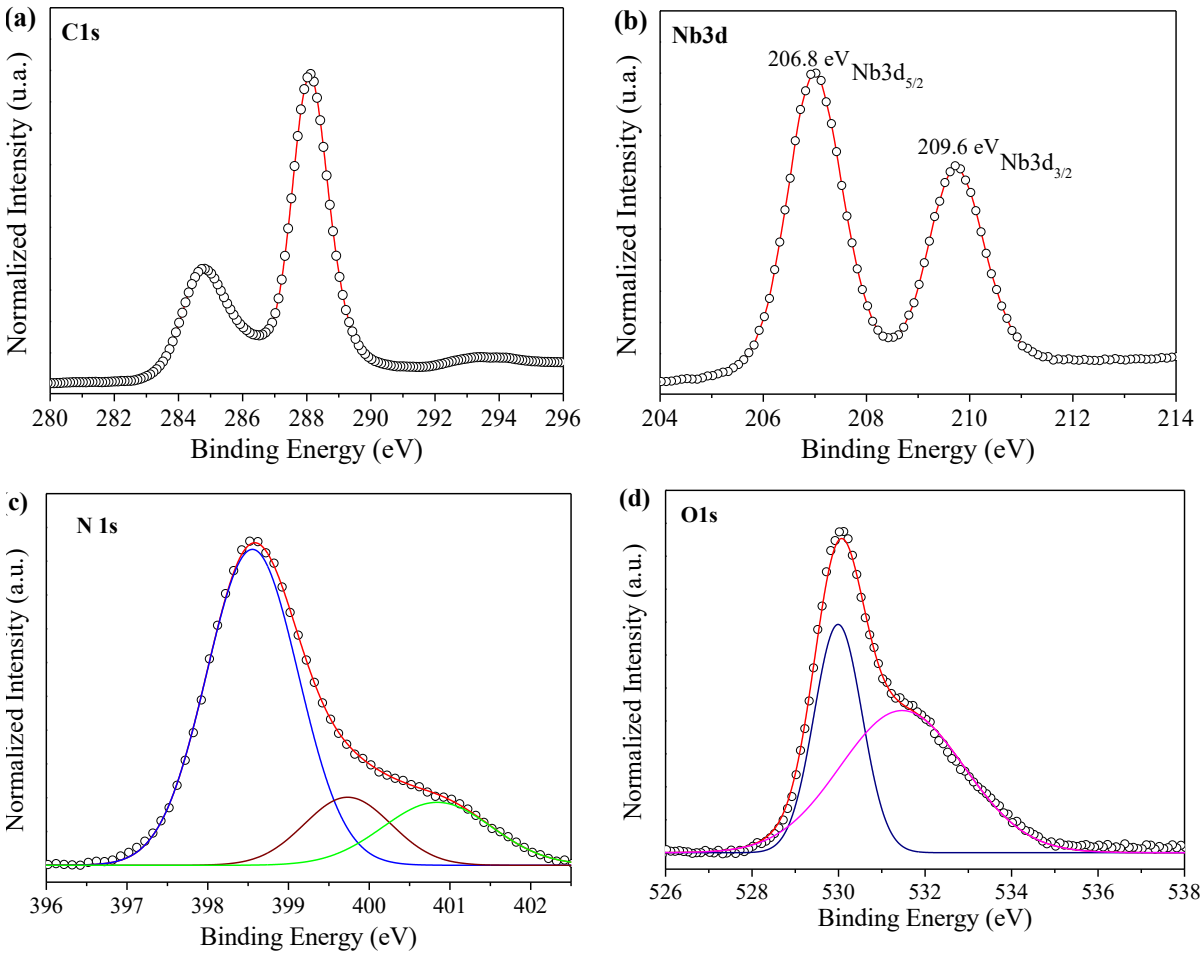

FIGURE 4.8 - (a) XPS survey spectra of the as-prepared g-C_3N_4, Nb_2O_5, and 3CN:1Nb heterostructure. (b) C 1s, (c) Nb 3d, (d) N 1s, and (e) O 1s high-resolution XPS spectra of the 3CN:1Nb heterostructure.

SEM (see in FIGURE 4.9) and TEM (FIGURE 4.10) images were used to analyze the morphologies of the as-synthesized samples. The pure g-C_3N_4 and Nb_2O_5 samples exhibited laminar and spherical agglomerate morphologies, respectively, as reported elsewhere [13,133]. Additionally, it can be seen in FIGURES 4.10c-e that the 3CN:1Nb heterostructure consisted of agglomerates of Nb_2O_5 nanoparticles quasi-homogeneously distributed on the laminar surface of g-C_3N_4.

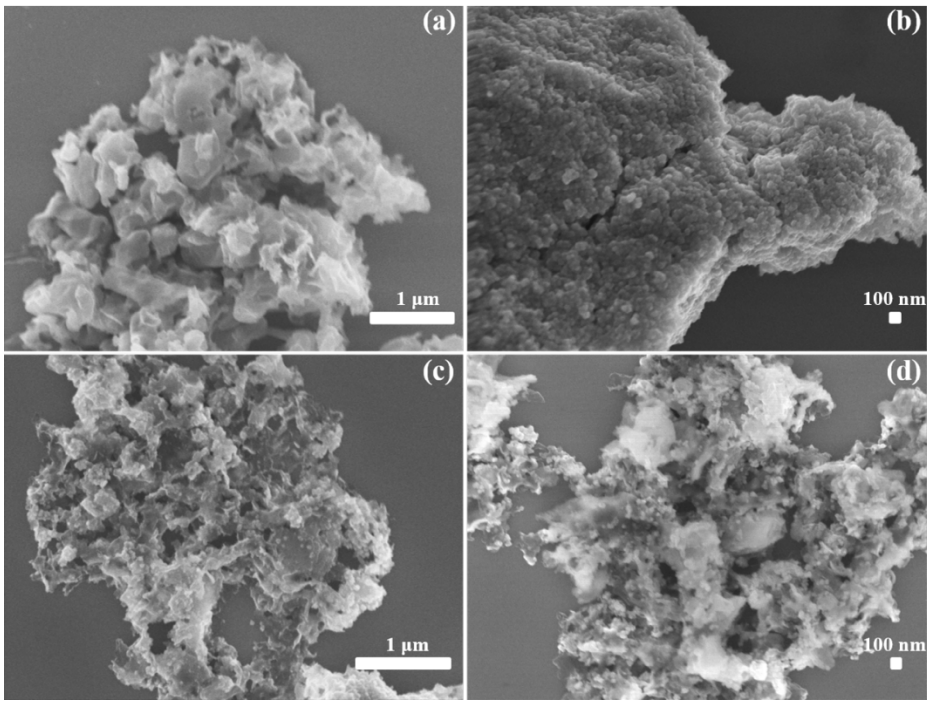

FIGURE 4.9 - Representative SEM images of (a) g-C_3N_4, (b) Nb_2O_5, (c) 3CN:1Nb, and (d) 1CN:3Nb.

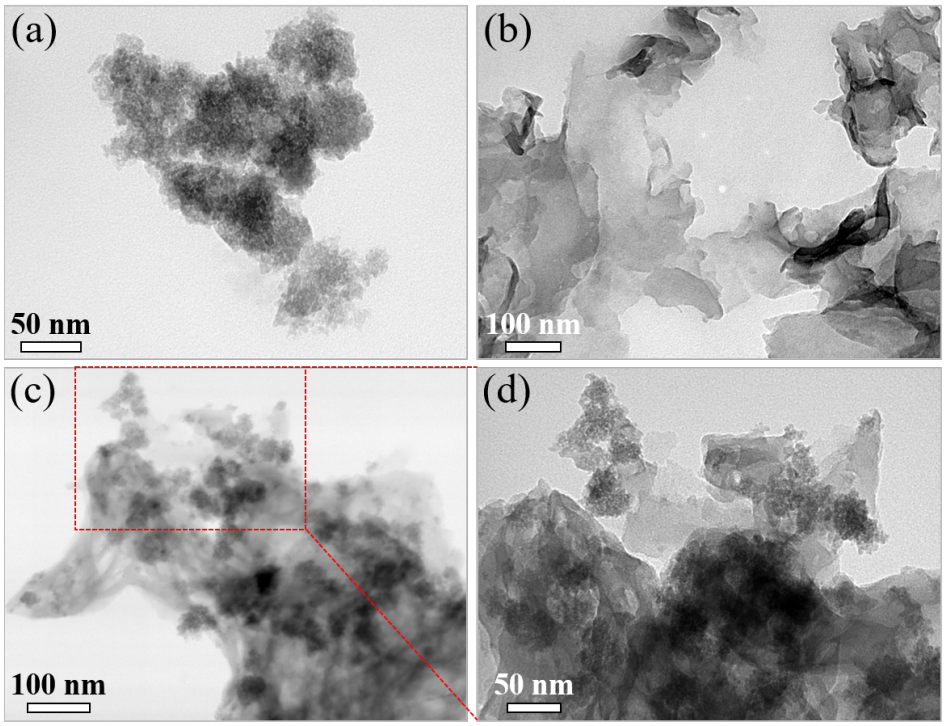

FIGURE 4.10 – TEM images of (a) Nb_2O_5 nanoparticles, (b) g-C_3N_4, and (c-d) 3CN:1Nb heterostructures.

As shown in FIGURE 4.10f, HRTEM image of the 3CN:1Nb sample showed an average inter-fringe distance of 0.39 nm, which could be attributed to the (001) plane of the orthorhombic Nb_2O_5 structure [13,101]. This finding confirmed the presence of Nb_2O_5 on the g-C_3N_4 surface, in agreement with the XRD observations (see in FIGURE 4.5). Furthermore, elemental mapping analysis (FIGURE 4.11) of the heterostructured 3CN:1Nb sample identified the presence of the elements C, N, Nb, and O sharing the same space, confirming that the agglomerates consisted of Nb_2O_5 nanoparticles in intimate contact with the g-C_3N_4 sheets. A notable feature was the satisfactory distribution of Nb_2O_5 over the g-C_3N_4 sheets, showing that the sonolysis procedure was highly effective in maximizing homogeneity, with the Nb_2O_5 particles being dispersed and showing similar sizes to those observed for the pristine material (FIGURE 4.10a). The same features were observed in the SEM images of the 1CN:3Nb heterostructure (see in FIGURE 4.9), which revealed Nb_2O_5 nanoparticles present on the g-C_3N_4 surface, showing that heterojunctions were formed using different CN:Nb weight ratios.

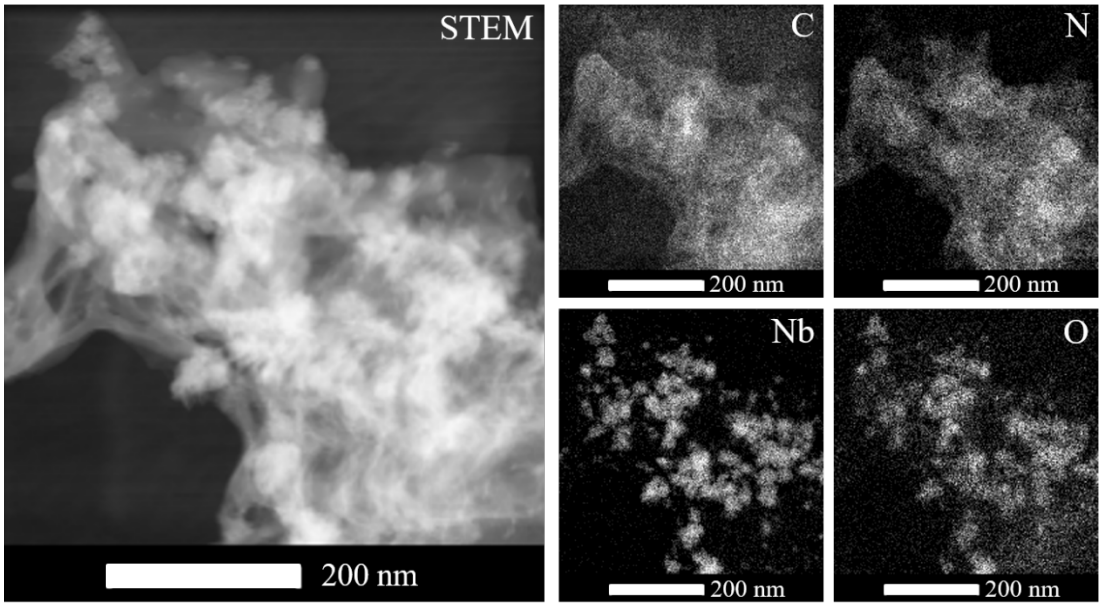

FIGURE 4.11 - STEM image and elemental distribution maps for C, N, Nb, and O of the 3CN:1Nb heterostructure.

Diffuse reflectance spectroscopy measurements were carried out to evaluate the optical properties of the as-synthesized samples. The Tauc equation [161] was used to calculate the band gap energy values of g-C_3N_4, Nb_2O_5, and the g-C_3N_4/Nb_2O_5 heterostructures (FIGURE 4.12). The band gap values of the pure g-C_3N_4 and Nb_2O_5 samples were approximately 2.8 and 3.2 eV, respectively, which were consistent with those described for these phases in the literature [13,17]. All the CN:Nb heterostructures (FIGURE 4.12) showed band gap values similar to that obtained for g-C_3N_4, indicating that the optical properties of g-C_3N_4 were predominant in these heterostructures. Consequently, the CN:Nb heterostructures could be activated under visible irradiation, which is highly desirable for photocatalytic purposes.

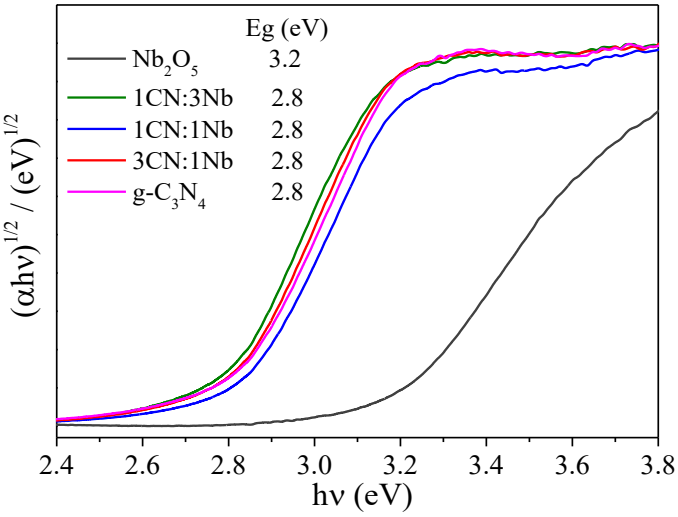

FIGURE 4.12 - Tauc plot obtained from UV-Vis diffuse reflectance spectra data for Nb_2O_5, g-C_3N_4, and the g-C_3N_4/Nb_2O_5 heterostructures.

The specific surface areas (SSA) of the g-C_3N_4, Nb_2O_5, and g-C_3N_4/Nb_2O_5 heterostructures samples were obtained by applying the BET model to the nitrogen adsorption data (TABLE 4.1). A higher specific surface area of g-C_3N_4 after the sonochemical treatment, compared to bulk g-C_3N_4, could be attributed to mechanical exfoliation of the sheets induced by the ultrasonic treatment [162]. On the other hand, the pure Nb_2O_5 sample did not show any

significant change in specific surface area following the sonication process. The specific surface areas of the 3CN:1Nb, 1CN:1Nb, and 1CN:3Nb heterostructures were approximately 113.4, 118.3, and 156.2 $m^2 g^{-1}$, these values are very close to the expected ones for the linear combination of the SSAs of the g-C_3N_4 and Nb_2O_5 components.

TABLE 4.1 - Specific surface areas (SSAs) of as-synthesized samples.

Sample	SSA ($m^2 g^{-1}$)		
	Experimental	*Calculated	**Before
Nb_2O_5	193.4	-	200.7
1CN:3Nb	133.9	155.2	-
1CN:1Nb	118.3	129.7	-
3CN:1Nb	113.4	104.2	-
g-C_3N_4	65.9	-	54.9

*Corresponds to the linear combination of the SSAs of the pristine materials according to the relative amount of each material.
**Before and after sonochemical treatment.

4.4.2 Evaluation of photocatalytic properties

The photocatalytic performances of the as-synthesized samples were evaluated using the oxidation of rhodamine B (RhB) dye under visible irradiation (λ >420 nm). As shown in FIGURE 4.13a, a blank test performed in the absence of the photocatalysts indicated that the contribution of direct photolysis was not significant, and that adsorption was also negligible. Hence, a decrease in the RhB concentration could be attributed exclusively to its oxidation due to the effect of photocatalysis. The pure Nb_2O_5 sample exhibited low activity in RhB photooxidation, with an efficiency of 17% after 90 min under visible irradiation. This result was probably due to a photosensitization process [13], because this material exhibited an optical absorption edge at wavelengths lower than 387.5 nm (~3.2 eV), so it could only be directly activated under ultraviolet irradiation. The pure g-C_3N_4 sample showed RhB dye photooxidation efficiency of 54%, while the 1CN:3Nb, 1CN:1Nb, and 3CN:1Nb heterostructures exhibited efficiencies of approximately 67, 79, and 81%, respectively.

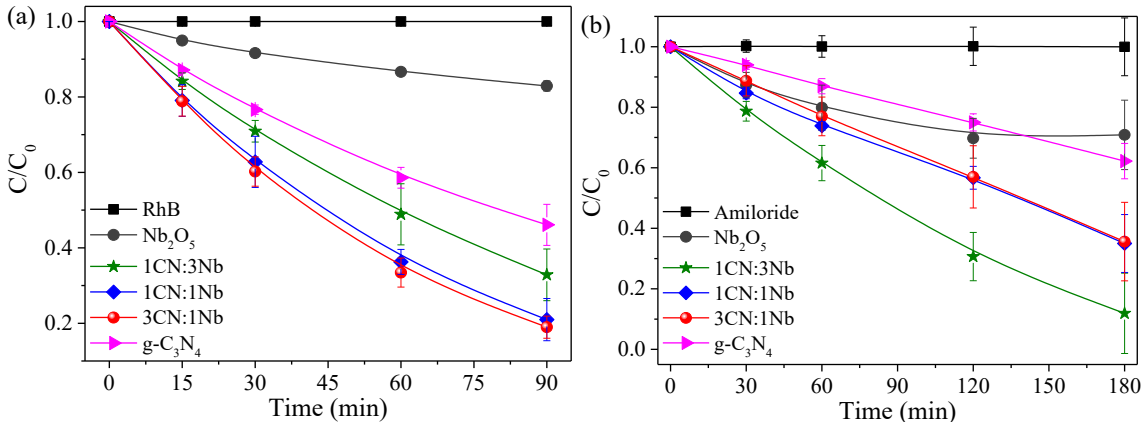

FIGURE 4.13 - Curves of (a) RhB dye and (b) drug AML photooxidation catalyzed by the as-synthesized samples under visible irradiation.

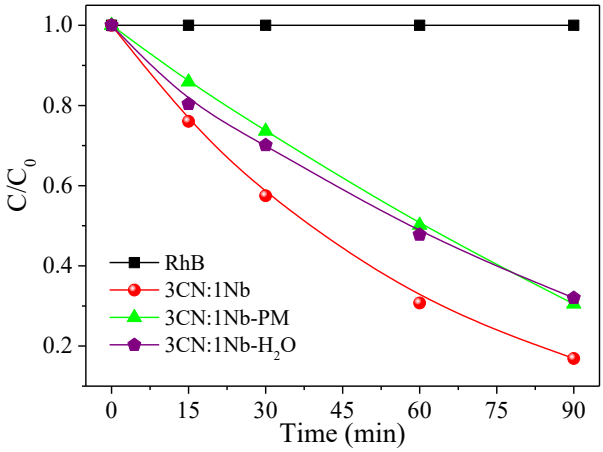

FIGURE 4.14 - Photo degradation curves of RhB under visible light using the g-C_3N_4/Nb_2O_5 samples obtained using different synthesis conditions.

Additionally, the 3CN:1Nb heterostructure showed higher photoactivity than the 3CN:1Nb-PM and 3CN:1Nb-H_2O samples, as shown in FIGURE 4.14. Quantitative determination of the photocatalytic efficiencies of the different samples in RhB oxidation was achieved by calculating the kinetic rate constants of the reactions catalyzed by the materials. It was assumed that the reactions followed apparent first-order kinetics, described by the equation: $-\ln(C/C_0) = k_{app}t$, where C_0 and C are the initial RhB dye concentration and the concentration at time "t", respectively, and k_{app} is the apparent rate constant

(min^{-1}). TABLE 4.2 shows the k_{app} values for all the as-synthesized samples. The value of k_{app} obtained for the 3CN:1Nb heterostructure was approximately 2.2 and 9.4 times higher than those obtained for pure g-C_3N_4 and Nb_2O_5, respectively. Additionally, the 3CN:1Nb heterostructure showed 1.5 and 1.6 times higher than those obtained for 3CN:1Nb-PM and 3CN:1Nb-H_2O samples (TABLE 4.2), respectively, indicating the suitability of a sonochemical method based on surface charge-induced heteroaggregation for obtaining effective heterojunctions between two semiconductors. It was found that an increase in the CN:Nb weight ratio resulted in a significant increase in the photocatalytic activity of the heterostructure, indicating that the superior photocatalytic performance of the composite materials was probably due to interfacial charge transfer between the g-C_3N_4 and Nb_2O_5 semiconductors, which increased the lifetime of photogenerated electron/hole pairs.

TABLE 4.2 - Apparent rate constant (k_{app}) for the RhB dye and drug AML photocatalytic oxidation under different photocatalysts driven by visible radiation.

Photocatalysts	Rhodamine B		Amiloride	
	k_{app} x 10^3 (min^{-1})	R^2	k_{app} x 10^3 (min^{-1})	R^2
Nb_2O_5	2.6	0.96657	1.8	0,90727
g-C_3N_4	9.4	0.99919	3.1	0,99383
1CN:3Nb	11.4	0.99878	13.7	0,94184
1CN:1Nb	18.9	0.99828	6.6	0,96503
3CN:1Nb	20.2	0.99874	6.3	0,98337
3CN:1Nb-PM	13.2	0.98651	-	-
3CN:1Nb-H_2O	12.5	0.99732	-	-

Amiloride (AML) was used here to demonstrate the non-selectivity of the as-synthesized samples to catalyze the oxidation of different kinds of organic pollutants. FIGURE 4.13b shows the curves for AML photooxidation catalyzed by the as-synthesized photocatalysts under visible irradiation. As in the RhB photooxidation, no oxidation by direct photolysis was observed using an

AML solution without any catalysts, under visible irradiation for 180 min. All the as-synthesized samples were photoactive for AML oxidation, since the kinetic curves decreased faster than the direct photolysis curve. The apparent kinetic rate constants (k_{app}) were obtained by plotting the apparent first-order kinetics curves for AML photooxidation (TABLE 4.2). All the composite materials showed higher photoactivity, compared to the pure phases. The FIGURE 4.15 shows the UV-Vis spectra of amiloride during the photocatalytic experiments in the presence of the heterostructure.

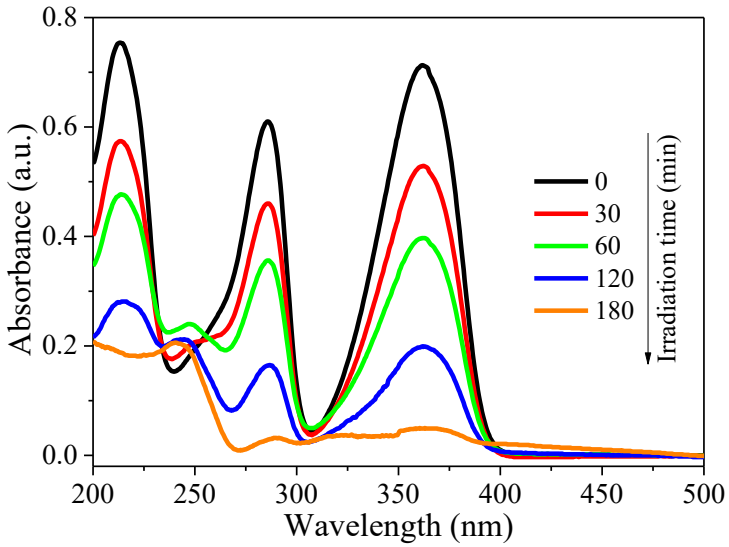

FIGURE 4.15 - Time dependent UV-vis spectra of amiloride solution (10 mg L^{-1}) in presence of 1CN:3Nb heterostructure under visible irradiation

In contrast to the behavior observed with RhB, the 1CN:3Nb heterostructure was the most active, with an apparent kinetic rate constants approximately 6.2 and 4.5 times higher than obtained for the pure Nb_2O_5 and g-C_3N_4 samples, respectively. These results were probably related to the differences in surface acidity, considering that Nb_2O_5 is highly acid. The AML molecule possesses basic groups (as shown in FIGURE 4.3) that were probably able to interact with the acid surface, hence improving the oxidation process. On the other hand, RhB is a zwitterionic molecule [132], so the net charge in solution was expected to be zero. Therefore, the dye was less influenced by the surface acidity,

compared to AML. These findings demonstrate the versatility of this material, since it could be used in certain selective oxidation procedures, while adjustment of its composition could be employed to enhance its performance in the oxidation of different substrates. Additionally, photocatalytic experiments under UV irradiation were performed and a similar behavior was observed for photooxidation of the RhB dye and drug AML catalyzed by the as-synthesized samples, in which the heterostructured g-C_3N_4/Nb_2O_5 samples exhibited higher photocatalytic activity than the isolated phases (FIGURE 4.16 and TABLE 4.3). These findings confirmed the formation of effective heterojunctions between g-C_3N_4 and Nb_2O_5, resulting in superior photocatalytic performance of the heterostructured samples.

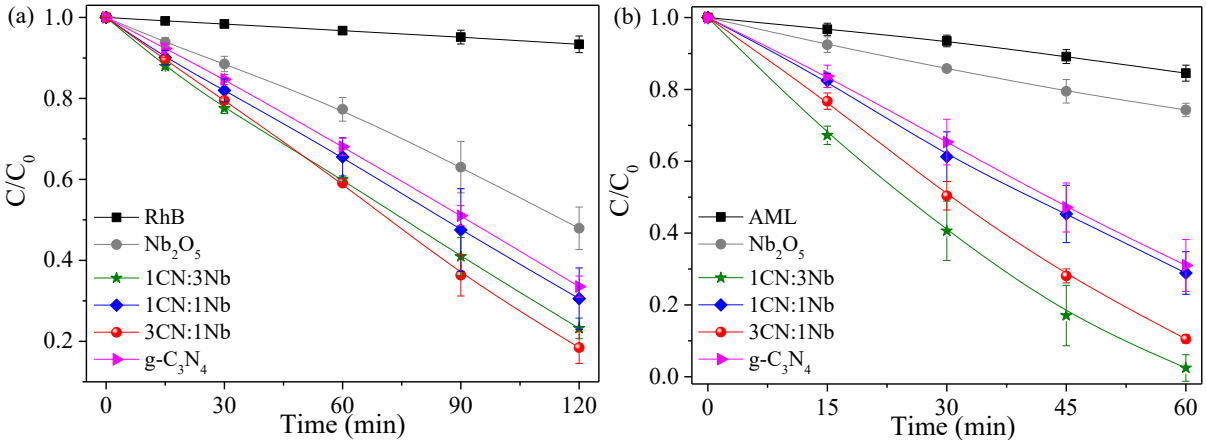

FIGURE 4.16 - Curves of (a) RhB dye and (b) drug AML photooxidation catalyzed by the as-synthesized samples under UV irradiation.

TABLE 4.3 - Kinetics constant values obtained from organic pollutants photodegradation catalyzed by the as-synthesized samples under UV irradiation.

Sample	k_{RhB} x 10^3 (min^{-1})	k_{AML} x 10^3 (min^{-1})
Blank	0.57	2.78
Nb_2O_5	5.97	4.97
1CN:3Nb	11.73	58.59
1CN:1Nb	9.62	20.55
3CN:1Nb	13.72	36.71
g-C_3N_4	8.90	19.44

In order to understand the dynamics of the electron/hole pair recombinations of the as-synthesized materials, their lifetimes were calculated for the pure g-C_3N_4 and the 3CN:1Nb heterostructure samples using time-resolved photoluminescence, with excitation at 409 nm and monitoring of the photoluminescence decay spectra at 535 nm. The measurement was not performed for the pure Nb_2O_5, because this material has a band gap of ~3.2 eV (FIGURE 4.12) and is not activated by laser excitation at 409 nm. FIGURE 4.17 shows a comparison of the time-resolved photoluminescence decay spectra of g-C_3N_4 and the 3CN:1Nb heterostructure. For both samples, the fluorescence decay was fitted using a bi-exponential decay function (FIGURE 4.17). The values of the lifetime constants (τ) are shown in TABLE 4.4. Higher lifetime constants (τ_1 and τ_2) were obtained for the 3CN:1Nb heterostructure, compared to pure g-C_3N_4. These results confirm the formation of the type-II heterostructure, since this kind of heterostructure provides a spatial separation of the electron/hole pair driven by the difference between the reduction potentials of the g-C_3N_4 and Nb_2O_5 semiconductors, resulting in an increase in its lifetime [142,143]. As illustrated in SCHEME 4.2, the photogenerated electrons in the conduction band of g-C_3N_4 (-1.23 eV), instead of returning quickly to its valence band, migrate to the conduction band of Nb_2O_5 (-0.80 eV), while the photogenerated holes in the

valence band of Nb_2O_5 (+2.3 eV) migrate to the valence band of g-C_3N_4 (+1.40 eV) [147,163,164]. The increase in the lifetime of the photogenerated charges observed for the 3CN:1Nb heterostructure explains its higher photocatalytic performance in the oxidation of RhB and AML than that of the pristine g-C_3N_4, as shown in FIGURES 4.13 and 4.16a-b. These findings demonstrated the formation of effective heterojunctions between the g-C_3N_4 and Nb_2O_5 phases, which favored the transfer of charge carriers between them and increased the lifetimes of the photogenerated charges.

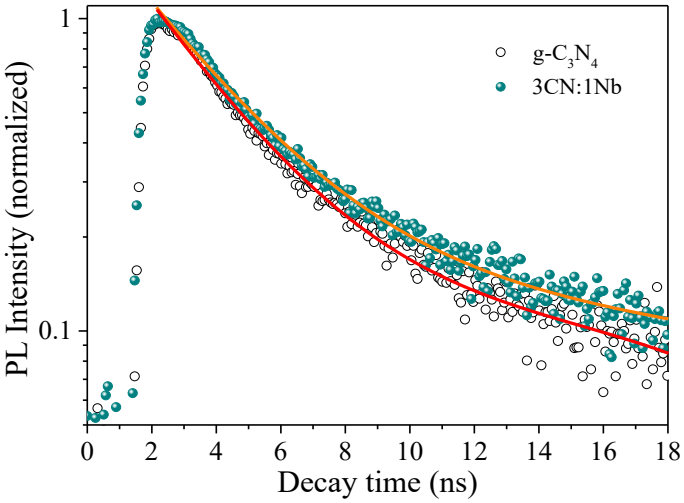

FIGURE 4.17 - Time-resolved fluorescence decay spectra of g-C_3N_4 and the 3CN:1Nb heterostructure excited by laser irradiation at 409 nm and monitored at 535 nm. The solid lines are the results of the kinetic fits.

TABLE 4.4 – Radiative fluorescence lifetimes of the photoexcited charge carriers in g-C_3N_4 and the 3CN:1Nb heterostructure.

Sample	τ_1 [ns]	τ_2 [ns]
g-C_3N_4	2.03	14.38
3CN:1Nb	2.21	14.64

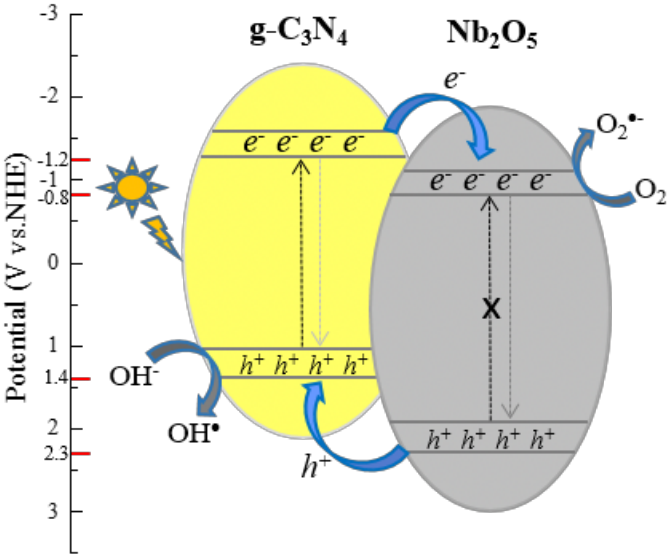

SCHEME 4.2 - Schematic diagram showing the charge transfer between the g-C_3N_4 and Nb_2O_5 phases in the heterostructure under visible irradiation.

4.4.3 Evaluation of photooxidation mechanism and stability

In order to understand the main mechanism of RhB and AML oxidation catalyzed by the g-C_3N_4/Nb_2O_5 heterostructures, evaluation was made of the effect of adding different reactive scavenger species directly to the 3CN:1Nb and 1CN:3Nb materials (FIGURE 4.18). It was found that •OH radicals had no substantial influence on the oxidation profile, since oxidation tests with TBA showed almost the same result as the standard test, with oxidation of RhB occurring at a similar rate. On the other hand, the presence of sodium oxalate (hole scavenger) caused a large decrease in RhB photooxidation, showing that the photogenerated holes in the valence band played an important role in this process. The $O_2^{\bullet-}$ radical made a minor contribution to RhB photooxidation, as can be observed in FIGURE 4.18, with the presence of $KBrO_3$ (electron scavenger) causing only a small decrease. These results indicated that the direct oxidation (i.e., hole attack) of the rhodamine B molecules was the most important mechanism, so the interaction between the substrate and the g-C_3N_4/Nb_2O_5 heterostructure surface was the first step of the oxidation mechanism.

Regarding the mechanism of the AML photooxidation, it was found that the presence of sodium oxalate (hole scavenger) caused only a small decrease

in this process. On the other hand, the presence of $KBrO_3$ (electron scavenger) caused a significant increase in AML photooxidation. This result is most likely due to the increase in the lifetime of the photogenerated holes, leading to a higher $^{\bullet}OH$ formation. In addition, it was observed a large decrease in the presence of TBA ($^{\bullet}OH$ scavenger), showing that the indirect oxidation promoted by hydroxyl radical generation was the main mechanism for drug AML photooxidation process.

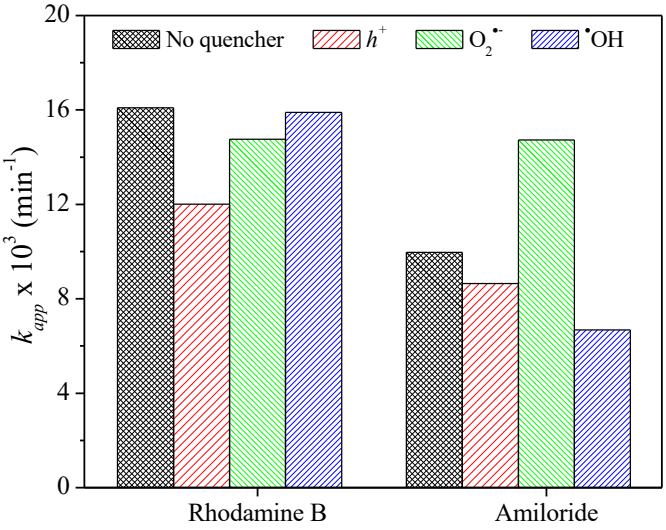

FIGURE 4.18 - Effects of different scavengers on RhB dye and drug AML photooxidation over the 3CN:1Nb and 1CN:3Nb heterostructures, respectively, under visible irradiation.

The stability of a photocatalyst is a crucial parameter in catalytic applications such as the treatment of wastewater. The stability of the 3CN:1Nb and 1CN:3Nb heterostructures, which were chosen due to their higher photoactivities (FIGURES 4.13a-b), was evaluated during the photooxidation of RhB dye and the drug AML under visible irradiation. After each cycle of the photocatalytic reaction, the photocatalyst was recovered by centrifugation and transferred to a fresh pollutant solution to repeat the reaction under identical conditions. The results (FIGURE 4.19) showed that the heterostructures exhibited good stability, since the photocatalytic efficiency decreased by only 23% and 7%

to 3CN:1Nb and 1CN:3Nb, respectively, after four cycles of reuse. This decrease in photooxidation efficiency may be related to two factors: loss of material by leaching during the reuse process or chances of physical-chemical properties such as morphology, surface groups, and structure. As shown in FIGURE 4.20 the SEM, FTIR, and XRD characterizations were performed before and after the photocatalytic experiments and the properties of the materials remained practically unchanged, thus the leaching loss was considered to be the responsible for the loss of material activity.

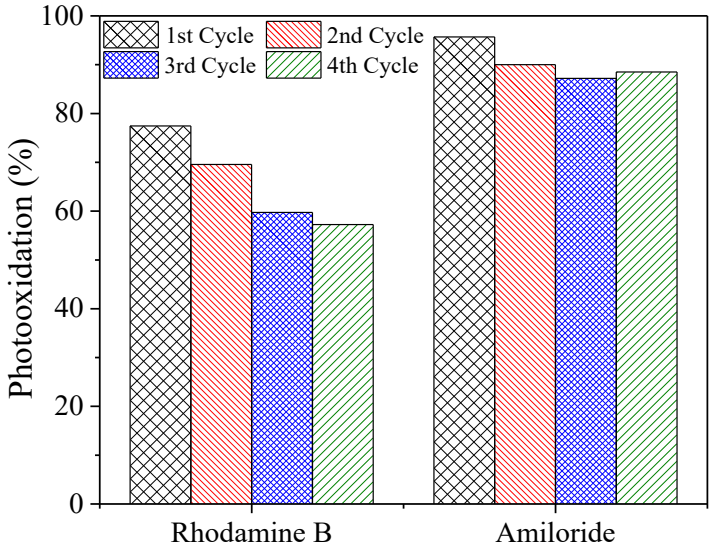

FIGURE 4.19 – Stability of the 3CN:1Nb and 1CN:3Nb heterostructures during consecutive cycles of RhB and AML photooxidation, respectively, under visible irradiation.

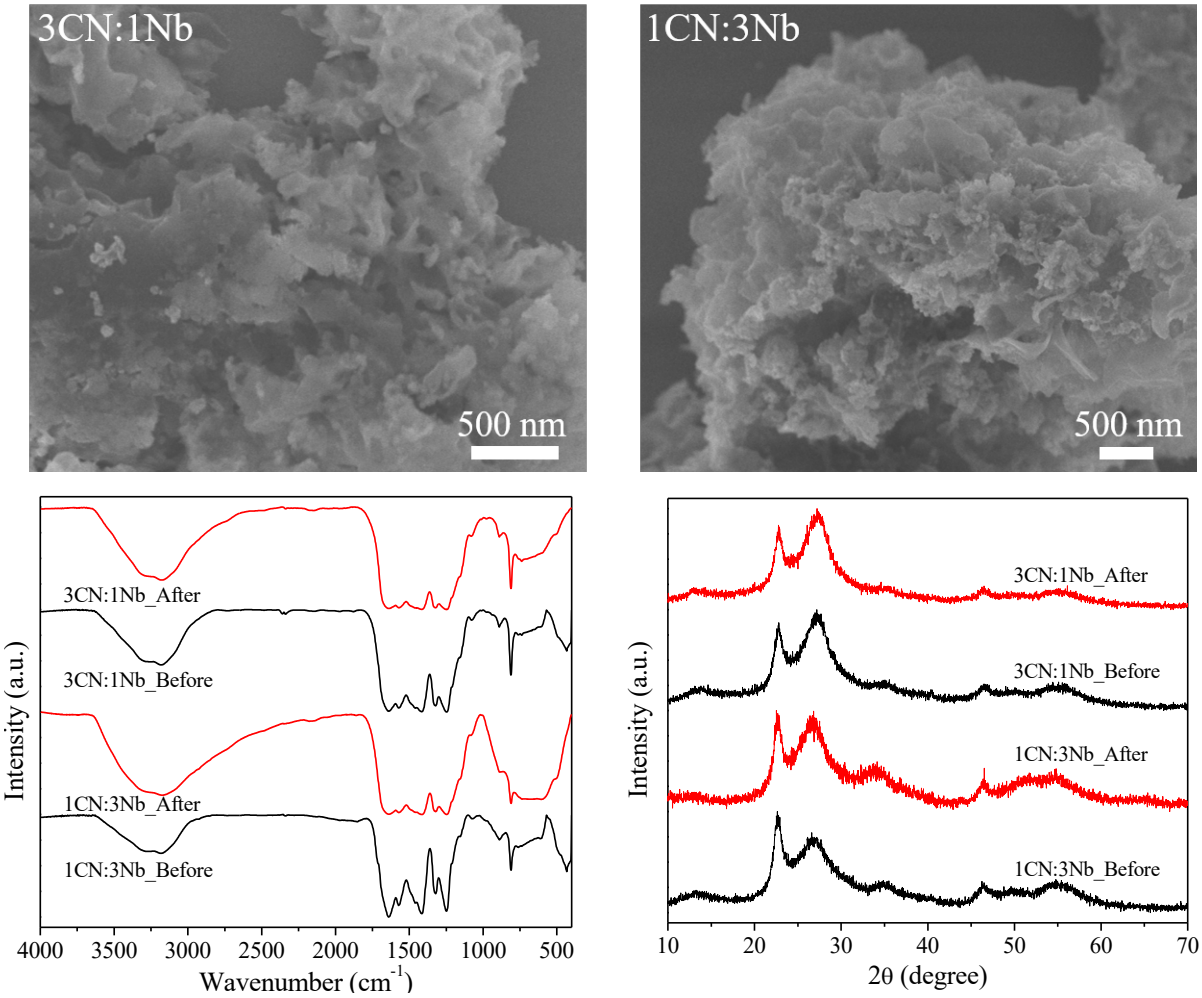

FIGURE 4.20 - Representative SEM images, FTIR spectra, and XDR patterns of 3CN:1Nb and 1CN:3Nb after experiments of photooxidation of RhB and AML, respectively.

4.5 Conclusions

In summary, g-C_3N_4/Nb_2O_5 heterostructures with different CN:Nb weight ratios were successfully obtained using an efficient and versatile method based on surface charge-induced heteroaggregation combined with a sonochemical treatment. The g-C_3N_4/Nb_2O_5 heterostructures exhibited higher photocatalytic activities towards the oxidation of RhB and AML under visible irradiation, compared to the pure g-C_3N_4 and Nb_2O_5 phases. The 3CN:1Nb and 1CN:3Nb heterostructures showed the highest photocatalytic performances in the oxidation of RhB and AML, respectively, because these substrates interacted

differently with the heterostructure surfaces. The direct (i.e., hole attack) and indirect (i.e., $^{\bullet}OH$ attack) mechanisms play the most important role in the oxidation of RhB and AML, respectively, catalyzed by the g-C_3N_4/Nb_2O_5 heterostructures. The enhancement of their photoactivities was attributed to longer lifetimes of the electron/hole pairs, due to the migration of photogenerated charge carriers between g-C_3N_4 and Nb_2O_5. In addition, it was demonstrated that the g-C_3N_4/Nb_2O_5 heterostructures exhibited satisfactory photostability, even after four successive reuse cycles.

5 CHAPTER III: CO_2 photoreduction catalyzed by g-C_3N_4/Nb_2O_5 heterojunctions

The content of this chapter is an adaptation of the article entitled **"Surface protonation of g-C_3N_4 and improving the heterojunction p-CN/Nb_2O_5 toward to increase its photocatalytic performance for CO_2 conversion into CH_4"** by Gelson T.S.T. da Silva, Kele T. G. Carvalho, Osmando F. Lopes, and Caue Ribeiro that is under production.

5.1 Abstract

In this study, we attempted to protonate the surface of C_3N_4, aiming at a process of electrostatic heteroaggregation induced by sonication between the protonated C_3N_4 and Nb_2O_5 obtained by hydrothermal crystallization as a strategy to produce materials capable of promoting the reaction of CO_2 photoreduction. The method proved to be effective because it changes the surface charge of C_3N_4 from a negative to a positive value, which drives spontaneously the interaction with the Nb_2O_5 since this oxide has a negative surface charge. After the heterojunction formation all the materials enlarged the absorption region of the electromagnetic spectrum, C_3N_4 characteristic profile. In addition, all the heterojunctions showed photocatalytic performance for the conversion of CO_2 to CH_4 under UV radiation, compared to pure materials. This is associated to an increase in the recombination time of the photogenerated electron/hole pairs confirmed by luminescence spectroscopy since all samples have an emission intensity lower than the pure C_3N_4, characterizing photogenerated charge migration.

5.2 Experimental Section

5.2.1 Sample preparation

Firstly, bulk g-C_3N_4 was prepared using a typical for thermal polymerization of urea (CH_4N_2O, Synth) in a muffle furnace with an air atmosphere. The urea powder (10g) was put into an alumina crucible with a semi-covered and heated to 550 °C for 2 h at a heating rate of 3 °C min^{-1}, resulting in yellow powder. Then, g-C_3N_4 was exfoliated and protonated via acidification combined with the sonicated method. Briefly, 1 g g-C_3N_4 powder was placed a beaker with 200 mL of HCl aqueous solution (0.5 mol L^{-1}) and maintained under an ultrasound bath for 1 h to exfoliation of the material. After that, further to protonation g-C_3N_4 acid suspension was stirred vigorously for 4 h at room temperature. The final material was washed with deionized water to remove HCl

until the pH of the filtrate water became neutral.[165] Finally, the pCN product was dried at 70 °C for 12 h and then ground into powder. Pure Nb_2O_5 NPs were synthesized by hydrothermal route from a precursor ammonium niobium oxalate ($NH_4[NbO(C_2O_4)_2(H_2O)_2]\cdot nH_2O$ – CBMM, Brazil) and H_2O_2 at 120 °C for 12 h and a white powder was obtained.[13]

The g-C_3N_4/Nb_2O_5 heterostructures were prepared by ultrasonic method. 500 mg of Nb_2O_5 and different amounts of g-C_3N_4 were immersed into 350 mL of water. Then, placed the solution under ultrasonic shaking for 1h in ice-bath. After that, materials were centrifuged dried at 80 °C in air. The heterostructured samples are referred to as xpCN-yNb, where x is the weight ratio of g-C_3N_4, and y is the weight ratio of Nb_2O_5.

5.2.2 Characterization

Zeta potential measurements were obtained by dynamic light-scattering analysis using the Zetasizer Nano ZS (Malvern Instruments). In brief, 2 mg of the sample was dispersed in 20 mL of DI water by sonication at room temperature. The phase compositions of the samples were characterized with a powder X-ray diffractometer (XRD, Shimadzu) using Cu-Kα radiation at a scanning rate of 2° min^{-1} in the 2θ range 10–70°. Thermogravimetric analysis (TGA) was done on a TA Instrument Q500 from room temperature to 700 °C at a constant heating rate of 10 °C min^{-1} under air atmosphere. UV-vis diffuse reflectance spectra were recorded on a Varian model Cary 5G spectrometer from 200 to 800 nm to determine the band gap of the materials. The measurements were performed in total reflection mode with an integration cell containing MgO as a reference. A field emission gun scanning electron microscope (FEG-SEM Jeol JSM 6701F) working at 3 kV was used to verify the materials morphology. A Micrometrics ASAP 2000 instrument was used to measure the Brunauer–Emmett–Teller (BET) surface area at liquid nitrogen temperature after a pretreatment at 100 °C. Photoluminescence (PL) measurements were carried out

on a LS 50B fluorescence spectrometer (PerkinElmer). The fluorescence emission spectra were obtained with an excitation wavelength of 390 nm.

5.2.3 Photocatalytic experiments

The photocatalytic activity of the as-synthesized samples was evaluated for the photo-reduction of CO_2 under UV irradiation (the irradiation spectra are shown in FIGURE A1) in a stainless-steel reactor (FIGURE 5.1). Before irradiation, the reactor was purged with ultrapure gaseous CO_2 and water vapor for 30 min to achieve the adsorption-desorption equilibrium and to remove the oxygen inside of the reactor. After that, the reactor was sealed, and the reaction was started turning on the UV light source.

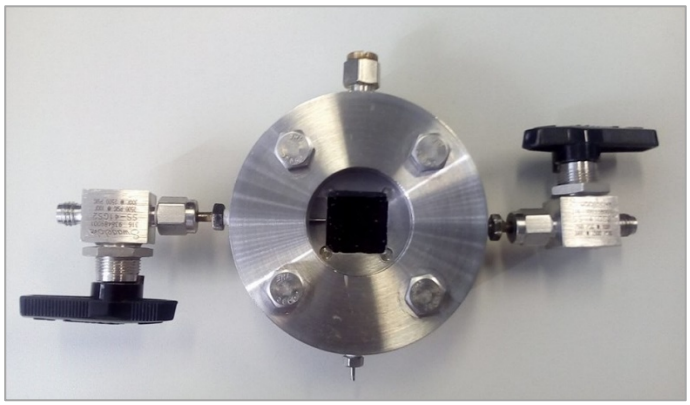

FIGURE 5.1 - Reactor used to realize the CO_2 photoreduction in gas phase.

The photocatalytic reactions were performed at room temperature for 6 hours and the formed products were analyzed every one hour by gas chromatography (GC).

5.3 Results and discussion

The pCN-Nb heterostructures were prepared based on the heteroaggregation induced by the sonochemical method. As can be seen in FIGURE 5.2 nanoparticles of niobium pentoxide in distilled water exhibited zeta potential value of -25 mV, this negative character of the surface charges exhibited

by niobium oxides is attributed to surface hydroxyl groups distorting the crystal lattice and forming acid sites.[166] C_3N_4 particles synthesized by the traditional urea thermopolymerization method exhibited surface charge values of -15 mV. However, after protonation with HCl, the particles showed slightly positive surface charges (~ 3 mV), with a difference of ~ 18 mV relative to the untreated material. Thus, the difference in surface charge between the C_3N_4 and Nb_2O_5 particles which were 10 mV increases to 28 mV. This difference, combined with sonication favors spontaneous intimate contact between particles, based on purely electrostatic phenomena.[165]

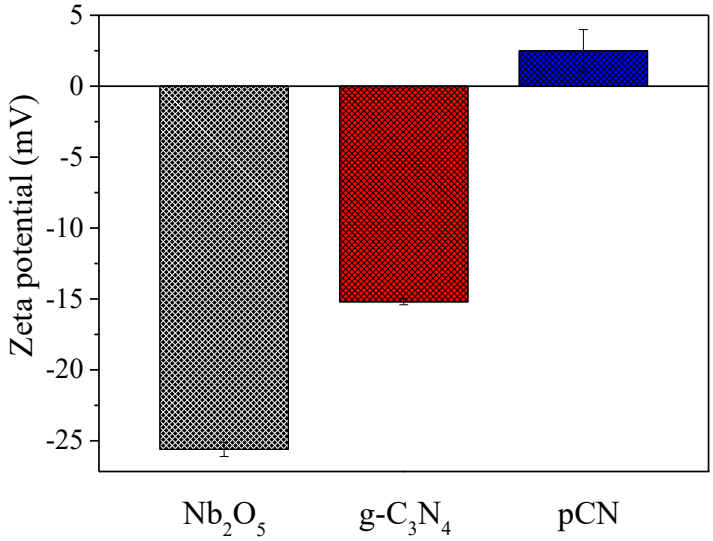

FIGURE 5.2 - Zeta potentials of Nb_2O_5, g-C_3N_4, and pCN at pH ~ 6.

XRD patterns of all synthesized samples were shown in FIGURE 5.3. It is possible to observe that the protonate C_3N_4 samples (pCN) have the typical crystallographic profile for C_3N_4, with two distinct peaks: one more weak at 13°, indexed to the (100) plane, that can be attributed to the in-plane structural packing motif tris-triazine units and another strong peak at 27°, indexed to the (002) plane, that can be attributed to the interlayer stacking of aromatic segments. These peaks are normally found in graphite-like stacking C_3N_4 layers according to JCPDS #87-1526.[72] Nb_2O_5 nanoparticles assisted by hydrothermal crystallization exhibited XRD pattern characteristics for the orthorhombic

phase(JCPDS #28-0317), however, it can be seen in FIGURE 5.3 that the crystallographic peaks are broad, indicating the low crystallinity of the synthesized material and confirming the acid and negative surface of the Nb_2O_5 nanoparticles.[13] The heterostructures obtained with different pCN and Nb_2O_5 proportions through the electrostatic induction heteroaggregation method presented the main characteristic diffraction peaks of both materials, however, it is possible to note that with the increase of the amount of niobium pentoxide in the mixtures, the presence of pCN peak decreased. For example, in the 75pCN-25Nb sample, it is possible to better identify the presence of the C_3N_4 plane-indexed (002) than in the 25pCN-75Nb sample. With this it is possible to confirm the presence of the two semiconductors in the heterostructures and that the difference of composition between the prepared mixtures.

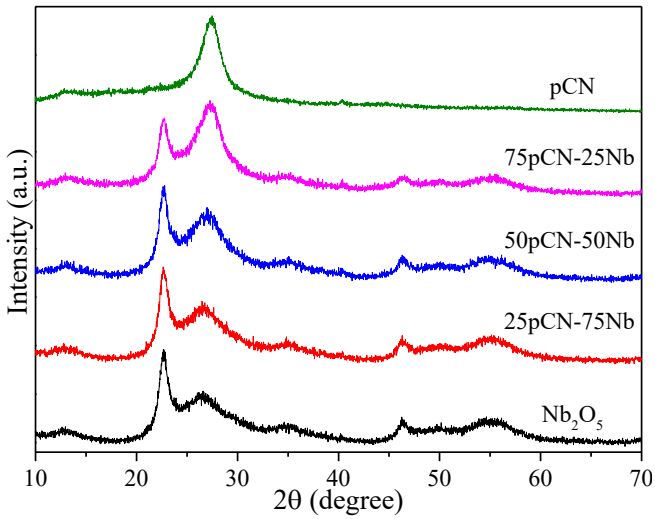

FIGURE 5.3 – XRD patterns of the pCN, Nb_2O_5, and heterostructured pCN-Nb samples.

In FIGURE 5.4 it is possible to observe different behaviors for the synthesized samples at high temperature. The C_3N_4 sample under oxidizing atmosphere undergoes complete thermal decomposition at 550 °C. On the other hand, Nb_2O_5, even annealed at 700 °C, kept 80% of its initial mass, demonstrating its thermal. This loss of 20% was attributed to the loss of hydration and

crystallization water molecules, or even to the loss of precursor residues. The synthesized heterostructures have different thermal degradation profiles, and the samples contain the highest amount of C_3N_4, which suffer the greatest degradation. Thus, it can be observed that the synthesized heterostructures, maintained a proportion between the semiconductors near the beginning of the synthesis, demonstrating through the whole proposed one can obtain a controlled synthesis of the amount of mass in the heterostructures.

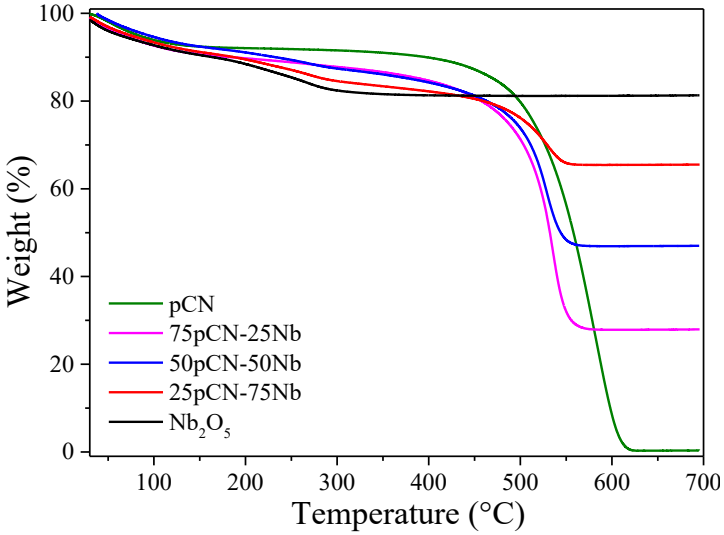

FIGURE 5.4 - Thermogravimetric curves (TG) of pCN, Nb_2O_5, and the pCN-Nb heterostructures.

The morphologies of all synthesized samples are shown in FIGURE 5.5. The pCN images show large particles with lamellar structure.[167] On the other hand, the synthesized Nb_2O_5 nanoparticles formed spherical agglomerates of approximately 30 nm.[13] In the representative images of the different pCN-Nb proportions, it is possible to observe the presence of both morphologies, . In addition, Nb_2O_5 nanoparticles are homogeneous distributed over pCN lamellae, indicating that the proposed method promoted intimate contact between the semiconductors throughout the surface of the pCN.

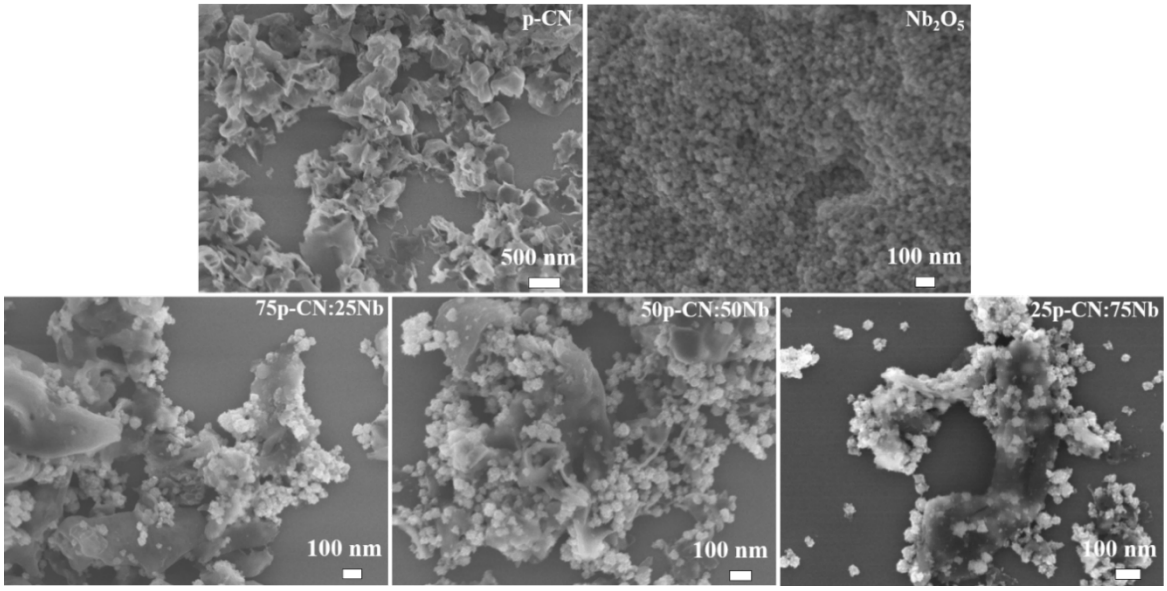

FIGURE 5.5 – Representative SEM images of the pCN, Nb_2O_5, and heterostructured pCN-Nb samples.

The optical properties of the as-prepared PCN, Nb_2O_5, and the pCN-Nb_2O_5 (pCN-Nb) heterostructures were measured by the UV−vis DRS technique. As shown in TABLE 5.1 and FIGURE 5.6, the absorption edge of the pCN and Nb_2O_5 pure are at 2.9 and 3.3 eV, respectively.[72] However, after mixing different proportions of Nb_2O_5 nanoparticles under the pCN surface via sonication, the optical absorption of the heterostructures maintained the characteristics of the pCN (2.8 eV), regardless of the amount of Nb_2O_5. Therefore, these results of UV−vis DRS suggest that the fabrication of the heterostructured pCN-Nb composites can greatly improve the optical absorption property and increase the utilized efficiency of solar light, which are favorable for the enhancement of the photocatalytic activity.

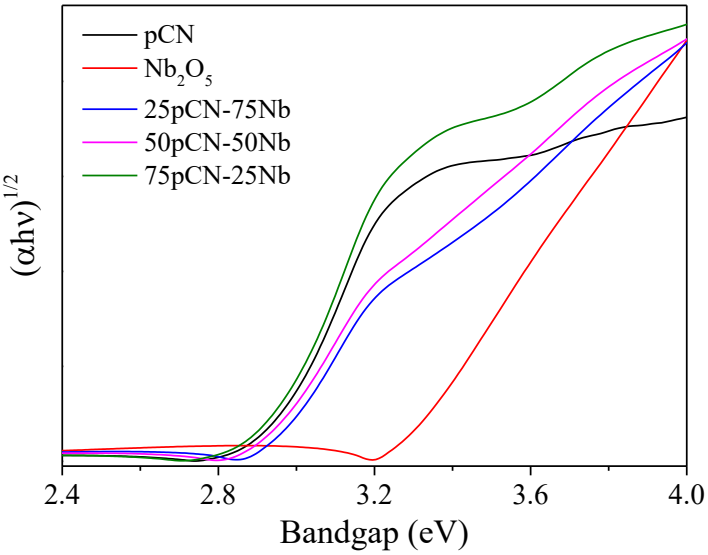

FIGURE 5.6 - Tauc plot for the different synthesized samples.

TABLE 5.1 - Physicochemical properties of the protonate g-C_3N_4 (pCN), Nb_2O_5, and heterostructured PCN/Nb samples.

Sample	SSA (m^2 g^{-1})	Calculated	Band gap (eV)
Nb_2O_5	204.6	-	3.3
25pCN-75Nb	154.5	164.4	2.9
50pCN-50Nb	130.3	124.2	2.9
75pCN-25Nb	80.3	83.9	2.9
pCN	43.7	-	2.9

The BET specific surface areas of the as-prepared samples were measured by N_2 adsorption/desorption equilibrium and the data are listed in TABLE 5.1. The specific surface area values measured for the pure pCN and Nb_2O_5 samples were in agreement with the literature reports, which show between 40 m^2 g^{-1} for C_3N_4 samples obtained from urea and 200 m^2 g^{-1} for samples of Nb_2O_5 synthesized via hydrothermal crystallization.[13,156] This difference between the specific surface areas of the pure materials was expected because as observed in the images representative of SEM, the Nb_2O_5 particles are smaller than the C_3N_4 lamellae, which confers a larger surface area specific to the material.

5.3.1 Photocatalytic activity test

The photo-reduction of CO_2 to CH_4 under UV irradiation was applied to evaluate photoactivity of the as-synthesized photocatalysts. To exclude the thermal-induced catalytic conversion of CO_2 and the possibility of surface organic contaminants that may be converted into CH_4, background tests were conducted by introducing $N_2 + H_2O$ vapor to the reactor in the presence of the as-synthesized photocatalysts. The amount of CH_4 produced was not detectable either in the dark or under photo-irradiation. This confirms that the produced CH_4 was indeed derived from photocatalytic CO_2 conversion.

Figure 5.7 shows the photocatalytic capacity of those synthesized for CO_2 conversion into CH_4 in gas phase reactions under UV radiation. The pure g-C_3N_4 showed a catalytic activity of approximately 3.2 times lower than the pure Nb_2O_5, i.e. 4.27 μmol h^{-1} g^{-1} and 13.57 μmol h^{-1} g^{-1}, respectively. This may be associated with fast recombination of photogenerated electron-hole pairs, typical behavior of these isolated semiconductors.[63,168] However, when analyzing the amount of methane produced by the synthesized heterostructures, it is observed that all of them present photocatalytic activity of CO_2 conversion into CH_4 higher than pure materials, regardless of the pCN-Nb ratio, demonstrating that the difference-induced heteroaggregation method can be an interesting and efficient strategy for the formation of promising candidates for the conversion of CO_2 into hydrocarbons.

Comparing the methane production between the synthesized heterostructures, it is possible observed that the samples 75pCN-25Nb and 25pCN-75Nb exhibit higher photocatalytic efficiency than 50pCN-50Nb. Despite this effect is not yet totally understood, this indicates that the preferential exposition of one phase is necessary to improve the photoactivity.[67] In fact, this indicates that high relative proportions of components (about 1:1, i.e., 50% of each material) lead to complete coverage of one surface, making the process in

the other material difficult. Therefore, since this is a redox process, it is necessary that both materials can be assessable to the medium.

However, when comparing the methane production obtained by the sample 75pCN-25Nb (32.4 μmol h^{-1} g^{-1}) it is observed a photocatalytic efficiency 2.4 times greater than pure Nb_2O_5 and 7.6 times greater than pure pCN. The 25pCN-75Nb sample (24.2 μmol h^{-1} g^{-1}) has a photocatalytic efficiency for CO_2 conversion into methane 1.8 times higher than pure Nb_2O_5 and 5.3 times higher than pure pCN, thus demonstrating that although samples show good photocatalytic performance for conversion of CO_2 to sample with a higher amount of pCN is more efficient than pure materials.

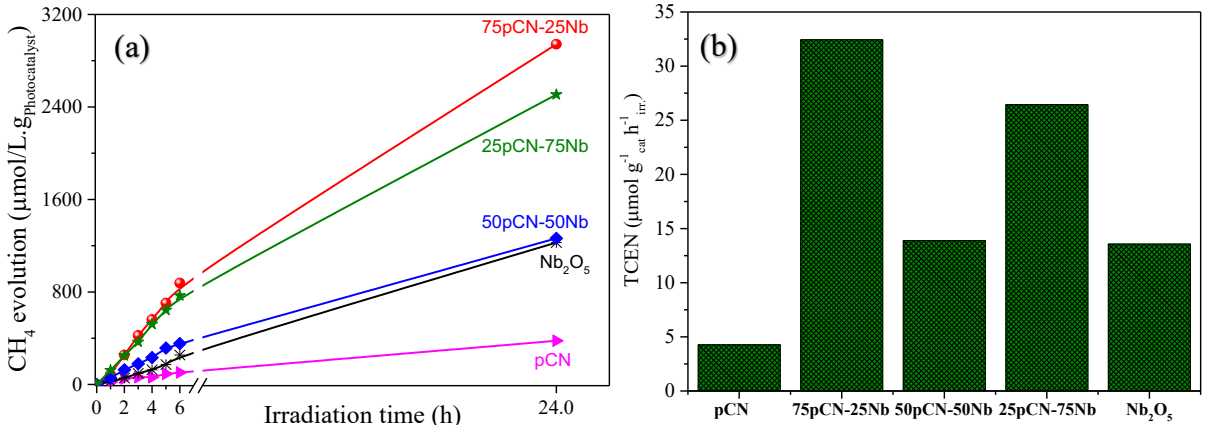

FIGURE 5.7 - Photoreduction of CO_2 to CH_4 for g-C_3N_4, Nb_2O_5, and heterostructured g-C_3N_4/Nb_2O_5 samples.

It is better to estimate the CO_2 reduction efficiency was estimate considering the total consumed electron number (TCEN) per unit reaction time and unit mass of photocatalyst, which can be calculated by using the product amount and the incident photon number as shown in the equation below.

$$TCEN = \frac{\sum(c_{product}\ x\ n_{electrons})\ x\ V_{reactor}}{m_{cat}\ x\ t_{irr.}}$$

where TCEN is the total consumed electron number for the photocatalytic CO_2 conversion, $V_{reactor}$ is the reactor volume, $ti_{rr.}$ is the irradiation time, $m_{cat.}$ is the catalyst mass, $c_{product}$ is the concentration of a certain product of CO_2 conversion, and $n_{electrons}$ is the corresponding consumed electrons per mole of the certain product. In addition, H_2 is not considered to calculate the TCEN in the following chapters because it is not converted from CO_2 directly.[169]

As can be seen in FIGURE 5.7b, the amount of electrons consumed by heterostructures in CO_2 photoreduction reactions is greater than that of pure materials, confirming that the synthesized heterostructures are more efficient in promoting the photocatalytic reduction of CO_2 in CH_4. This efficiency may be related to the capacity that the formation of heterostructures between two semiconductors has to decrease the recombination time of the photogenerated charge carriers.[38]

Photoluminescence spectroscopy provides important information about the behavior of the photogenerated charges in a semiconductor, as can be seen in figure 5.8, the pure pCN sample and the heterostructures present luminescence when excited at 390 nm, however the pure Nb_2O_5 sample does not it presents an answer that was expected, as could be observed in the DRS, this sample is activated only with energy of approximately 365 nm, unlike the other synthesized samples.[170]

However, when comparing the spectroscopic behavior of the synthesized heterostructures and pure pCN, it is observed a decrease in emitted luminescence. This can be related to loss of energy in the form of phono, a characteristic behavior of materials that have load sharing, because when activated the electrons of the located in the valence band are promoted to conduction band that in turn instead of returning again the valence band is transferred to the conduction band of the semiconductor coupled to it, this phenomenon decreases the intensity of the photons emitted, since part of that

energy used returns to the valence band in a longer time and at a lower intensity.[171]

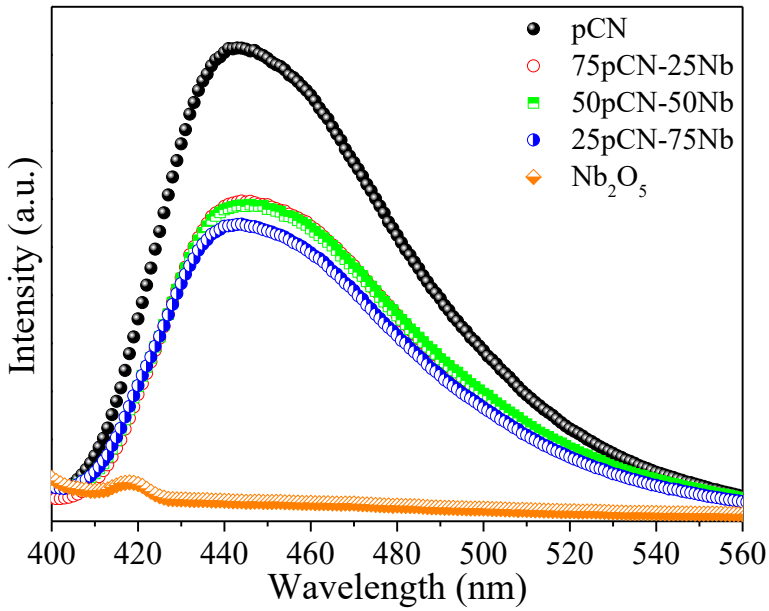

FIGURE 5.8 - Solid photoluminescence spectra of pCN, Nb_2O_5, and heterostructured pCN-Nb samples.

5.4 Conclusions

The proposed C_3N_4 surface protonation method to promote heteroaggregation by electrostatic attraction with Nb_2O_5 was an efficient strategy to form heterostructures of different pCN-Nb proportions capable of catalyzing the CO_2 reduction reaction in CH_4. All the synthesized heterostructures exhibited better photocatalytic performance than the pure materials, indicating that the formation of heterojunctions between the two semiconductors and that this phenomenon was fundamental for the increased activity of these materials, combinate with the specific surface area. The 75pCN-25Nb and 25pCN-75Nb samples exhibited the best photocatalytic activity for conversion of CO_2 into CH_4 between the synthesized samples. However, the 75pCN-25Nb sample exhibited higher catalytic performance, demonstrating that a larger amount of CN contributes more to photocatalytic activity than other prepared heterostructures. This is probably due to the higher absorption of the incident electromagnetic

radiation, because although they exhibit band gap value even of the other formed heterostructures, the greater amount of C_3N_4 induces a greater absorption of the radiation in the same wavelength. The intimate contact and sharing of the photogenerated charges were confirmed by the photoluminescent response of the synthesized samples, where can observed that all the synthesized heterostructures present a decrease of their emission in relation to the pure C_3N_4.

6 GENERAL CONCLUSIONS

In this thesis, it was possible to successfully understand the photocatalytic behavior of Nb_2O_5 and g-C_3N_4 in oxidizing and reducing processes. As well as the mechanism of formation of the Nb_2O_5/g-C_3N_4 heterostructures via the sonochemical method of electrostatic induction heteroaggregation, aiming at an improvement of its photocatalytic properties.

Nb_2O_5, when subjected to high temperatures, loses surface hydroxyls which gives Lewis and Brønsted acid characteristics and has its crystalline structure changed from a solid with low crystallinity to the pseudohexagonal phase. This superficial acidity, characteristic of the materials synthesized at lower temperatures, has low interaction with CO, the main intermediary of CO_2 photoreduction reactions. Therefore, when the CO is formed, it passes rapidly to the reaction medium and subsequently to the reaction headspace, due to its low solubility. The small fraction of CO present in the solution in contact with the surface of Nb_2O_5 is then converted to the other products in which the catalyst was selective, CH_4, HCOOH and CH_3COOH.

The g-C_3N_4/Nb_2O_5 heterostructures were successfully formed and exhibited high photocatalytic activity for the degradation of organic compounds under visible radiation and the CO_2 photoreduction under UV radiation. In addition, it can be observed that the CN/Nb ratios exhibited different performances against the molecules to be degraded, the sample with the highest amount of Nb had a higher selectivity for AML degradation, compared to the other analyzed samples, this can be associated with the interaction of the surface acidity of Nb with the basic groups of the structure in the drug. The main mechanism used by the CN/Nb heterostructures synthesized for the degradation of the molecules evaluated was the direct and indirect degradations, through the formation of a hole and of hydroxyl radicals, respectively. In addition, the heterostructures, as well as characteristics of the g-C_3N_4 and Nb_2O_5 materials, separately, presented high photostability, after successive cycles of reuse of the

catalyst, proving to be a promising alternative for photocatalytic processes for environmental remediation.

With regard to the photocatalytic efficiency of the g-C_3N_4/Nb_2O_5 heterostructures for the CO_2 conversion into CH_4, it can be concluded that the heterostructures with the highest CN/Nb ratios exhibit better photocatalytic performances, since the preferential exposure of one of the phases is required the process takes place efficiently.

7 REFERENCES

[1] S. Chu, A. Majumdar, Opportunities and challenges for a sustainable energy future, Nature. 488 (2012) 294–303. doi:10.1038/nature11475.

[2] J. Huang, H. Yu, A. Dai, Y. Wei, L. Kang, Drylands face potential threat under 2 °C global warming target, Nat. Clim. Chang. 7 (2017) 417–422. doi:10.1038/nclimate3275.

[3] J. Liu, B. Wang, M.A. Cane, S.-Y. Yim, J.-Y. Lee, Divergent global precipitation changes induced by natural versus anthropogenic forcing, Nature. 493 (2013) 656–659. doi:10.1038/nature11784.

[4] G. Centi, E.A. Quadrelli, S. Perathoner, Catalysis for CO_2 conversion: a key technology for rapid introduction of renewable energy in the value chain of chemical industries, Energy Environ. Sci. 6 (2013) 1711. doi:10.1039/c3ee00056g.

[5] WMO, WMO Greenhouse Gas Bulletin, World Meteorol. Organ. Bull. (2017) 1–4. doi:ISSN 2078-0796.

[6] S.A. Montzka, E.J. Dlugokencky, J.H. Butler, Non-CO_2 greenhouse gases and climate change, Nature. 476 (2011) 43–50. doi:10.1038/nature10322.

[7] S. Holloway, Storage of Fossil Fuel-derived carbon dioxide beneath the Surface of the Earth, Annu. Rev. Energy Environ. 26 (2002) 201–235. doi:10.1146/annurev.energy.26.1.201.

[8] Q. Wang, J. Luo, Z. Zhong, A. Borgna, CO2 capture by solid adsorbents and their applications: Current status and new trends, Energy Environ. Sci. 4 (2011) 42–55. doi:10.1039/c0ee00064g.

[9] L. Yuan, Y.-J. Xu, Photocatalytic conversion of CO_2 into value-added and renewable fuels, Appl. Surf. Sci. 342 (2015) 154–167. doi:10.1016/j.apsusc.2015.03.050.

[10] S.N. Habisreutinger, L. Schmidt-Mende, J.K. Stolarczyk, Photocatalytic reduction of CO_2 on TiO_2 and other semiconductors, Angew. Chemie - Int. Ed. 52 (2013) 7372–7408. doi:10.1002/anie.201207199.

[11] T. Inoue, A. Fujishima, S. Konishi, K. Honda, Photoelectrocatalytic reduction of carbon dioxide in aqueous suspensions of semiconductor powders, Nature. 277 (1979) 637–638. doi:10.1038/277637a0.

[12] O.F. Lopes, V.R. De Mendonça, F.B.F. Silva, E.C. Paris, C. Ribeiro, Niobium Oxides: An Overview of the Synthesis of Nb2O5 and its Application in Heterogeneous Photocatalysis, Quim. Nova. 38 (2015) 106–117. doi:10.5935/0100-4042.20140280.

[13] O.F. Lopes, E.C. Paris, C. Ribeiro, Synthesis of Nb_2O_5 nanoparticles through the oxidant peroxide method applied to organic pollutant photodegradation: A mechanistic study, Appl. Catal. B Environ. 144 (2014) 800–808.

[14] D.M. Schultz, T.P. Yoon, Solar synthesis: Prospects in visible light photocatalysis, Science (80-.). 343 (2014). doi:10.1126/science.1239176.

[15] D. Masih, Y. Ma, S. Rohani, Graphitic C_3N_4 based noble-metal-free photocatalyst systems : A review, Appl. Catal. B Environ. 206 (2017) 556–588. doi:10.1016/j.apcatb.2017.01.061.

[16] S. Cao, J. Low, J. Yu, M. Jaroniec, Polymeric photocatalysts based on graphitic carbon nitride, Adv. Mater. 27 (2015) 2150–2176. doi:10.1002/adma.201500033.

[17] W.-J. Ong, L.-L. Tan, Y.H. Ng, S.-T. Yong, S.-P. Chai, Graphitic Carbon Nitride (g-C_3N_4)-Based Photocatalysts for Artificial Photosynthesis and Environmental Remediation: Are We a Step Closer To Achieving Sustainability?, Chem. Rev. (2016) acs.chemrev.6b00075. doi:10.1021/acs.chemrev.6b00075.

[18] T. Su, Q. Shao, Z. Qin, Z. Guo, Z. Wu, Role of Interfaces in Two-Dimensional Photocatalyst for Water Splitting, ACS Catal. 8 (2018) 2253–2276. doi:10.1021/acscatal.7b03437.

[19] T. Xiong, W. Cen, Y. Zhang, F. Dong, Bridging the g-C3N4 Interlayers for Enhanced Photocatalysis, ACS Catal. 6 (2016) 2462–2472. doi:10.1021/acscatal.5b02922.
[20] X.-B. Li, L.-Z. Wu, C. Ye, L.-P. Zhang, X.-B. Fan, J.-X. Li, C.-H. Tung, Z.-J. Li, B. Chen, Enhanced Driving Force and Charge Separation Efficiency of Protonated g-C 3 N 4 for Photocatalytic O 2 Evolution , ACS Catal. 5 (2015) 6973–6979. doi:10.1021/acscatal.5b02185.
[21] J. Fu, J. Yu, C. Jiang, B. Cheng, g-C_3N_4-Based Heterostructured Photocatalysts, Adv. Energy Mater. 1701503 (2018) 1–31. doi:10.1002/aenm.201701503.
[22] A. Fujishima, K. Honda, Electrochemical photolysis of water at a semiconductor electrode, Nature. 238 (1972) 37–38. doi:10.1038/238037a0.
[23] N. Serpone, A.V. Emeline, Semiconductor Photocatalysis - Past, Present, and Future Outlook, J. Phys. Chem. Lett. 3 (2012) 673–677. doi:10.1021/jz300071j.
[24] A. Kudo, Y. Miseki, Heterogeneous photocatalyst materials for water splitting, Catal. Surv. from Asia. 38 (2009) 31–38. doi:10.1039/b800489g.
[25] S. Ouyang, Y. Bi, N. Umezawa, J. Ye, H. Tong, M. Oshikiri, Nano-photocatalytic Materials: Possibilities and Challenges, Adv. Mater. 24 (2011) 229–251. doi:10.1002/adma.201102752.
[26] T. Hisatomi, J. Kubota, K. Domen, Recent advances in semiconductors for photocatalytic and photoelectrochemical water splitting, Chem. Soc. Rev. 43 (2014) 7520–7535. doi:10.1039/c3cs60378d.
[27] S.C. Markham, Photocatalytic properties of oxides, J. Chem. Educ. 32 (1955) 540. doi:10.1021/ed032p540.
[28] W. Doerffler, K. Hauffe, Heterogeneous photocatalysis I. The influence of oxidizing and reducing gases on the electrical conductivity of dark and illuminated zinc oxide surfaces, J. Catal. 3 (1964) 156–170. doi:10.1016/0021-9517(64)90123-X.
[29] W. Doerffler, K. Hauffe, Heterogeneous photocatalysis II. The mechanism of the carbon monoxide oxidation at dark and illuminated zinc oxide surfaces, J. Catal. 3 (1964) 171–178. doi:10.1016/0021-9517(64)90124-1.
[30] Y. Qu, X. Duan, Progress, challenge and perspective of heterogeneous photocatalysts., Chem. Soc. Rev. 42 (2013) 2568–80. doi:10.1039/c2cs35355e.
[31] E. Karamian, S. Sharifnia, On the general mechanism of photocatalytic reduction of CO_2, J. CO2 Util. 16 (2016) 194–203. doi:10.1016/j.jcou.2016.07.004.
[32] W.Y. Teoh, J. a. Scott, R. Amal, Progress in Heterogeneous Photocatalysis: From Classical Radical Chemistry to Engineering Nanomaterials and Solar Reactors, J. Phys. Chem. Lett. 3 (2012) 629–639. doi:10.1021/jz3000646.
[33] M. Grätzel, Photoelectrochemical cells., Nature. 414 (2001) 338–344. http://www.ncbi.nlm.nih.gov/pubmed/11713540.
[34] S. Tojo, T. Tachikawa, M. Fujitsuka, T. Majima, Oxidation processes of aromatic sulfides by hydroxyl radicals in colloidal solution of TiO_2 during pulse radiolysis, Chem. Phys. Lett. 384 (2004) 312–316. doi:10.1016/j.cplett.2003.11.109.
[35] T. Sawyer, S. Valentine, How Super Superoxide?, Acc. Chem. Res. (1981) 393–400.
[36] S.S. Meryem, S. Nasreen, M. Siddique, R. Khan, An overview of the reaction conditions for an efficient photoconversion of CO_2, Rev. Chem. Eng. 34 (2017). doi:10.1515/revce-2016-0016.
[37] J. Mao, K. Li, T. Peng, Recent advances in the photocatalytic CO_2 reduction over semiconductors, Catal. Sci. Technol. 3 (2013) 2481. doi:10.1039/c3cy00345k.
[38] X. Li, J. Yu, M. Jaroniec, Hierarchical photocatalysts, Chem. Soc. Rev. 45 (2016) 2603–2636. doi:10.1039/c5cs00838g.
[39] K. Nakata, A. Fujishima, TiO2 photocatalysis: Design and applications, J. Photochem. Photobiol. C Photochem. Rev. 13 (2012) 169–189. doi:10.1016/j.jphotochemrev.2012.06.001.

[40] K. Hashimoto, H. Irie, A. Fujishima, TiO2 Photocatalysis : A Historical Overview and Future Prospects, Jpn. J. Appl. Phys. 44 (2005) 8269–8285. doi:10.1143/JJAP.44.8269.
[41] Y. Zhao, X. Zhou, L. Ye, S.C.E. Tsang, Nanostructured Nb_2O_5 catalysts, Nano Rev. 3 (2012) 1–11. doi:10.3402/nr.v3i0.17631.
[42] M. Ziolek, I. Sobczak, The role of niobium component in heterogeneous catalysts, Catal. Today. 285 (2017) 211–225. doi:10.1016/j.cattod.2016.12.013.
[43] A.G.S.A.G.S. Prado, L.B. Bolzon, C.P. Pedroso, A.O. Moura, L.L. Costa, Nb_2O_5 as efficient and recyclable photocatalyst for indigo carmine degradation, Appl. Catal. B Environ. 82 (2008) 219–224. doi:10.1016/j.apcatb.2008.01.024.
[44] K.M.A. Santos, E.M. Albuquerque, L.E.P. Borges, M.A. Fraga, Discussing Lewis and Brønsted acidity on continuous pyruvaldehyde Cannizzaro reaction to lactic acid over solid catalysts, Mol. Catal. (2017). doi:10.1016/j.mcat.2017.12.010.
[45] T. Murayama, J. Chen, J. Hirata, K. Matsumoto, W. Ueda, Hydrothermal synthesis of octahedra-based layered niobium oxide and its catalytic activity as a solid acid, Catal. Sci. Technol. 4 (2014) 4250–4257. doi:10.1039/C4CY00713A.
[46] Y. Zhao, X. Zhou, L. Ye, S. Chi Edman Tsang, Nanostructured Nb2O5 catalysts, Nano Rev. 3 (2012) 17631. doi:10.3402/nano.v3i0.17631.
[47] X. Chen, T. Yu, X. Fan, H. Zhang, Z. Li, J. Ye, Z. Zou, Enhanced activity of mesoporous Nb_2O_5 for photocatalytic hydrogen production, Appl. Surf. Sci. 253 (2007) 8500–8506. doi:10.1016/j.apsusc.2007.04.035.
[48] A. Esteves, L.C. a. Oliveira, T.C. Ramalho, M. Goncalves, A.S. Anastacio, H.W.P. Carvalho, New materials based on modified synthetic Nb_2O_5 as photocatalyst for oxidation of organic contaminants, Catal. Commun. 10 (2008) 330–332. doi:10.1016/j.catcom.2008.09.012.
[49] K. Skrodczky, M.M. Antunes, X. Han, S. Santangelo, A.A. Valente, N. Pinna, P.A. Russo, Niobium pentoxide nanomaterials with distorted structures as efficient acid catalysts, Commun. Chem. (2019) 1–11. doi:10.1038/s42004-019-0231-3.
[50] M.I. Litter, Heterogeneous photocatalysis Transition metal ions in photocatalytic systems, Appl. Catal. B Environ. 23 (1999) 89–114.
[51] M. Nan, B. Jin, C.W.K. Chow, C. Saint, Recent developments in photocatalytic water treatment technology: A review, Water Res. 44 (2010) 2997–3027. doi:10.1016/j.watres.2010.02.039.
[52] Y. Wang, Xinlong Ma, H. Li, B. Liu, H. Li, Shu Yin, T. Sato, Recent Advances in Visible-Light Driven Photocatalysis, in: Adv. Catal. Mater. - Photocatal. Other Curr. Trends Photoexcitation, 2016: pp. 337–358. doi:10.5772/32009.
[53] H. Wang, L. Zhang, Z. Chen, J. Hu, S. Li, Semiconductor heterojunction photocatalysts: design, construction, and photocatalytic, Chem. Soc. Rev. (2014). doi:10.1039/c4cs00126e.
[54] J.S. Jang, H.G. Kim, J.S. Lee, Heterojunction semiconductors: A strategy to develop efficient photocatalytic materials for visible light water splitting, Catal. Today. 185 (2012) 270–277. doi:10.1016/j.cattod.2011.07.008.
[55] A. Ibhadon, P. Fitzpatrick, Heterogeneous Photocatalysis: Recent Advances and Applications, Catalysts. 3 (2013) 189–218. doi:10.3390/catal3010189.
[56] J. Tian, Z. Zhao, A. Kumar, I. Boughton, H. Liu, Recent progress in design, synthesis, and applications of one-dimensional TiO2 nanostructured surface heterostructures: a review, Chem. Soc. Rev. (2014). doi:10.1039/c4cs00180j.
[57] N. Serpone, E. Borgarello, M. Grätzel, Visible light induced generation of hydrogen from H2S in mixed semiconductor dispersions; improved efficiency through inter-particle electron transfer, J. Chem. Soc. Chem. Commun. (1984) 342–344. doi:10.1039/C39840000342.
[58] M.R. Nellist, F.A.L. Laskowski, F. Lin, T.J. Mills, S.W. Boettcher, Semiconductor-

Electrocatalyst Interfaces: Theory, Experiment, and Applications in Photoelectrochemical Water Splitting, Acc. Chem. Res. 49 (2016) 733–740. doi:10.1021/acs.accounts.6b00001.

[59] H. Li, Y. Zhou, W. Tu, J. Ye, Z. Zou, State-of-the-art progress in diverse heterostructured photocatalysts toward promoting photocatalytic performance, Adv. Funct. Mater. 25 (2015) 998–1013. doi:10.1002/adfm.201401636.

[60] A.E. Nogueira, O.F. Lopes, A.B.S. Neto, C. Ribeiro, Enhanced Cr(VI) photoreduction in aqueous solution using Nb_2O_5/CuO heterostructures under UV and visible irradiation, Chem. Eng. J. 312 (2017) 220–227. doi:10.1016/j.cej.2016.11.135.

[61] Y. Hong, C. Li, G. Zhang, Y. Meng, B. Yin, Y. Zhao, W. Shi, Efficient and stable Nb_2O_5 modified g-C3N4 photocatalyst for removal of antibiotic pollutant, Chem. Eng. J. 299 (2016) 74–84. doi:10.1016/j.cej.2016.04.092.

[62] L.C.A. Oliveira, H.S. Oliveira, G. Mayrink, H.S. Mansur, A.A.P. Mansur, R.L. Moreira, One-pot synthesis of CdS@Nb2O5 core-shell nanostructures with enhanced photocatalytic activity, Appl. Catal. B Environ. 152–153 (2014) 403–412. doi:10.1016/j.apcatb.2014.01.025.

[63] J. Wu, J. Li, J. Liu, J. Bai, L. Yang, A novel Nb2O5/Bi2WO6 heterojunction photocatalytic oxidative desulfurization catalyst with high visible light-induced photocatalytic activity, RSC Adv. 7 (2017) 51046–51054. doi:10.1039/c7ra09829d.

[64] A. Thomas, A. Fischer, F. Goettmann, M. Antonietti, J.-O. Müller, R. Schlögl, J.M. Carlsson, Graphitic carbon nitride materials: variation of structure and morphology and their use as metal-free catalysts, J. Mater. Chem. 18 (2008) 4893. doi:10.1039/b800274f.

[65] G. Dong, Y. Zhang, Q. Pan, J. Qiu, A fantastic graphitic carbon nitride (g-C3N4) material: Electronic structure, photocatalytic and photoelectronic properties, J. Photochem. Photobiol. C Photochem. Rev. 20 (2014) 33–50. doi:10.1016/j.jphotochemrev.2014.04.002.

[66] Y. Zhang, T. Mori, J. Ye, Polymeric Carbon Nitrides: Semiconducting Properties and Emerging Applications in Photocatalysis and Photoelectrochemical Energy Conversion, Sci. Adv. Mater. 4 (2012) 282–291.

[67] G.T.S.T. Da Silva, K.T.G. Carvalho, O.F. Lopes, C. Ribeiro, g-C3N4/Nb2O5 heterostructures tailored by sonochemical synthesis: Enhanced photocatalytic performance in oxidation of emerging pollutants driven by visible radiation, Appl. Catal. B Environ. 216 (2017) 70–79. doi:10.1016/j.apcatb.2017.05.038.

[68] J. Fu, J. Yu, C. Jiang, B. Cheng, g-C3N4-Based Heterostructured Photocatalysts, Adv. Energy Mater. 8 (2018) 1–31. doi:10.1002/aenm.201701503.

[69] T. Rahman, G. Borah, P.K. Gogoi, Hybrid composite of CuO with g -C 3N 4 as a photoactive catalyst: an efficient approach for the oxidation of alcohols, J. Chem. Sci. 131 (2019) 1–9. doi:10.1007/s12039-018-1581-6.

[70] G.T.S.T. Da Silva, K.T.G. Carvalho, O.F. Lopes, E.S. Gomes, A.R. Malagutti, V.R. Mastelaro, C. Ribeiro, H.A.J.L. Mourão, Synthesis of ZnO Nanoparticles Assisted by N-Sources and their Application in the Photodegradation of Organic Contaminants, ChemCatChem. 9 (2017) 3795–3804. doi:10.1002/cctc.201700756.

[71] K. Wei, K. Li, L. Yan, S. Luo, H. Guo, Y. Dai, X. Luo, One-step fabrication of g-C3N4 nanosheets/TiO2 hollow microspheres heterojunctions with atomic level hybridization and their application in the multi-component synergistic photocatalytic, Appl. Catal. B Environ. 222 (2018) 88–98. doi:10.1016/j.apcatb.2017.09.070.

[72] K.T.G. Carvalho, A.E. Nogueira, O.F. Lopes, G. Byzynski, C. Ribeiro, Synthesis of g-C3N4/Nb2O5 heterostructures and their application on removal of organic pollutants under visible and ultraviolet irradiation, Ceram. Int. 43 (2016). doi:10.1016/j.ceramint.2016.11.063.

[73] W. Wang, H. Cheng, B. Huang, X. Liu, X. Qin, X. Zhang, Y. Dai, Hydrothermal synthesis of g-C3N4/BiOIO3 heterostructures with enhanced photocatalytic properties, J. Colloid Interface Sci. 442 (2015) 97–102. doi:10.1016/j.jcis.2014.11.061.
[74] Y. Tian, B. Chang, Z. Yang, B. Zhou, F. Xi, X. Dong, Graphitic carbon nitride–BiVO 4 heterojunctions: simple hydrothermal synthesis and high photocatalytic performances, RSC Adv. 4 (2014) 4187–4193. doi:10.1039/C3RA46079G.
[75] N. Siedl, S.O. Baumann, M.J. Elser, O. Diwald, Particle networks from powder mixtures: Generation of TiO_2-SnO_2 heterojunctions via surface charge-induced heteroaggregation, J. Phys. Chem. C. 116 (2012) 22967–22973. doi:10.1021/jp307737s.
[76] L. Sun, Y. Qi, C.-J. Jia, Z. Jin, W. Fan, Enhanced visible-light photocatalytic activity of g-C3N4/Zn2GeO4 heterojunctions with effective interfaces based on band match, Nanoscale. 6 (2014) 2649. doi:10.1039/c3nr06104c.
[77] C. Huntingford, L.M. Mercado, High chance that current atmospheric greenhouse concentrations commit to warmings greater than 1.5°C over land, Nat. Publ. Gr. (2016) 1–7.
[78] A. Stips, D. Macias, C. Coughlan, E. Garcia-gorriz, X.S. Liang, On the causal structure between CO_2 and global temperature, Sci. Rep. (2016) 1–9.
[79] WMO, The State of Greenhouse Gases in the Atmosphere Based on Global Observations through 2016, Greenh. Gas Bull. (2017) 1–4.
[80] K. Li, X. An, K. Hyeon, M. Khraisheh, J. Tang, A critical review of CO_2 photoconversion : Catalysts and reactors, Catal. Today. 224 (2014) 3–12. doi:10.1016/j.cattod.2013.12.006.
[81] S. Bai, W. Yin, L. Wang, Z. Li, Y. Xiong, Surface and interface design in cocatalysts for photocatalytic water splitting and CO2 reduction, RSC Adv. 6 (2016) 57446–57463. doi:10.1039/C6RA10539D.
[82] Y. He, Y. Wang, L. Zhang, B. Teng, M. Fan, High-efficiency conversion of CO_2 to fuel over ZnO/g-C_3N_4 photocatalyst, Appl. Catal. B Environ. 168–169 (2015) 1–8. doi:10.1016/j.apcatb.2014.12.017.
[83] Z. Li, J. Feng, S. Yan, Z. Zou, Solar fuel production: Strategies and new opportunities with nanostructures, Nano Today. (2015) 1–19.
[84] X. Liu, S. Inagaki, J. Gong, Heterogeneous Molecular Systems for Photocatalytic CO_2 Reduction with Water Oxidation, Angew. Chemie - Int. Ed. 55 (2016) 14924–14950. doi:10.1002/anie.201600395.
[85] J. Kou, C. Lu, J. Wang, Y. Chen, Z. Xu, R.S. Varma, Selectivity Enhancement in Heterogeneous Photocatalytic Transformations, Chem. Rev. 117 (2017) 1445–1514. doi:10.1021/acs.chemrev.6b00396.
[86] J.A. Oliveira, A.E. Nogueira, M.C.P. Gonc, E.C. Paris, C. Ribeiro, G.Y. Poirier, T.R. Giraldi, Photoactivity of N-doped ZnO nanoparticles in oxidative and reductive reactions, Appl. Surf. Sci. 433 (2018) 879–886. doi:10.1016/j.apsusc.2017.10.110.
[87] I.H. Tseng, W.C. Chang, J.C.S. Wu, Photoreduction of CO_2 using sol-gel derived titania and titania-supported copper catalysts, Appl. Catal. B Environ. 37 (2002) 37–48. doi:10.1016/S0926-3373(01)00322-8.
[88] Q. Li, L. Zong, C. Li, J. Yang, Photocatalytic reduction of CO_2 on MgO/TiO_2 nanotube films, Appl. Surf. Sci. 314 (2014) 458–463. doi:10.1016/j.apsusc.2014.07.019.
[89] F. Sastre, A. Corma, H. García, 185 nm photoreduction of CO2 to methane by water. Influence of the presence of a basic catalyst, J. Am. Chem. Soc. 134 (2012) 14137–14141. doi:10.1021/ja304930t.
[90] K. Bhattacharyya, A. Danon, B.K. Vijayan, K.A. Gray, P.C. Stair, E. Weitz, Role of the Surface Lewis Acid and Base Sites in the Adsorption of CO_2 on Titania Nanotubes and Platinized Titania Nanotubes : An in Situ FT-IR Study, J. Phys. Chem. C. 117

(2013) 12661–12678.
[91] S. Civiš, M. Ferus, A. Knížek, P. Kubelík, L. Kavan, M. Zukalová, Photocatalytic transformation of CO_2 to CH_4 and CO on acidic surface of TiO2anatase, Opt. Mater. (Amst). 56 (2016) 80–83. doi:10.1016/j.optmat.2015.11.015.
[92] J. Jiao, Y. Wei, Y. Zhao, Z. Zhao, A. Duan, J. Liu, Y. Pang, J. Li, G. Jiang, Y. Wang, AuPd/3DOM-TiO2 catalysts for photocatalytic reduction of CO2: High efficient separation of photogenerated charge carriers, Appl. Catal. B Environ. 209 (2017) 228–239. doi:10.1016/j.apcatb.2017.02.076.
[93] M.L. Marin, G.L. Hallett-tapley, S. Impellizzeri, C. Fasciani, S. Simoncelli, C. Netto-ferreira, J.C. Scaiano, Synthesis, acid properties and catalysis by niobium oxide nanostructured materials, Catal. Sci. Technol. 4 (2014) 3044–3052. doi:10.1039/c4cy00238e.
[94] S. Hayashi, M. Hara, K. Nakajima, Y. Baba, R. Noma, M. Kitano, J.N. Kondo, S. Hayashi, M. Hara, $Nb_2O_5.nH_2O$ as a Heterogeneous Catalyst with Water-Tolerant Lewis Acid Sites, J. Am. Chem. Soc. 133 (2011) 4224–4227. doi:10.1016/j.ijleo.2015.05.036.
[95] O.F. Lopes, V.R. De Mendonça, F.B.F. Silva, E.C. Paris, C. Ribeiro, Niobium Oxides: An Overview of the Synthesis of Nb_2O_5 and its Application in Heterogeneous Photocatalysis, Quim. Nova. 38 (2014) 106–117. doi:10.5935/0100-4042.20140280.
[96] H. Liu, N. Gao, M. Liao, X. Fang, Hexagonal-like Nb_2O_5 Nanoplates-Based Photodetectors and Photocatalyst with High Performances, Sci. Rep. 5 (2015) 7716. doi:10.1038/srep07716.
[97] E.V. Savinkina, L.N. Obolenskaya, G.M. Kuzmicheva, I.D. Morozov, R.G. Chumakov, Effects of peroxo precursors and annealing temperature on properties and photocatalytic activity of nanoscale titania, J. Mater. Res. 33 (2018) 1422–1432. doi:10.1557/jmr.2018.52.
[98] L. Forni, Comparison of the Methods for the Determination of Surface Acidity of Solid Catalysts, Catal. Rev. Sci. Eng. (2012) 37–41.
[99] C. Guo, Z. Qian, Acidic and catalytic properties of niobic acid crystallized at low temperature, Catal. Today. 16 (1993) 379–385.
[100] S. Li, Q. Xu, E. Uchaker, X. Cao, G. Cao, Comparison of amorphous, pseudohexagonal and orthorhombic Nb_2O_5 for high-rate lithium ion insertion, CrystEngComm. 18 (2016) 2532–2540. doi:10.1039/c5ce02069g.
[101] J. Xue, R. Wang, Z. Zhang, S. Qiu, Facile preparation of C, N co-modified Nb_2O_5 nanoneedles with enhanced visible light photocatalytic activity, Dalt. Trans. 45 (2016) 16519–16525. doi:10.1039/C6DT03548E.
[102] M. Ristic, S. Popovic, S. Music, Sol-gel synthesis and characterization of Nb_2O_5 powders, Mater. Lett. 58 (2004) 2658–2663. doi:10.1016/j.matlet.2004.03.041.
[103] E.R. Leite, C. Vila, J. Bettini, E. Longo, Synthesis of Niobia Nanocrystals with Controlled Morphology, J. Phys. Chem. B. 110 (2006) 18088–18090.
[104] C. Paraguassú Cecchi, D. Cesarín-Sobrinho, A. Buarque Ferreira, J. Netto-Ferreira, New Insights on the Oxidation of Unsaturated Fatty Acid Methyl Esters Catalyzed by Niobium(V) Oxide. A Study of the Catalyst Surface Reactivity, Catalysts. 8 (2018) 6. doi:10.3390/catal8010006.
[105] R.F. Brandão, R.L. Quirino, V.M. Mello, A.P. Tavares, A.C. Peres, F. Guinhos, J.C. Rubim, P.A.Z. Suarez, Synthesis, characterization and use of Nb_2O_5 based catalysts in producing biofuels by transesterification, esterification and pyrolysis, J. Braz. Chem. Soc. 20 (2009) 954–966. doi:10.1590/S0103-50532009000500022.
[106] X. Ma, Y. Chen, H. Li, X. Cui, Y. Lin, Annealing-free synthesis of carbonaceous Nb_2O_5 microspheres by flame thermal method and enhanced photocatalytic activity for hydrogen evolution, Mater. Res. Bull. 66 (2015) 51–58.

doi:10.1016/j.materresbull.2015.02.005.
[107] S. Ge, H. Jia, H. Zhao, Z. Zheng, L. Zhang, First observation of visible light photocatalytic activity of carbon modified Nb_2O_5 nanostructures, J. Mater. Chem. 20 (2010) 3052. doi:10.1039/b923586h.
[108] X. Chang, T. Wang, J. Gong, CO2 photo-reduction: Insights into CO2 activation and reaction on surfaces of photocatalysts, Energy Environ. Sci. 9 (2016) 2177–2196. doi:10.1039/C6EE00383D.
[109] T. Yui, A. Kan, C. Saitoh, K. Koike, T. Ibusuki, O. Ishitani, Photochemical reduction of CO_2 using TiO_2: effects of organic adsorbates on TiO_2 and deposition of Pd onto TiO_2., ACS Appl. Mater. Interfaces. 3 (2011) 2594–600. doi:10.1021/am200425y.
[110] M.E. Aguirre, R. Zhou, A.J. Eugene, M.I. Guzman, M.A. Grela, Cu_2O/TiO_2 heterostructures for CO_2 reduction through a direct Z-scheme: Protecting Cu_2O from photocorrosion, Appl. Catal. B Environ. 217 (2017) 485–493. doi:10.1016/j.apcatb.2017.05.058.
[111] E.L.P.J. V. Hillman, Carbon monoxide, in: R.D.H.M.B.T. Johnson (Ed.), Hamilt. Hardy's Ind. Toxicol., 6th ed., WILEY, 2015: pp. 309–316.
[112] J.A. Dean, Lange's Handbook of Chemistry, 15th ed., McGRAW-HILL, INC, 1999.
[113] R. Sander, Compilation of Henry's law constants (version 4.0) for water as solvent, Atmos. Chem. Phys. 15 (2015) 4399–4981. doi:10.5194/acp-15-4399-2015.
[114] IUPAC, Compendium of Chemical Terminology, 2nd ed., Blackwell Scientific Publications, Oxford, 1997.
[115] J.-P. Jones, G.K.S.K.S. Prakash, G.A.A. Olah, Electrochemical CO_2 Reduction: Recent Advances and Current Trends, Isr. J. Chem. 54 (2014) 1451–1466. doi:10.1002/ijch.201400081.
[116] S.R. Lingampalli, M.M. Ayyub, C.N.R. Rao, Recent Progress in the Photocatalytic Reduction of Carbon Dioxide, ACS Omega. 2 (2017) 2740–2748. doi:10.1021/acsomega.7b00721.
[117] J. Albo, M. Alvarez-Guerra, P. Castaño, A. Irabien, Towards the electrochemical conversion of carbon dioxide into methanol, Green Chem. 17 (2015) 2304–2324. doi:10.1039/c4gc02453b.
[118] D. Ren, J. Fong, B.S. Yeo, The effects of currents and potentials on the selectivities of copper toward carbon dioxide electroreduction, Nat. Commun. 9 (2018). doi:10.1038/s41467-018-03286-w.
[119] R. Kortlever, J. Shen, K.J.P. Schouten, F. Calle-vallejo, M.T.M. Koper, Catalysts and Reaction Pathways for the Electrochemical Reduction of Carbon Dioxide, J. Phys. Chem. Lett. 6 (2015) 4073–4082. doi:10.1021/acs.jpclett.5b01559.
[120] K.J.P. Schouten, Y. Kwon, C.J.M. van der Ham, Z. Qin, M.T.M. Koper, A new mechanism for the selectivity to C1 and C2 species in the electrochemical reduction of carbon dioxide on copper electrodes, Chem. Sci. 2 (2011) 1902. doi:10.1039/c1sc00277e.
[121] D. C., T. A., Metal-Support Interactions in Rh/CeO_2, Rh/TiO_2, and Rh/Nb_2O_5 Catalysts as Inferred from CO_2 Methanation Activity, J. Catal. 156 (1995) 174–174.
[122] Y. Zhao, Y. Wei, X. Wu, H. Zheng, Z. Zhao, J. Liu, J. Li, Graphene-wrapped Pt/TiO_2 photocatalysts with enhanced photogenerated charges separation and reactant adsorption for high selective photoreduction of CO_2 to CH_4, Appl. Catal. B Environ. 226 (2018) 360–372. doi:10.1016/j.apcatb.2017.12.071.
[123] Y. Wei, X. Wu, Y. Zhao, L. Wang, Z. Zhao, X. Huang, J. Liu, J. Li, Efficient photocatalysts of TiO_2 nanocrystals-supported PtRu alloy nanoparticles for CO_2 reduction with H_2O: Synergistic effect of Pt-Ru, Appl. Catal. B Environ. 236 (2018) 445–457. doi:10.1016/j.apcatb.2018.05.043.
[124] W.N. Wang, J. Soulis, Y. Jeffrey Yang, P. Biswas, Comparison of CO_2 photoreduction

systems: A review, Aerosol Air Qual. Res. 14 (2014) 533–549. doi:10.4209/aaqr.203.09.0283.
[125] Q. Guo, Q. Zhang, H. Wang, Z. Liu, Z. Zhao, Unraveling the role of surface property in the photoreduction performance of CO_2 and H_2O catalyzed by the modified ZnO, Mol. Catal. 436 (2017) 19–28. doi:10.1016/j.mcat.2017.04.014.
[126] C. Genovese, C. Ampelli, S. Perathoner, G. Centi, Mechanism of C-C bonf formation in the electrocatalytic reduction of CO_2 to acetic acid. A challenging reaction to use renewable energy with chemistry, Green Chem. (2017) 2406–2415. doi:10.1039/c6gc03422e.
[127] X. Sun, Q. Zhu, X. Kang, H. Liu, Q. Qian, J. Ma, Z. Zhang, G. Yang, B. Han, Design of a Cu(I)/C-doped boron nitride electrocatalyst for efficient conversion of CO2 into acetic acid., Green Chem. (2017) 2086–2091. doi:10.1039/c7gc00503b.
[128] Y.N.B. Li, D.E. Moore, B.N. Tattam, Photodegradation of amiloride in aqueous solution, Int. J. Pharm. 183 (1999) 109–116. doi:10.1016/S0378-5173(99)00035-6.
[129] P. Calza, C. Massolino, G. Monaco, C. Medana, C. Baiocchi, Study of the photolytic and photocatalytic transformation of amiloride in water, J. Pharm. Biomed. Anal. 48 (2008) 315–320. doi:10.1016/j.jpba.2008.01.014.
[130] M.B. Ahmed, J.L. Zhou, H.H. Ngo, W. Guo, N.S. Thomaidis, J. Xu, Progress in the biological and chemical treatment technologies for emerging contaminant removal from wastewater: A critical review, J. Hazard. Mater. 323 (2016) 274–298. doi:10.1016/j.jhazmat.2016.04.045.
[131] L. Lin, H. Wang, P. Xu, Immobilized TiO_2-reduced graphene oxide nanocomposites on optical fibers as high performance photocatalysts for degradation of pharmaceuticals, Chem. Eng. J. (2016). doi:10.1016/j.cej.2016.04.024.
[132] V.R. de Mendonça, H.A.J.L. Mourão, A.R. Malagutti, C. Ribeiro, The role of the relative dye/photocatalyst concentration in TiO_2 assisted photodegradation process, Photochem. Photobiol. 90 (2014) 66–72. doi:10.1111/php.12175.
[133] S. Martha, A. Nashim, K.M. Parida, Facile synthesis of highly active g-C_3N_4 for efficient hydrogen production under visible light, J. Mater. Chem. A. 1 (2013) 7816. doi:10.1039/c3ta10851a.
[134] X. Fan, Z. Xing, Z. Shu, L. Zhang, L. Wang, J. Shi, Improved photocatalytic activity of g-C_3N_4 derived from cyanamide–urea solution, RSC Adv. 5 (2015) 8323–8328. doi:10.1039/C4RA16362A.
[135] S. Cao, J. Yu, g-C_3N_4-Based Photocatalysts for Hydrogen Generation, J. Phys. Chem. Lett. 5 (2014) 2101–2107.
[136] Z. Zhao, Y. Sun, F. Dong, F. Dong, Graphitic carbon nitride based nanocomposites : a review, Nanoscale. (2015) 15–37. doi:10.1039/c4nr03008g.
[137] P. Niu, L. Zhang, G. Liu, H.M. Cheng, Graphene-like carbon nitride nanosheets for improved photocatalytic activities, Adv. Funct. Mater. 22 (2012) 4763–4770. doi:10.1002/adfm.201200922.
[138] Z. Jin, Q. Zhang, S. Yuan, T. Ohno, Synthesis high specific surface area nanotube g-C_3N_4 with two-step condensation treatment of melamine to enhance photocatalysis, RSC Adv. Supplement (2012) 1–4.
[139] H. Xu, J. Yan, X. She, L. Xu, J. Xia, Y. Xu, Y. Song, L. Huang, H. Li, Graphene-analogue carbon nitride: novel exfoliation synthesis and its application in photocatalysis and photoelectrochemical selective detection of trace amount of Cu^{2+}., Nanoscale. 6 (2014) 1406–15. doi:10.1039/c3nr04759h.
[140] G. Liu, P. Niu, C. Sun, S.C. Smith, Z. Chen, G.Q. (Max) Lu, H.-M. Cheng, Unique Electronic Structure Induced High Photoreactivity of Sulfur-Doped Graphitic C_3N_4, J. Am. Chem. Soc. 132 (2010) 11642–11648. doi:10.1021/ja103798k.
[141] S. Cao, J. Jiang, B. Zhu, J. Yu, Shape-dependent photocatalytic hydrogen evolution

activity over a Pt nanoparticle coupled g-C_3N_4 photocatalyst, Phys. Chem. Chem. Phys. 18 (2016) 19457–19463. doi:10.1039/C6CP02832B.
[142] Y. Wang, Q. Wang, X. Zhan, F. Wang, M. Safdar, J. He, Visible light driven type II heterostructures and their enhanced photocatalysis properties: a review., Nanoscale. 5 (2013) 8326–39. doi:10.1039/c3nr01577g.
[143] W. Shi, N. Chopra, Nanoscale heterostructures for photoelectrochemical water splitting and photodegradation of pollutants, Nanomater. Energy. 2 (2013) 158–178. doi:10.1680/nme.13.00009.
[144] X. Zhong, M. Jin, H. Dong, L. Liu, L. Wang, H. Yu, S. Leng, G. Zhuang, X. Li, J. Wang, TiO_2 nanobelts with a uniform coating of g-C_3N_4 as a highly effective heterostructure for enhanced photocatalytic activities, J. Solid State Chem. 220 (2014) 54–59. doi:10.1016/j.jssc.2014.08.016.
[145] J. Tian, Q. Liu, A.M. Asiri, X. Sun, Y. He, Ultrathin graphitic C_3N_4 nanofibers: Hydrolysis-driven top-down rapid synthesis and application as a novel fluorosensor for rapid, sensitive, and selective detection of Fe3+, Sensors Actuators B Chem. 216 (2015) 453–460. doi:10.1016/j.snb.2015.04.075.
[146] W. Wang, H. Cheng, B. Huang, X. Liu, X. Qin, X. Zhang, Y. Dai, Hydrothermal synthesis of C_3N_4/$BiOIO_3$ heterostructures with enhanced photocatalytic properties, J. Colloid Interface Sci. 442 (2015) 97–102. doi:10.1016/j.jcis.2014.11.061.
[147] S.M. Lam, J.C. Sin, I. Satoshi, A.Z. Abdullah, A.R. Mohamed, Enhanced sunlight photocatalytic performance over Nb2O5/ZnO nanorod composites and the mechanism study, Appl. Catal. A Gen. 471 (2014) 126–135. doi:10.1016/j.apcata.2013.12.001.
[148] T.A. Sedneva, E.P. Lokshin, M.L. Belikov, A.T. Belyaevskii, TiO2- and Nb2O5-based photocatalytic composites, Inorg. Mater. 49 (2013) 382–389. doi:10.1134/S0020168513040134.
[149] Z. Yue, D. Chu, H. Huang, J. Huang, P. Yang, Y. Du, M. Zhu, C. Lu, A novel heterogeneous hybrid by incorporation of Nb_2O_5 microspheres and reduced graphene oxide for photocatalytic H_2 evolution under visible light irradiation, RSC Adv. 5 (2015) 47117–47124. doi:10.1039/C5RA05348J.
[150] L.C.A. Oliveira, M. Gonçalves, M.C. Guerreiro, T.C. Ramalho, J.D. Fabris, M.C. Pereira, K. Sapag, A new catalyst material based on niobia/iron oxide composite on the oxidation of organic contaminants in water via heterogeneous Fenton mechanisms, Appl. Catal. A Gen. 316 (2007) 117–124. doi:10.1016/j.apcata.2006.09.027.
[151] I. Khan, S. Ali, M. Mansha, A. Qurashi, Sonochemical assisted hydrothermal synthesis of pseudo-flower shaped Bismuth vanadate ($BiVO_4$) and their solar-driven water splitting application, Ultrason. Sonochem. 36 (2017) 386–392. doi:10.1016/j.ultsonch.2016.12.014.
[152] J.H. Bang, K.S. Suslick, Applications of ultrasound to the synthesis of nanostructured materials, Adv. Mater. 22 (2010) 1039–1059. doi:10.1002/adma.200904093.
[153] K. Okitsu, M. Ashokkumar, F. Grieser, Sonochemical synthesis of gold nanoparticles: effects of ultrasound frequency., J. Phys. Chem. B. 109 (2005) 20673–5. doi:10.1021/jp0549374.
[154] J. Liu, T. Zhang, Z. Wang, G. Dawson, W. Chen, Simple pyrolysis of urea into graphitic carbon nitride with recyclable adsorption and photocatalytic activity, J. Mater. Chem. 21 (2011) 14398. doi:10.1039/c1jm12620b.
[155] I. Krivtsov, E.I. Garcia-Lopez, G. Marci, L. Palmisano, Z. Amghouz, J.R. Garcia, S. Ordonez, E. Diaz, Selective photocatalytic oxidation of 5-hydroxymethyl-2-furfural to 2,5-furandicarboxyaldehyde in aqueous suspension of g-C_3N_4, Appl. Catal. B Environ. 204 (2017) 430–439. doi:10.1016/j.apcatb.2016.11.049.
[156] B. Zhu, P. Xia, W. Ho, J. Yu, Isoelectric point and adsorption activity of porous g-C_3N_4, Appl. Surf. Sci. 344 (2015) 188–195. doi:10.1016/j.apsusc.2015.03.086.

[157] R. Jin, W. Gao, J. Chen, H. Zeng, F. Zhang, Z. Liu, N. Guan, Photocatalytic reduction of nitrate ion drinking water by using metal-loaded $MgTiO_3$-TiO_2 composite semiconductor catalyst, J. Photochem. Photobiol. A Chem. 162 (2004) 585–590. doi:10.1016/S1010-6030(03)00420-9.
[158] P. Liu, C. Li, Z. Zhao, G. Lu, H. Cui, W. Zhang, Induced effects of advanced oxidation processes., Sci. Rep. 4 (2014) 1–4. doi:10.1038/srep04018.
[159] S.J. Armaković, S. Armaković, N.L. Finčur, F. Šibul, D. Vione, J.P. Šetrajčić, B.F. Abramović, Influence of electron acceptors on the kinetics of metoprolol photocatalytic degradation in TiO_2 suspension. A combined experimental and theoretical study, RSC Adv. 5 (2015) 54589–54604. doi:10.1039/c5ra10523d.
[160] B. Zhu, P. Xia, Y. Li, W. Ho, J. Yu, Fabrication and photocatalytic activity enhanced mechanism of direct Z-scheme g-C_3N_4/Ag_2WO_4 photocatalyst, Appl. Surf. Sci. 391 (2017) 175–183. doi:10.1016/j.apsusc.2016.07.104.
[161] A.B. Murphy, Band-gap determination from diffuse reflectance measurements of semiconductor films, and application to photoelectrochemical water-splitting, Sol. Energy Mater. Sol. Cells. 91 (2007) 1326–1337. doi:10.1016/j.solmat.2007.05.005.
[162] S. Yang, Y. Gong, J. Zhang, L. Zhan, L. Ma, Z. Fang, R. Vajtai, X. Wang, P.M. Ajayan, Exfoliated graphitic carbon nitride nanosheets as efficient catalysts for hydrogen evolution under visible light, Adv. Mater. 25 (2013) 2452–2456. doi:10.1002/adma.201204453.
[163] Y. Shiraishi, S. Kanazawa, Y. Kofuji, H. Sakamoto, S. Ichikawa, S. Tanaka, T. Hirai, Sunlight-Driven Hydrogen Peroxide Production from Water and Molecular Oxygen by Metal-Free Photocatalysts, Angew. Chemie - Int. Ed. (2014) 1–7. doi:10.1002/anie.201407938.
[164] Y. Cui, Z. Ding, P. Liu, M. Antonietti, Metal-free activation of H_2O_2 by g-C_3N_4 under visible light irradiation for the degradation of organic pollutants, Phys. Chem. Chem. Phys. (2012) 1455–1462. doi:10.1039/c1cp22820j.
[165] W. Ong, L. Tan, S. Chai, S. Yong, A. Rahman, Surface charge modification via protonation of graphitic carbon nitride (g-C3N4) for electrostatic self-assembly construction of 2D/2D reduced graphene oxide (rGO)/g-C3N4 nanostructures toward enhanced photocatalytic reduction of carbon diode to methan, Nano Energy. 13 (2015) 757–770.
[166] G.T.S.T. Da Silva, A.E. Nogueira, J.A. Oliveira, J.A. Torres, O.F. Lopes, C. Ribeiro, Acidic surface niobium pentoxide is catalytic active for CO2 photoreduction, Appl. Catal. B Environ. 242 (2019) 349–357. doi:10.1016/j.apcatb.2018.10.017.
[167] A. Nikokavoura, C. Trapalis, Graphene and g-C3N4 based photocatalysts for NOx removal: A review, Appl. Surf. Sci. 430 (2018) 18–52. doi:10.1016/j.apsusc.2017.08.192.
[168] S. Ye, R. Wang, M.-Z. Wu, Y.-P. Yuan, A review on g-C_3N_4 for photocatalytic water splitting and CO_2 reduction, Appl. Surf. Sci. (2015). doi:10.1016/j.apsusc.2015.08.173.
[169] J. Jin, J. Luo, L. Zan, T. Peng, One-Pot Synthesis of Cu-Nanocluster-Decorated Brookite TiO2 Quasi-Nanocubes for Enhanced Activity and Selectivity of CO2 Photoreduction to CH4, ChemPhysChem. 18 (2017) 3230–3239. doi:10.1002/cphc.201700563.
[170] Y. Zhang, Q. Pan, G. Chai, M. Liang, G. Dong, Q. Zhang, J. Qiu, Synthesis and luminescence mechanism of multicolor-emitting g-C_3N_4 nanopowders by low temperature thermal condensation of melamine., Sci. Rep. 3 (2013) 1943. doi:10.1038/srep01943.
[171] H. Shi, G. Chen, C. Zhang, Z. Zou, Polymeric g-C_3N_4 Coupled with $NaNbO_3$ Nanowires toward Enhanced Photocatalytic Reduction of CO_2 into Renewable Fuel, ACS Catal. 4 (2014) 3637–3643.